Astronomy Reports, Vol. 45, No. 12, 2001, pp. 1002–1011. Translated from Astronomicheskiĭ Zhurnal, Vol. 78, No. 12, 2001, pp. 1135–1145.

Intermediate-Brightness Spectrophotometric Standards. Standards Near +40° Declination

V. M. Tereshchenko

Fesenkov Astrophysical Institute, Academy of Sciences of Kazakhstan, Kamenskoe Plato, Almaty, 480068 Kazakhstan

Received June 22, 2000

Abstract—The second stage in our program to compile a list of regional intermediate-brightness spectrophotometric standards has been completed. We have obtained spectral energy distributions for 24 stars with magnitudes $7^m.0$–$8^m.5$ near +40° declination. The range $\lambda\lambda$3100–7600 Å was studied with a spectral resolution of 50 Å. The relative rms error of our results in the visible is 1–2%, increasing to 3–5% toward the edges of the studied wavelength interval. All the stars are referenced to a single standard, the circumpolar star HD 221525. The energy distributions were used to compute color indices in the UBV, $WBVR$, and $UPXYZVS$ systems, as well as in the system of the TYCHO catalog. The computed and observed values for stars in common with the TYCHO catalog are compared. © *2001 MAIK "Nauka/Interperiodica"*.

1. INTRODUCTION

A star's spectral energy distribution $E(\lambda)$ is one of its principal observed, as well as physical, parameters. In addition, stars with well-studied energy distributions can be used as spectrophotometric standards for observations of other celestial bodies. By 2000, the spectral energy distributions in the visible had been studied for more than two thousand stars, the vast majority brighter than 6^m. More than half of the studied stars can be used as spectrophotometric standards and spectral calibrations of light receivers. The remaining stars are variable, cannot be used due to the character of their spectra, or have inaccurately known $E(\lambda)$ distributions. Understandably, fainter standards are needed for standardization when using large telescopes. However, there are fewer than 200 stars fainter than 6^m with known $E(\lambda)$ distributions [1–10], which is obviously insufficient. The low density of faint standards results in losses of precious observing time on large telescopes. In addition, it is known that calibration accuracy depends on the difference of the zenith distances of the object and standard and on the time interval between their observations. It is not always possible to minimize both parameters if too few standards are available. Thus, it remains important to study $E(\lambda)$ for stars fainter than 6^m. It is interesting that, prior to the publication of [8–10], the total number of fainter standards (13^m–17^m) exceeded that of intermediate-brightness standards (7^m–10^m); thanks to the efforts of Chilean astronomers [7], there were more intermediate-brightness standards in the southern than in the northern hemisphere. Note also that most papers on spectrophotometry of faint stars present data on fluxes or illuminations in the visible only for some wavelengths. Usually, the number of measured positions in the spectrum does not exceed 20.

In [11], we proposed several stellar spectrophotometric observing programs that we felt to have high priority. Among these were programs to identify circumpolar, intermediate-declination (northern hemisphere) and equatorial, intermediate-brightness standards. Though these proposals were put forward more than seven years ago, they retain their importance. In fact, the American spectrophotometric study [8] of comparatively bright open-cluster members was included among our listed programs, confirming the well groundedness of our proposals. In [11], we presented spectral energy distributions for 14 circumpolar ($\delta > 85°$) stars. The current paper is devoted to the second stage of our suggested program. We present the energy distributions for 24 stars we recommend as secondary spectrophotometric standards for the northern hemisphere. We have selected these stars taking into account the general requirements for standards (that they be single, non-variable stars), as well as the following considerations and possibilities.

(1) The standards should be positioned more or less uniformly in right ascension along the fortieth parallel, in the declination strip $\delta = 40° \pm 2°$. The total number of stars selected was 24, corresponding to, on average, one star per hour of right ascension.

(2) The standards should be fainter than 7^m. The limiting magnitude depends not only on the instrumentation, but also on the required accuracy and

1063-7729/01/4512-1002$21.00

Table 1. Program stars and their principal characteristics

No.	HD	α_{2000}	δ_{2000}	V	$B-V$	Sp
01	4806	$0^h50^m27^s$	40° 48′.5	$8^m.0$	$0^m.0$	B8.5V
02	5065	0 52 52	40 14.7	7.0	0.6	G0V
03	15980	2 35 14	40 35.3	7.8	0.0	B9.5V
04	16175	2 37 02	42 03.7	7.2	0.7	G0V
05	27831	4 25 20	39 03.1	7.8	0.7	G0V
06	27970	4 26 42	41 07.4	7.9	0.0	B9.5V
07	44614	6 24 31	38 34.1	7.7	0.6	G0V
08	45041	6 27 10	40 12.8	8.2*	–	B9V
09	72543	8 35 03	41 01.4	7.6	0.8	G5IV
10	72862	8 36 40	39 25.1	7.9*	–	A2
11	94479	10 54 58	39 47.4	8.2	–	A2m
12	94792	10 57 06	41 21.1	7.4	0.6	G0V
13	108076	12 24 46	38 19.1	8.02	0.56	G0V
14	109995	12 38 47	39 18.5	7.62	0.05	A0V
15	124320	14 11 57	38 49.9	8.86	–	A2V
16	124968	14 15 35	39 40.6	7.6	0.9	G5IV
17	149025	16 30 23	40 44.2	7.9	0.6	G0V
18	150391	16 39 09	38 20.7	7.6	0.1	A2V
19	173074	18 41 27	40 28.6	8.0	0.9	G5IV
20	173052	18 41 33	41 23.4	8.0	0.1	A0
21	195629	20 31 02	40 25.6	7.60	−0.08	B9.5V
22	195988	20 33 01	41 28.4	7.1	0.6	G0V
23	214524	22 38 09	41 07.2	7.49	−0.04	B8.5V
24	218355	23 06 55	38 01.0	7.9	0.9	G5IV

Asterisks indicate photographic magnitudes from [14].

spectral resolution. With all this in mind, we restricted our consideration to stars brighter than $8^m.5$.

(3) We decided that the secondary standards should belong to luminosity classes IV or V and spectral types either B8–A2 or G0–G5, and that the spectral types should alternate in right ascension, forming pairs of an early and a late star. Early-type stars are usually preferred as spectrophotometric standards: their spectra include extended smooth sections convenient for use in instrumental calibration and the reduction of data for other objects. We recommend G stars for two reasons. First, they are best suited for observations of galaxies, most of which have integrated spectra resembling those of G stars [12]. Second, low-resolution spectra of G stars are fairly smooth and show only modest flux-intensity changes in the typical working ranges of CCD detectors ($\lambda\lambda$ 4200–9000 Å). There is another, indirect reason to include G stars in our list of standards: spectrophotometric data are needed in connection with another problem — the search for photometric analogs of the Sun. Note that the small number of different spectral types among the standards will make it possible for observers to quickly become accustomed to the appearance of their spectra for the particular instruments they are using. Comparisons of the expected and observed spectra of standard stars enable judgment about the conditions of the instrumentation used and the atmosphere during observations.

Table 1 contains the list of our program stars, which we recommend as secondary standards, along

Table 2. Spectral energy distributions of the intermediate-declination standards (in units of 10^{-6} erg cm^{-2} s^{-1} cm^{-1})

λ, Å	Standard No.											
	01	02	03	04	05	06	07	08	09	10	11	12
3125	300	305	288	147	65	182	144	290	52	123	120	170
3175	301	319	284	169	65	179	144	288	51	128	120	175
3225	293	331	284	166	70	173	145	273	51	123	121	185
3275	284	414	280	217	84	169	179	263	72	133	124	212
3325	275	410	276	220	83	171	190	264	71	129	124	217
3375	274	408	273	208	78	169	166	253	69	128	123	202
3425	265	420	271	216	80	167	170	242	73	126	126	210
3475	255	404	265	202	78	166	169	240	76	121	124	209
3525	252	431	261	229	81	162	184	234	83	123	126	216
3575	244	428	264	216	77	159	171	232	72	123	127	215
3625	242	453	258	245	93	163	188	226	103	125	129	225
3675	237	511	261	280	114	160	221	217	125	129	130	253
3725	254	478	275	258	100	179	206	232	103	139	138	243
3775	283	485	342	243	95	221	196	250	94	153	150	245
3825	356	463	436	224	82	291	172	297	68	198	177	242
3875	419	549	495	249	96	347	195	335	89	255	211	283
3925	455	455	550	240	97	374	191	354	95	272	213	241
3975	378	530	452	284	120	312	226	290	128	226	195	271
4025	517	779	608	429	169	435	324	369	214	346	282	388
4075	437	733	514	412	163	378	306	330	216	274	246	379
4125	424	783	495	432	169	335	323	314	222	267	240	384
4175	476	790	524	421	161	386	318	330	204	311	271	395
4225	452	760	525	437	166	388	324	323	230	311	263	389
4275	446	743	517	427	162	385	313	318	229	299	266	377
4325	344	727	409	409	164	303	302	261	249	215	212	356
4375	395	794	474	450	179	330	334	294	278	266	231	391
4425	398	804	470	464	181	343	340	286	286	277	245	397
4475	379	820	456	486	198	335	360	279	317	272	244	409
4525	370	832	439	498	193	329	363	271	333	259	239	413
4575	359	834	422	492	197	317	364	266	339	257	233	408
4625	350	833	422	497	196	312	363	259	352	256	232	413
4675	339	831	408	477	186	300	354	252	344	239	227	405
4725	324	816	393	477	189	288	354	240	356	235	225	404
4775	309	811	377	494	193	283	357	228	362	224	216	397
4825	279	788	338	475	187	256	341	206	358	191	196	385
4875	238	748	291	446	178	215	327	193	351	165	169	358
4925	286	780	344	461	189	261	344	213	364	200	196	382
4975	281	784	338	479	188	259	345	210	371	205	203	388
5025	272	762	322	450	182	255	335	203	354	195	197	372
5075	269	788	313	466	185	248	345	198	368	190	196	382
5125	258	773	301	463	181	242	335	194	362	186	190	375
5175	250	736	294	431	173	234	318	189	345	178	183	354
5225	245	752	286	446	178	231	328	184	369	179	182	364
5275	239	743	277	441	182	227	331	181	367	177	176	359
5325	233	756	270	451	180	223	333	178	384	171	177	365

Table 2. (Contd.)

λ, Å	Standard No.											
	01	02	03	04	05	06	07	08	09	10	11	12
5375	228	750	264	447	181	217	331	174	391	168	171	357
5425	225	755	258	455	187	214	332	171	393	162	169	362
5475	221	762	251	454	181	209	333	169	394	159	167	362
5525	214	759	247	454	180	208	334	163	397	155	167	360
5575	212	747	238	441	185	206	333	160	396	154	164	354
5625	207	735	239	448	174	202	329	157	403	150	163	345
5675	203	729	236	441	182	200	324	155	394	149	159	348
5725	200	731	234	443	180	197	321	148	413	145	157	347
5775	197	715	225	444	177	190	328	147	413	140	156	344
5825	191	736	225	446	189	184	327	142	410	141	156	344
5875	185	721	221	445	182	183	318	141	404	137	151	342
5925	182	715	208	440	180	178	315	137	408	134	151	340
5975	180	710	201	440	177	174	310	135	403	132	150	337
6025	178	710	199	430	180	170	305	133	396	130	148	334
6075	172	705	194	428	183	165	300	130	388	129	146	334
6125	168	700	190	421	176	161	297	122	379	126	145	326
6175	163	689	185	407	176	157	291	121	383	122	142	321
6225	159	681	180	405	166	152	288	117	380	119	140	320
6275	154	666	177	393	171	149	289	113	373	115	139	313
6325	149	664	171	389	162	145	284	110	381	112	135	314
6375	146	661	168	385	160	143	289	107	585	110	134	310
6425	140	650	163	383	152	140	289	105	376	105	131	307
6475	137	655	160	381	162	138	286	102	383	105	129	304
6525	132	659	156	389	163	131	280	100	382	102	124	300
6575	115	596	133	363	150	113	250	85	373	83	114	276
6625	127	620	150	373	147	130	274	93	376	96	124	280
6675	124	633	147	369	157	133	276	94	370	100	124	290
6725	124	618	147	376	153	130	267	92	379	96	122	279
6775	120	604	145	370	153	128	265	92	375	93	121	273
6825	113	586	141	361	159	126	265	89	365	90	118	276
6875	118	584	140	360	154	125	260	89	360	93	116	276
6925	112	578	133	348	144	124	254	83	367	91	119	268
6975	114	579	133	353	150	122	255	85	363	87	115	265
7025	109	560	130	338	145	120	256	82	354	87	114	262
7075	99	558	124	338	145	117	241	79	345	84	113	257
7125	99	559	124	342	140	114	252	80	353	83	115	255
7175	100	554	118	328	138	113	244	78	340	83	114	252
7225	98	548	115	331	135	114	233	76	339	82	113	246
7275	97	544	111	340	140	110	238	75	342	80	112	262
7325	94	540	109	338	140	107	233	73	342	76	109	243
7375	97	530	103	324	135	105	226	71	349	77	107	239
7425	93	514	107	305	136	103	228	70	339	72	106	232
7475	92	519	104	296	130	101	229	68	329	71	106	233
7525	91	516	97	307	134	102	220	70	327	66	105	229
7575	83	516	89	284	124	96	218	65	325	66	104	221

Table 2. (Contd.)

λ, Å	Standard No.											
	13	14	15	16	17	18	19	20	21	22	23	24
3125	150	232	90	58	130	317	80	121	670	220	999	88
3175	151	230	88	67	127	316	81	124	649	218	971	91
3225	146	228	85	62	134	315	82	121	627	219	945	89
3275	162	225	86	90	152	310	99	122	612	278	928	108
3325	160	223	85	86	154	313	103	120	589	280	897	102
3375	152	222	80	72	149	307	99	122	567	271	865	103
3425	156	226	79	84	153	310	104	126	550	281	856	106
3475	160	222	78	84	147	302	96	124	534	279	828	100
3525	162	219	77	93	151	304	107	127	521	306	798	112
3575	154	222	76	79	148	304	99	126	510	284	781	107
3625	160	215	77	107	160	308	105	127	501	301	761	113
3675	179	220	81	133	183	310	122	130	491	332	745	131
3725	170	276	89	112	180	326	114	139	505	323	711	120
3775	167	360	101	107	174	365	115	162	537	313	692	117
3825	159	475	128	88	171	459	109	206	652	309	771	111
3875	186	564	148	95	194	546	128	250	762	368	850	128
3925	144	631	166	105	173	614	107	280	783	303	875	118
3975	168	523	145	136	199	532	121	233	662	332	765	131
4025	233	727	211	220	287	810	176	342	852	490	896	194
4075	228	587	174	219	268	638	166	279	749	476	832	184
4125	229	585	165	220	284	639	176	270	694	483	780	194
4175	225	649	189	206	283	731	169	307	749	487	802	189
4225	229	653	194	225	290	743	172	306	746	487	799	187
4275	219	640	190	230	276	721	167	306	739	466	801	181
4325	214	470	144	246	257	515	157	222	597	464	678	182
4375	227	554	166	264	296	624	177	262	643	490	699	196
4425	232	564	172	276	295	651	182	272	637	502	685	205
4475	242	551	168	299	301	645	186	267	615	514	660	209
4525	241	538	167	310	308	630	189	256	593	526	652	209
4575	241	519	164	315	307	616	187	252	572	519	626	205
4625	240	505	158	332	309	609	187	246	563	534	612	208
4675	238	488	154	324	300	600	184	240	539	524	597	206
4725	238	471	149	327	294	563	180	228	518	525	569	204
4775	234	448	142	336	296	537	178	217	492	520	545	205
4825	227	402	126	335	279	470	172	190	445	494	504	199
4875	218	339	107	328	265	391	165	167	403	477	461	190
4925	225	405	127	331	278	492	171	198	449	492	497	195
4975	226	414	128	339	281	498	179	202	448	505	495	199
5025	225	401	127	334	272	481	167	195	424	472	476	190
5075	224	388	126	338	283	476	176	193	421	503	470	197
5125	219	385	123	334	278	464	167	186	407	489	452	195
5175	209	373	119	312	256	446	158	179	392	456	444	184
5225	219	360	117	335	267	440	166	175	385	477	434	191
5275	221	352	115	338	259	423	165	170	370	468	417	188
5325	220	339	112	352	268	418	166	165	358	486	405	193

Table 2. (Contd.)

λ, Å	Standard No.											
	13	14	15	16	17	18	19	20	21	22	23	24
5375	216	331	111	361	270	410	167	161	349	478	398	194
5425	219	327	108	356	267	402	164	158	342	470	387	192
5475	215	320	106	366	268	396	166	155	334	475	380	193
5525	218	309	105	364	269	389	165	152	326	478	371	195
5575	215	306	103	365	266	380	165	147	314	467	358	188
5625	215	299	101	364	259	375	159	143	308	466	350	189
5675	218	294	98	66	255	365	159	139	299	458	341	189
5725	210	285	98	65	259	360	154	137	289	458	333	185
5775	213	276	95	62	251	349	159	133	279	452	324	183
5825	213	271	93	380	259	343	156	131	274	452	321	185
5875	210	263	91	377	258	336	155	128	265	452	310	185
5925	208	255	88	372	255	327	155	126	260	450	305	179
5975	205	252	85	370	255	322	152	124	257	444	299	176
6025	203	247	83	371	250	316	150	122	253	439	293	176
6075	201	242	80	364	246	312	150	121	246	433	287	171
6125	200	238	78	359	39	305	147	119	240	425	281	171
6175	192	232	75	349	232	296	141	115	233	416	273	170
6225	190	227	74	352	234	289	146	112	229	413	267	165
6275	191	226	73	350	231	284	142	110	224	405	260	162
6325	182	216	71	348	225	276	141	107	218	402	252	163
6375	186	209	70	351	225	271	144	105	214	406	249	164
6425	184	207	68	350	221	264	146	102	207	400	241	160
6475	185	205	67	346	221	259	139	100	202	392	235	158
6525	180	194	62	347	220	241	142	97	190	369	228	159
6575	175	160	57	349	201	205	129	79	168	370	205	152
6625	182	186	66	347	215	237	135	92	186	378	214	153
6675	179	185	65	347	213	240	135	91	182	380	211	154
6725	178	183	64	341	210	238	130	89	180	380	210	155
6775	177	182	63	348	209	234	132	88	177	375	202	151
6825	175	174	58	340	206	225	129	87	170	375	193	151
6875	171	176	58	337	203	222	130	85	165	370	189	150
6925	170	170	57	335	199	219	126	85	162	365	191	146
6975	173	170	56	333	203	214	126	83	160	360	187	147
7025	171	161	54	331	196	213	125	82	156	355	184	152
7075	168	159	53	327	191	204	125	79	153	350	178	147
7125	166	157	52	330	196	203	120	78	148	348	174	151
7175	165	155	51	323	192	198	121	78	146	340	172	150
7225	164	149	50	323	187	198	124	78	145	345	174	148
7275	163	143	51	323	188	195	123	76	142	338	171	145
7325	158	146	52	319	185	194	120	73	141	334	169	143
7375	156	140	50	321	182	190	116	74	138	328	160	136
7425	153	138	51	313	180	186	115	72	130	322	167	136
7475	149	137	50	315	178	182	110	70	125	323	159	140
7525	146	130	49	313	177	178	110	69	123	317	150	133
7575	147	132	49	311	176	177	105	68	120	315	150	133

with their principal characteristics. The data were taken from the SC catalog [13], with the exception of the two values marked with asterisks, which were taken from the PPM catalog [14]. The latter presents photographic magnitudes rather than V magnitudes. As a rule, the V and $B-V$ values given in [13] are based on the reduction of photographic data, and, accordingly, are somewhat crude and nonuniform. Photoelectric data are available for only five stars. Due to the lack of availability of trustworthy photometric and spectroscopic data at the time of the program-star selection (1993), we later found that some of the stars do not completely satisfy the above criteria.

2. OBSERVATIONS AND REDUCTION

Our observations were carried out in 1993–1994 at the former Tien Shan high-altitude observatory of the Sternberg Astronomical Institute ($h = 2800$ m above sea level), near Almaty (this observatory has now become a national facility of Kazakhstan). We used the 1-m Karl Zeiss (Jena) telescope with a one-channel Seya–Namioka spectrometer with a curved diffraction grating. This spectrometer has been described in numerous of our previous papers (for example, cf. [15]). A detailed description of the observation and reduction techniques can be found in [11]. Here, we will summarize only the principal features and discuss differences from the earlier methods used.

As in [11], the primary standard was the circumpolar star HD 221525, whose spectral energy distribution was derived by us earlier [16]. The careful analysis in [17] shows this to be an excellent standard. The differences between the observed color indices for this star and those computed from the spectral energy distribution proved to be the lowest among all primary spectrophotometric standards. In contrast to the measurement technique applied for the catalog [15], our reduction now uses readings corresponding to the primary standard's integrated spectrum rather than the integrated envelope. Compared to the approach used for the catalog, this method provides more definite and unambiguous final results near the Balmer jump, but also leads to higher uncertainties at the wavelengths corresponding to the Balmer lines, Hα–Hε. Because we used only one standard and the equal-altitude method, is was necessary to prepare a strict schedule of observations for each night. When this schedule was carefully followed, the air-mass difference between the program stars and the standard was, on average, less than 0.1. In rare cases, due to various operational errors, the difference reached 0.20.

During the program observations, a global deterioration of the Earth's atmospheric transparency occurred due to the eruption of the volcano Pinatubo in the Philippines in the Summer of 1991. The worsening of the transparency was accompanied by an abrupt drop in the number of clear nights. Our measurements [18] show that the 1993–1994 transparency at northern Tien Shan was decreased by 10–12%. When performing the atmospheric reduction, we used the mean transparency coefficients for each observing season.

We observed each star on four to six different nights. On each night, we obtained four, and in rare cases, two scans. As a result, from 12 to 20 scans were acquired for each star. The observations had a resolution of 20–30 Å, but we decreased this to the standard 50 Å during the reduction of the data.

Our final results, the extra-atmospheric monochromatic illuminations $E(\lambda)$ for the program stars, are collected in Table 2. The wavelengths (in Å) in the first column refer to the centers of the averaged intervals; the upper row contains the ordinal numbers of the secondary standards from Table 1. After computer reduction of the data, we examined large-scale plots for each star, corrected obvious errors, and introduced corrections for suspicious data points. The number of such points was usually from 5 to 10–12. As a rule, they appeared at the edges of the studied spectral regions or near 600 nm. This latter wavelength is where the filter separating the first and the second spectral orders is introduced, and is also the location of a switch between sensitivity levels. We stress that we did not perform excessive smoothing, as can be seen from the scatter of the data, especially toward the edges of the wavelength range considered.

The relative rms error of the tabulated illuminations for 400–650 nm is, on average, 1 to 2%, increasing to 3–5% toward the edges of this interval. The errors are mainly instrumental.

3. COMPUTED COLOR INDICES

Prior to the HIPPARCOS and TYCHO catalogs [19], neither spectrophotometric data nor photoelectric photometry were available for the vast majority of our program stars. Though photometric data can be considered only a substitute for spectrophotometry, they are among the most important observable parameters of celestial bodies. Therefore, we used the obtained energy distributions to derive the program stars' color indices in two broad-band photometric systems, UBV and $WBVR$, as well as in the intermediate-band Vilnius system. This procedure involves convolution of the energy distribution with the response curves of the system of interest; this process has been applied by us and other authors many times and is described in detail, for example,

Table 3. UBV, $WBVR$, and $UPXYZVS$ color indices computed from the spectral energy distributions

Standard No.	UBV		$WBVR$			$UPXYZVS$					
	$U-B$	$B-V$	V	$W-B$	$B-V$	$U-P$	$P-X$	$X-Y$	$Y-Z$	$Z-V$	$V-S$
01	-0.20^m	-0.01^m	8.056^m	-0.224^m	$+0.006^m$	0.47^m	0.72^m	0.20^m	0.11^m	0.07^m	0.22^m
02	0.04	0.57	6.738	−0.046	0.594	0.51	0.66	0.69	0.33	0.20	0.61
03	−0.13	−0.03	7.896	−0.108	−0.015	0.60	0.75	0.22	0.08	0.05	0.24
04	0.15	0.62	7.294	0.057	0.645	0.50	0.73	0.78	0.31	0.21	0.61
05	0.18	0.65	8.275	0.091	0.676	0.52	0.75	0.78	0.35	0.22	0.64
06	0.00	0.10	8.108	0.055	0.158	0.66	0.84	0.27	0.16	0.09	0.27
07	0.08	0.60	7.631	−0.033	0.632	0.46	0.66	0.74	0.34	0.21	0.56
08	−0.40	0.01	8.363	−0.464	0.028	0.40	0.55	0.19	0.12	0.09	0.20
09	0.71	0.98	7.448	0.600	1.018	0.49	0.99	1.18	0.47	0.29	0.77
10	0.06	0.08	8.403	0.095	0.091	0.63	0.87	0.33	0.12	0.08	0.27
11	0.02	0.25	8.345	−0.013	0.266	0.57	0.77	0.42	0.21	0.11	0.46
12	0.02	0.52	7.539	−0.066	0.633	0.50	0.66	0.66	0.31	0.18	0.58
13	−0.17	0.54	8.086	−0.291	0.610	0.41	0.52	0.63	0.33	0.20	0.59
14	0.11	0.02	7.653	0.225	0.035	0.81	0.91	0.25	0.13	0.06	0.22
15	0.06	0.13	8.857	0.082	0.141	0.61	0.86	0.36	0.15	0.09	0.23
16	0.55	0.92	7.545	0.445	0.962	0.57	0.90	1.08	0.45	0.29	0.76
17	0.05	0.53	7.868	−0.036	0.628	0.50	0.68	0.68	0.30	0.20	0.57
18	0.06	0.12	7.424	0.074	0.130	0.58	0.87	0.37	0.14	0.08	0.25
19	−0.03	0.54	8.393	−0.122	0.565	0.46	0.62	0.67	0.31	0.20	0.60
20	0.04	0.05	8.437	0.086	0.062	0.66	0.86	0.30	0.13	0.05	0.25
21	−0.40	−0.10	7.605	−0.466	−0.083	0.38	0.58	0.14	0.08	0.04	0.17
22	0.02	0.56	7.244	−0.111	0.586	0.49	0.62	0.69	0.33	0.20	0.56
23	−0.66	−0.07	7.466	−0.794	−0.046	0.23	0.38	0.14	0.11	0.05	0.21
24	0.04	0.58	8.231	−0.061	0.611	0.48	0.67	0.70	0.34	0.21	0.58

by Straizys [20]. The response curves for the photometric systems were taken from [21–23]. The constants were determined from the main primary standard Vega, assuming equal observed and computed magnitudes and color indices for this star. The results of our computations are presented in Table 3. These will provide an indirect check of our results only when observations of these stars in the systems in question are acquired. However, Table 3 already enables us to draw several conclusions. We can compare the computed color indices for an individual star with the so-called normal (mean for the corresponding spectral type) color indices and identify discrepant cases. For example, the computed $W-B$ indices are in conflict with the spectral types attributed to HD 45041 (B9V), HD 108076 (G0V), and HD 173024 (G5IV). In addition, there is an obvious scatter of $W-B$ for the G5IV stars: HD 72543 ($0^m.600$), HD 124968 ($0^m.445$), HD 173024 ($-0^m.122$), and HD 218355 ($0^m.061$). In our opinion, these discrepancies are mainly associated with errors in spectral classification.

For the $WBVR$ system, in addition to the color indices, Table 3 presents the V magnitudes, which coincide with those computed for the UBV system to within hundredths of a magnitude. We can see from

Table 4. Observed and calculated values of V_T and $B_T - V_T$ and their residuals

Standard No.	HD	V_T^O	V_T^C	δV_T	$(B_T^O - V_T^O)$	$(B_T^C - V_T^C)$	$\delta(B_T - V_T)$
1	4806	$8^m.118$	$8^m.048$	$+0^m.070$	$-0^m.034$	$+0^m.011$	$-0^m.045$
2	5065	6.832	6.798	0.034	+0.641	+0.638	+0.003
3	15980	7.879	7.873	0.006	−0.038	+0.010	−0.048
4	16175	7.340	7.356	−0.016	+0.710	+0.710	0.000
5	27831	8.306	8.344	−0.038	+0.740	+0.737	+0.003
6	27790	8.051	8.114	−0.063	+0.114	+0.131	−0.017
7	44614	7.665	7.693	−0.028	+0.698	+0.688	+0.010
8	45041	−	8.356	−	−	+0.020	−
9	72543	7.527	7.549	−0.022	+1.180	+1.154	+0.026
10	72862	8.393	8.433	−0.040	+0.133	+0.091	+0.047
11	94479	−	8.367	−	−	+0.092	−
12	94792	−	7.592	−	−	+0.594	−
13	108076	8.085	8.146	−0.061	+0.635	+0.597	+0.038
14	109995	7.603	7.644	−0.041	+0.052	+0.059	−0.007
15	124320	8.853	8.865	−0.012	+0.165	+0.167	−0.002
16	124968	7.599	7.643	−0.044	+1.118	+1.075	+0.043
17	149025	7.934	7.924	+0.010	+0.629	+0.600	+0.029
18	150391	7.434	7.428	+0.006	+0.165	+0.165	0.000
19	173024	−	8.448	−	−	+0.607	−
20	173052	8.435	8.428	+0.007	+0.090	+0.095	−0.005
21	195629	7.618	7.575	+0.043	−0.080	−0.077	−0.003
22	195988	−	7.300	−	−	+0.632	−
23	214524	7.467	7.443	+0.024	−0.068	−0.061	−0.007
24	218355	8.331	8.292	+0.039	0.675	+0.658	+0.017
Mean				−0.007			+0.004

this table that the computed V magnitudes deviate significantly from those given in Table 1. The differences can reach $0^m.3$–$0^m.5$! These are clearly due to errors in the magnitudes presented in [13], which, as was noted above, were mainly derived from the reduction of photographic data. This is confirmed by a comparison of the spectrophotometric data with photometric data from the HIPPARCOS mission. Table 4 contains the V_T magnitudes and $B_T - V_T$ color indices measured by the HIPPARCOS satel-

lite (the TYCHO catalog) and computed from our spectrophotometric data, along with their residual differences. The response curves for the photometric system of the TYCHO catalog were taken from [19]. Since there are no photometric data for Vega in the TYCHO catalog, we derived the constants determining the zero point of the magnitude scale using our primary standard, HD 221525. The δV_T and $\delta(B_T - V_T)$ residuals characterize the external agreement of our spectrophotometric data and the space-borne photometry of the HIPPARCOS mission. To some extent, they reflect the reliability of our spectrophotometric data. It follows from the table that, on average, the mean δV_T residual for the set of 19 stars is $0\overset{m}{.}007$, whereas the average $\delta(B_T - V_T)$ is $0\overset{m}{.}004$. For six stars, however, the residuals δV_T exceed $0\overset{m}{.}04$, and the residuals $\delta(B_T - V_T)$ exceed $0\overset{m}{.}03$. These are definitely higher than the combined standard errors quoted by the authors of the TYCHO catalog ($0\overset{m}{.}008$) and by us (1–2%).

Unfortunately, our attempts to discover the origins of these discrepancies were unsuccessful. Despite the well-deserved reputation of the TYCHO catalog, we are not convinced that these large discrepancies are entirely associated with our data. A more complete analysis of the secondary standards will be carried out after completion of the third stage of our program. In addition to the TYCHO catalog, we intend to use *uvby* data for this purpose.

4. CONCLUSIONS

We have completed the second stage of our program aimed at compiling a uniform system of regional intermediate-brightness spectrophotometric standards. We have obtained absolute spectral energy distributions for 24 stars with magnitudes 7^m–9^m at declinations near +40°. The relative rms error of our data in the visible is 1–2%. We used the spectral energy distributions to compute the color indices in three photometric systems: UBV, $WBVR$, and $UPXYZVS$. We have identified cases of significant discrepancies between assigned spectral type and computed color indices. We have compared our spectrophotometric data with photometric data acquired during the HIPPARCOS mission. Further analysis of the data will continue in our future work.

ACKNOWLEDGMENTS

I wish to express my sincere thanks to A. Mironov for his aid during the observations and for valuable advice, as well as to T. Bobryashova, O. Kolykhalova, L. Knyazeva, and N. Morozova for their assistance with the observations and computations. I am also grateful to the referee for constructive criticism.

REFERENCES

1. R. P. S. Stone, Astrophys. J. **218**, 767 (1977).
2. R. P. S. Stone, Mon. Not. R. Astron. Soc. **204**, 347 (1983).
3. P. Massey, K. Strobel, J. V. Barnes, and E. E. Anderson, Astrophys. J. **328**, 315 (1988).
4. J. B. Oke and J. E. Gunn, Astrophys. J. **266**, 713 (1983).
5. J. B. Oke, Astron. J. **99**, 1621 (1990).
6. A. Guttierez-Moreno, H. Moreno, G. Cortes, and E. Wenderoth, Publ. Astron. Soc. Pac. **100**, 973 (1988).
7. Mario Hamuy, A. R. Walker, N. B. Suntzeff, *et al.*, Publ. Astron. Soc. Pac. **104**, 533 (1992).
8. L. Clampitt and D. Burstein, Astron. J. **114** (2), 699 (1997).
9. V. V. Biryukov, G. V. Borisov, I. N. Glushneva, and V. I. Shenavrin, Astron. Astrophys. Trans. **16**, 83 (1998).
10. G. V. Borisov, I. N. Glushneva, and V. I. Shenavrin, Astron. Astrophys. Trans. **17**, 309 (1999).
11. V. M. Tereshchenko, Astron. Zh. **71**, 468 (1994) [Astron. Rep. **38**, 410 (1994)].
12. B. A. Vorontsov-Vel'yaminov, *Extragalactic Astronomy* [in Russian] (Nauka, Moscow, 1978).
13. A. Hirshfeld and R. W. Sinnot, *Sky Catalogue 2000.0* (Cambridge Univ. Press, Cambridge, 1982), Vol. 1.
14. S. Roeser and U. Bastian, *Positions and Proper Motions of 18 1731 Stars* (Spectrum. Acad. Verlag, Heidelberg, 1991), Vol. 1.
15. A. V. Kharitonov, V. M. Tereshchenko, and L. N. Knyazeva, *Spectrophotometric Star Catalogue* [in Russian] (Nauka, Alma-Ata, 1988).
16. V. M. Tereshchenko and E. A. Glushkova, Astron. Zh. **69**, 436 (1992) [Sov. Astron. **36**, 218 (1992)].
17. A. V. Mironov and V. G. Moshkalev, Astron. Zh. **72**, 80 (1995) [Astron. Rep. **39**, 70 (1995)].
18. V. M. Tereshchenko, Astron. Tsirk., No. 1556, 41 (1994).
19. M. A. C. Perryman, E. Hog, J. Kovalevsky, *et al.*, *The Hipparcos and Tycho Catalogues,* ESA SP-1200 (1997).
20. V. Straizys, *Multicolor Stellar Photometry* (Mokslas, Vil'nyus, 1977; Pachart Publ. House, Tucson, 1992).
21. A. Azhusenis and V. Straizhis, Astron. Zh. **46**, 402 (1969) [Sov. Astron. **13**, 316 (1969)].
22. V. G. Kornilov, I. M. Volkov, A. I. Zakharov, *et al., Catalogue of WBVR Values for Bright Stars of the Northern Sky* [in Russian] (Mosk. Gos. Univ., Moscow, 1991).
23. V. Straizys and K. Zdanavicius, Byull. Vil'nyus. Obs., No. 29, 15 (1970).

Translated by N. Samus'

Astronomy Reports, Vol. 45, No. 12, 2001, pp. 1012–1017. Translated from Astronomicheskiĭ Zhurnal, Vol. 78, No. 12, 2001, pp. 1146–1152.

Quasi-Biennial Oscillations of the Global Solar Magnetic Field

V. N. Obridko and B. D. Shelting

Institute of Terrestrial Magnetism, Ionosphere, and Radiowave Propagation, Troitsk, 142190, Russia

Received March 16, 2001

Abstract—Quasi-biennial oscillations (QBOs) can clearly be distinguished in uniform series of data on the solar magnetic-field polarity derived from Hα observations in 1915–1999. These have been proven to represent oscillations of the global magnetic field of the Sun. This is verified by spectral analyses executed using various methods: the QBOs are clearly visible in low harmonics ($l = 1$–3), but abruptly disappear for $l = 4$ and higher. First and foremost, the QBOs are displayed in variations of the sector structure of the large-scale magnetic field, demonstrating that they correspond to variations of the horizontal multipoles.

1. INTRODUCTION

The current paper continues our study of the Sun's large-scale magnetic fields and their behavior over an extended time interval (1915–1999). The characteristics of the large-scale magnetic field have been derived from Hα observations using an original method [1–5]. We will consider in detail one specific property of the large-scale field, namely quasi-periodic two to three-year oscillations. These oscillations have been named the "quasi-biennial oscillations" (QBOs), and we adopt this term here.

QBOs have been detected in the solar atmosphere in numerous studies based on analyses of various solar signals and indices, and many papers have been devoted to this phenomenon. This oscillation mode has been detected in solar-activity variations in the polar zone [6, 7], features of the large-scale magnetic fields [8], dynamics of sunspot indices [9], and geomagnetic activity [10, 11]. We note also the detection of QBOs in the magnetic field of the Sun as a star [12], the solar neutrino flux [13–15], displacements of magnetic neutral lines [16], in the Earth's stratosphere [17] (though it is not clear if these are related to the solar QBOs), in the total flux of the solar radiation [18], and in the solar wind and heliospheric magnetic fields [19].

In general, the QBOs do not exhibit any stable harmonic oscillations. Their period has been found to vary strongly from 1.5 to 3 yrs in a number of observations. It is possible that the QBOs correspond to a sequence of impulses with a frequency of one pulse approximately every two years.

2. QBOs IN SECTOR STRUCTURES

We have shown in our previous works [4, 5] concerning two- and four-sector structures that QBOs are manifest in four-sector structures, especially near phases 0.1, 0.35, 0.7, and 0.9 of the cycle, when the amplitude of the four-sector structure exceeds that of the two-sector structure; i.e., when the four-sector structure becomes quite important. It is difficult to know whether these maxima are associated with these points in the cycle or if they exhibit quasi-periodic fluctuations with a period of two to three years. Since there are four reference points and phases of maximum and minimum in each cycle, changes in the activity at these times could be interpreted as quasi-biennial oscillations. On the other hand, it is possible that precisely these two to three-yr fluctuations stimulate the abrupt changes in solar activity that we identify as the reference points of the cycle.

The most ordered structure with a quasi-period of two to three yrs is the difference between the periods of the two-sector and four-sector structures (T2–T4) and its spectrum at all latitudes (see Fig. 5 in [5]). Such oscillations in T2–T4 are much more significant than the 11-year periodicity. Their behavior varies slightly with time, and is virtually independent of the phase of the 11-year cycle. The latitude dependence is weak, probably indicating that they occur at a considerable depth. Apparently, the period of the 11-year oscillations is an eigenperiod for the regions in which the global magnetic field is generated, and these oscillations are in phase at the two levels where the two-sector and four-sector structures originate. Therefore, subtraction weakens both modes at this frequency considerably. At the same time, the QBOs are much more weakly phased. This may simply be due to their lower period or may have a more global physical nature—that these oscillations are external to both levels and there is some phase delay due to propagation between the levels. Since the oscillations

1063-7729/01/4512-1012$21.00

are out of phase, they are naturally attenuated much more weakly.

Here, we study biennial oscillations of the solar magnetic field in order to clarify their dependence on characteristic scales and structures. In Section 3, we calculate multipolar magnetic moments of various orders. The QBOs prove to be characteristic of the lowest harmonics; that is, they are global. In Section 4, we organize the data differently in order to study the zonal and sector structures separately. QBOs are more typical for sector than for zonal structures. In Section 5, we analyze oscillations of the magnetic moments of the polar and equatorial magnetic dipoles. The manifestations of QBOs in the polar and equatorial dipoles are essentially the same as those in the zonal and sector structures, respectively.

3. QBOs IN VARIATIONS OF THE MAGNETIC MOMENTS OF THE LARGE-SCALE MAGNETIC FIELDS

The intensities of various modes of the large-scale magnetic field and of polar and equatorial magnetic-field drifts have been studied using synoptic Hα maps of the solar magnetic field constructed for 1915–1999 using the technique of [1–3]. In order to compare the magnetic Hα maps with magnetograph measurements made at the Stanford Observatory, the synoptic maps were expanded in spherical harmonics, with the magnetic-field polarity being +1 G or −1 G [20, 21].

In a potential approximation expanding in spherical harmonics, we can express the solar magnetic field as a function of latitude θ, longitude φ, and the distance r from the center of the Sun:

$$B_r = \sum P_n^m(\cos\vartheta)(g_{nm}\cos m\varphi + h_{nm}\sin m\varphi) \times ((n+1)(R_O/R)^{n+1} - n(R/R_s)^{n-1}c_n), \quad (1)$$

$$B_\vartheta = -\sum \frac{\partial P_n^m(\cos\vartheta)}{\partial\vartheta}(g_{nm}\cos m\varphi + h_{nm}\sin m\varphi) \times ((R_O/R)^{n+2} + (R/R_s)^{n-1}c_n), \quad (2)$$

$$B_\varphi = -\sum \frac{m}{\sin\vartheta}P_n^m(\cos\vartheta) \times (h_{nm}\cos m\varphi - g_{nm}\sin m\varphi) \times ((R_O/R)^{n+2} + (R/R_s)^{n-1}c_n). \quad (3)$$

Here, $0 \le m \le n < N$ (we adopted $N = 9$), $c_n = -(R_O/R_s)^{n+2}$, P_n^m are Legendre polynomials, and g_{nm} and h_{nm} are the spherical-harmonic coefficients determined by the initial data. For the synoptic Hα maps, we took only the sign of the magnetic field, +1 G or −1 G for positive and negative fields, respectively. The expansion coefficients g_{nm} and h_{nm} provide all the necessary information to reconstruct the synoptic map and analyze the magnetic-field distribution.

We assume that the field remains potential up to the source surface, whose radius is $2.5R_0$, where R_0 is the radius of the solar photosphere. The technique is described in detail in [4, 20, 21]. The coefficients calculated at the Institute of Terrestrial Magnetism, Ionosphere, and Radiowave Propagation are available on the internet at the address http://helios.izmiran.rssi.ru/hellab/default.htm.

Let us consider the temporal behavior of harmonics with zonal numbers l varying from one to nine. We calculate the multipolar magnetic moments for each Carrington period via the formula

$$Mu_l(t) = \left(\sum_m \left(g_{nm}^2 + h_{nm}^2\right)\right)^{1/2}, \quad (4)$$

with the summation being performed over all m from 0 to l.

Figure 1 shows the Fourier spectrum of the magnetic moments calculated for the entire time interval. The frequency is in reciprocal years. The left half presents even harmonics ($l = 2, 4, 6, 8$), and the right half, odd harmonics ($l = 1, 3, 5, 7, 9$). We can see that the QBOs correspond to the processes in the solar atmosphere with the largest spatial scales, which are manifest only in low (global) harmonics ($l = 1, 2, 3$).

Figure 1 was constructed using the entire dataset and shows the average spectrum over the entire time covered by the observations. At the same time, it seems reasonable to suppose that the contribution of the QBOs to the total spectrum could be different for different time periods. Therefore, we used the wavelet and swan spectral methods to improve the temporal resolution.

We have used a "mexican hat" convolution function when applying the wavelet program [22]. The limiting window did not exceed a quarter of the realization length. The swan spectral analysis method [23] uses a Fourier expansion in moving intervals. The length of the moving interval was also a quarter of the realization length.

Figures 2a–2d present wavelet diagrams for the odd magnetic moments ($l = 1, 3, 5, 7$). We performed the calculations of periods in the range from 0.9 to 7.5 yrs. The periods of oscillations are plotted along the vertical axis in Fig. 2. QBOs with periods of about two years are clearly pronounced only in the first two moments ($l = 1, 3$), corresponding to the largest scales of the magnetic field, and are most clearly seen in the octupole moment. As expected, the QBOs are manifest differently at different times. They

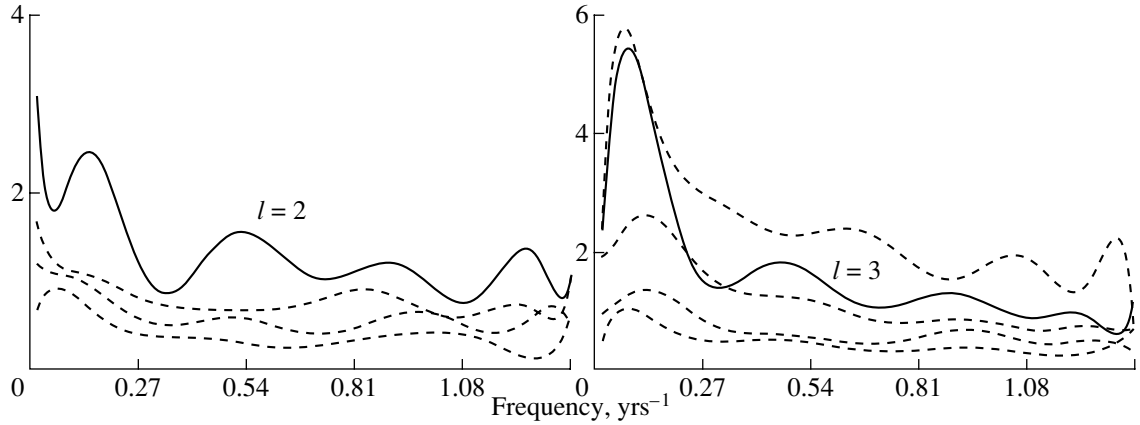

Fig. 1. Fourier spectra of the magnetic moments for the entire time interval under study. The frequencies in reciprocal Carrington periods are plotted along the horizontal axis and the spectral amplitudes along the vertical axis. The left half shows the spectra for even harmonics ($I = 2, 4, 6, 8$), and the right half, spectra for odd harmonics ($I = 1, 3, 5, 7, 9$).

are most intense for the dipole moment in the 18th cycle; in the octupole, this interval is broadened and encompasses the rising portion and maximum of the 19th cycle. Starting with $l = 5$, the spectrum for this period interval is abruptly attenuated during the entire time interval considered. Figures 3a and 3c present swan diagrams for two odd magnetic moments; the frequency is plotted along the horizontal axis. A horizontal strip at a frequency of 0.6 (i.e., a period of ≈ 1.7 yrs) can clearly be seen. The QBOs are pronounced in Fig. 3a ($l = 3$), while the spectrum for these periods is attenuated in Fig. 3c ($l = 1$). We can see that the QBOs display fine structure, demonstrating a set of oscillations with periods from two to three yrs, which evolve in different ways in time. In particular, energy was gradually transferred to lower frequencies, and there was a brief disappearance of the QBOs in the early 1960s.

It is interesting that the QBOs are also pronounced in the low even harmonic $l = 2$ (plot not shown), which determines the mutual asymmetry of the global field in the northern and southern hemispheres. This is consistent with the fact that the QBOs are clearly seen in the total Fourier spectrum in both even and odd low harmonics.

These results definitively demonstrate that the two-year oscillations have a global character. Here, we note that it was shown in [24] that precisely the harmonics displaying QBOs are correlated with the Wolf number with a delay of five to six yrs; such delays are typical for the global fields.

4. RELATIVE CONTRIBUTIONS OF ZONAL AND SECTOR MAGNETIC-FIELD STRUCTURES TO QBOs

Energy indices for the global magnetic field were introduced in [25, 26]. The meaning of these indices is the following. Let the square of the radial component of the magnetic field averaged over some spherical surface with radius R from the center of the Sun be the energy index $i(B_r)$:

$$i(B_r)|_R = \langle B_r^2 \rangle. \quad (5)$$

Using (1), we obtain for the source surface

$$i(B_r)|_{R_s} = \sum_{lm} (2l+1)\,\zeta^{2l+4}\left(g_{lm}^2 + h_{lm}^2\right), \quad (6)$$

where $\zeta = 0.4$.

We can also introduce partial indices, namely: the zonal-even index ZE [in this case, formula (4) contains only terms with $m = 0$ and even l]; zonal-odd index ZO ($m = 0, l = 2k + 1$); sector-even index SE ($m = l = 2k$); and sector-odd index SO ($m = l = 2k + 1$). Note that these indices were introduced in order to analyze direct measurements of the magnetic field and represent the average energy of the magnetic field or some of its components on a selected surface.

When using magnetic fields reconstructed from Hα measurements, these indices no longer have a direct physical meaning. However, they undoubtedly remain helpful, since they characterize the relative contributions and cycle phase variations of the zonal and sector structures [24]. Note that the SO index describes the contribution of the most common two-sector structures and other structures with $2m$ sectors, where m is odd. The SE index describes the contribution of the four-sector structures and other structures with $2m$ sectors, where m is even. It was shown in [24] that the zonal structure is most important for the global magnetic field.

The spectra calculated from the Hα data using the wavelet (Figs. 2e, 2f) and swan (Fig. 3) programs show that the QBOs are manifest most clearly in the odd sector SO structures (Fig. 3b) and much

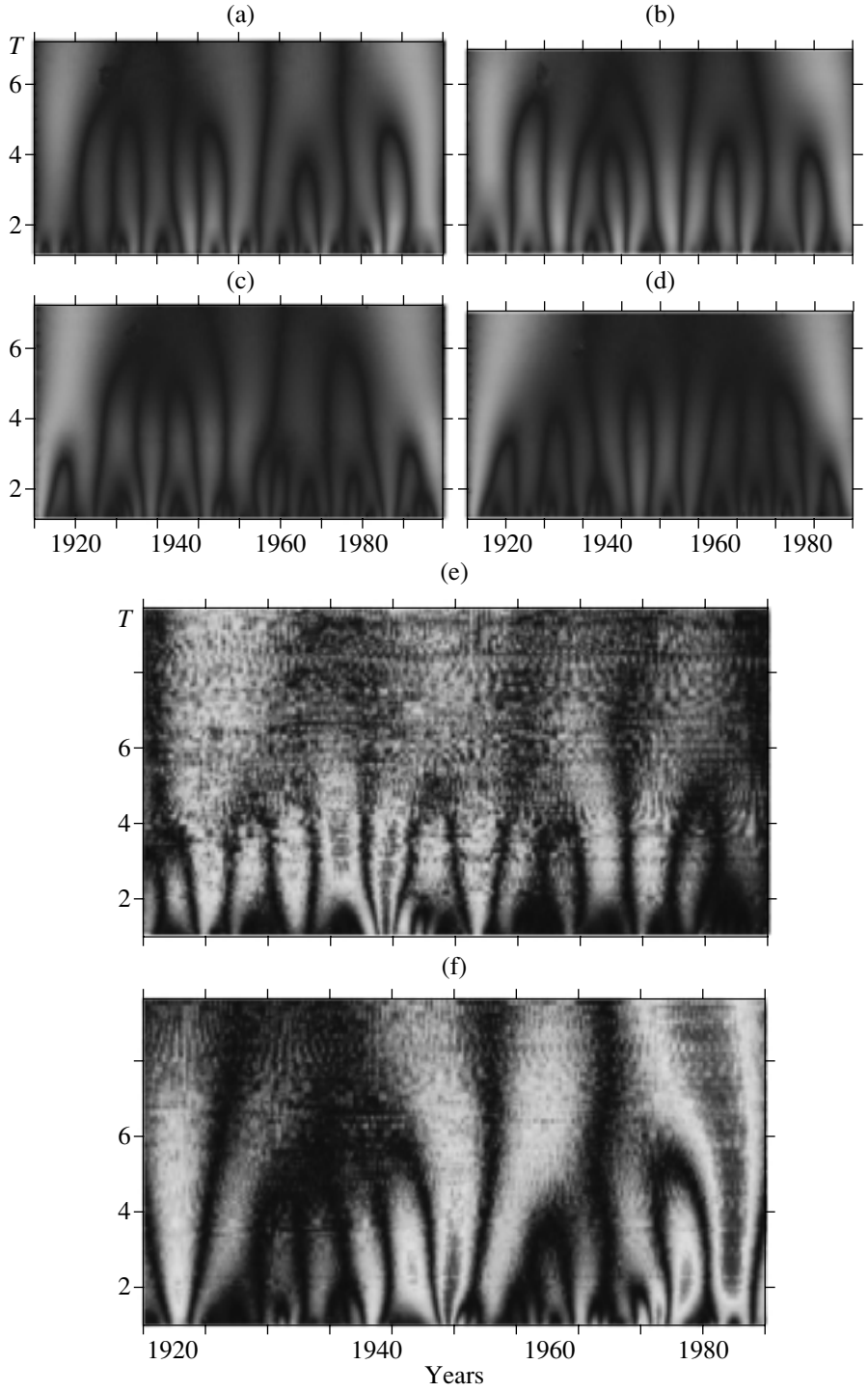

Fig. 2. Wavelet diagrams for the odd magnetic moments (a) $l = 1$, (b) 3, (c) 5, and (d) 7 with periods in the range from 0.9 to 7.5 yrs, and for the (e) odd sector structures and (f) odd zonal structures.

more weakly in the odd zonal ZO structures (Fig. 3d). The SO structures clearly display short-period oscillations with maxima at 1.6–2.0 and 3.0 yrs, which are present during virtually the entire time interval. The ZO structures display QBOs much more seldom (near 1920, 1950, and 1985). Similar to the behavior of the magnetic moments (Fig. 2), there is a gradual transfer of the energy of oscillations in SO and ZO structures to longer periods. This is especially pronounced in Fig. 2 for $l = 3$. After the end of

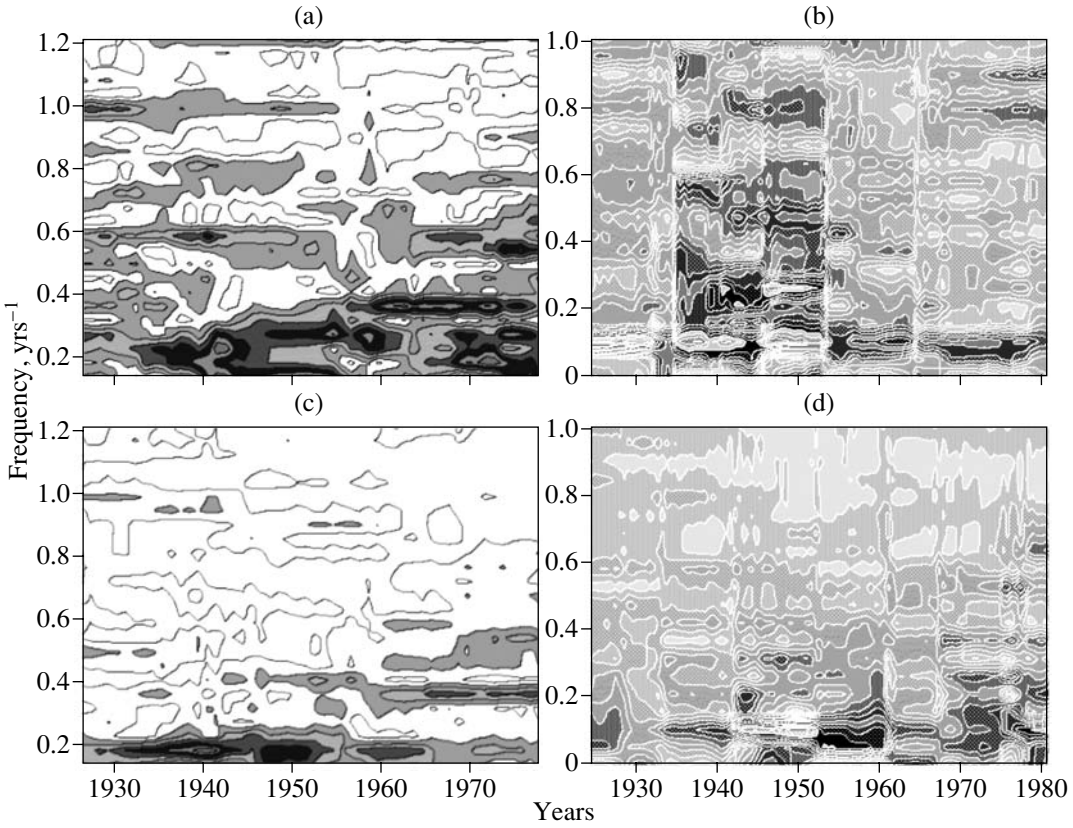

Fig. 3. Swan diagrams for the two odd magnetic moments (a) $I = 3$ and (c) $I = 1$, (b) odd sector structures SO, and (d) odd zonal structures ZO. The entire time interval in years is plotted on the horizontal axis and the periods in fractions of a year are plotted on the vertical axis.

the 18th cycle, the energy of short-period oscillations decreases, but increases again at the beginning of the 21st cycle.

We have compared the QBO for all types of indices derived from direct measurements of the magnetic field (the Stanford Observatory data) and from Hα data. A detailed description of this comparison is presented in [24], with an analysis of the SO indices being of particular interest. While, in the Stanford data, QBOs in the SO index are visible only near maxima of the cycles of local fields, in the Hα data they can clearly be seen during the entire interval considered. Since the contribution of local fields is weakened in the Hα data in comparison with the direct magnetic-field measurements, this clear expression of the QBOs provides evidence that these oscillations have a global character.

5. QBOs OF THE EFFECTIVE DIPOLE

Figure 2 shows that the 11-year oscillations dominate in Mu_1, which is the largest-scale component in the magnetic-moment expansion of the global magnetic field. However, note that Mu_1 contains two components with different spatial-temporal behaviors: we shall call these the magnetic moments of the polar D_v and equatorial D_h dipoles:

$$D_v = g_{10}, \tag{7}$$

$$D_h = \left(g_{11}^2 + h_{11}^2\right)^{1/2}. \tag{8}$$

D_v is predominantly determined by the main zonal component of the global field and reaches its maximum at the Wolf number minimum. D_h is associated with the two-sector structure, which is always present at every phase of the solar cycle [24]. The wavelet and swan diagrams obtained show that the QBOs in the vertical and horizontal dipoles are manifest similarly to those in the ZO and SO indices, respectively.

QBOs are continually present in the SO and D_h oscillations; i.e., they are associated with variations of the prominence of the two-sector structure.

6. CONCLUSIONS

We have arrived at the following main conclusions.

(1) First and foremost, the QBOs are manifest in oscillations of the very first harmonics of the global

magnetic field. In variations of the higher harmonics corresponding to medium-scale fields (down to the scales of active regions), QBOs are weakly expressed. The indices derived from the Stanford data (i.e., taking into account the field strength) do not display QBOs at cycle minima. At the same time, data constructed from Hα maps (i.e., mainly taking into account the field structure but not its strength) show comparable QBOs during the entire interval under study.

(2) QBOs are mainly displayed in variations of the sector structure of the large-scale magnetic field. Thus, the QBOs primarily represent variations of the equatorial dipole (and probably to a lesser extent of the quadrupole). Therefore, they are clearly seen in the large-scale magnetic fields and the locations of active longitudes [8], long-term dynamics of sunspot indices [9], geomagnetic activity [10, 11], displacement of magnetic neutral lines [16], and the heliospheric magnetic fields [19].

(3) The intensity of the QBOs varies with time and was maximum in the middle of the 20th century. The solar rotation reached its minimum precisely at that time [4, 5, 27]. It remains unclear if there is a relationship between these two phenomena.

ACKNOWLEDGMENT

This work was supported by the Russian Foundation for Basic Research (project no. 99-02-18346).

REFERENCES

1. V. N. Obridko and B. D. Shelting, in *Modern Problems of Solar Cyclicity* [in Russian], Ed. by V. I. Makarov and V. N. Obridko (Glavn. Astron. Obs., St. Petersburg, 1997), p. 193.
2. V. N. Obridko and B. D. Shelting, Sol. Phys. **184**, 187 (1999).
3. V. N. Obridko and B. D. Shelting, in *The New Solar Activity Cycle: Observational and Theoretical Aspects* [in Russian], Ed. by V. I. Makarov and V. N. Obridko (Glavn. Astron. Obs., St. Petersburg, 1998), p. 137.
4. V. N. Obridko and B. D. Shelting, Astron. Zh. **77**, 124 (2000) [Astron. Rep. **44**, 103 (2000)].
5. V. N. Obridko and B. D. Shelting, Astron. Zh. **77**, 303 (2000) [Astron. Rep. **44**, 262 (2000)].
6. E. E. Benevolenskaya and V. I. Makarov, Soln. Dannye, No. 2, 89 (2000).
7. V. I. Makarov, V. V. Makarova, and A. G. Tlatov, Soln. Dannye, No. 2, 89 (1991).
8. I. V. Ivanov, Soln. Dannye, No. 2, 91 (1991).
9. G. V. Kuklin and L. A. Plyusnina, Soln. Dannye, No. 2, 95 (1991).
10. G. S. Ivanov-Kholodnyĭ and V. E. Chertoprud, Soln. Dannye, No. 2, 96 (1991).
11. D. I. Ponyavin, Soln. Dannye, No. 2, 99 (1991).
12. Yu. R. Rivin and V. N. Obridko, Astron. Zh. **69**, 1083 (1992) [Sov. Astron. **36**, 557 (1992)].
13. V. N. Obridko and Yu. R. Rivin, Izv. Akad. Nauk, Ser. Fiz. **59** (9), 110 (1995).
14. V. N. Obridko and Yu. R. Rivin, Astron. Astrophys. **308**, 951 (1996).
15. V. N. Obridko and Yu. R. Rivin, Astron. Zh. **74**, 83 (1997) [Astron. Rep. **41**, 76 (1997)].
16. V. I. Makarov, K. S. Tavastsherna, A. G. Tlatov, and D. K. Callebaut, in *The New Solar Activity Cycle: Observational and Theoretical Aspects* [in Russian], Ed. by V. I. Makarov and V. N. Obridko (Glavn. Astron. Obs., St. Petersburg, 1998), p. 115.
17. K. Labitzke and H. van Loon, Ann. Geophys. **11**, 1084 (1993).
18. G. S. Ivanov-Kholodnyĭ, E. I. Mogilevskiĭ, and V. E. Chertoprud, Geomagn. Aeron. (2000) (in press).
19. I. S. Veselovskiĭ, A. V. Dmitriev, A. V. Suvorova, and Yu. S. Minaeva, Astron. Vestn. **34** (1), 82 (2000).
20. J. T. Hoeksema and P. H. Scherrer, *The Solar Magnetic Field 1976 through 1985* (US Department of Commerce, Boulder, 1986).
21. J. T. Hoeksema, *The Solar Magnetic Field 1985 through 1990* (US Department of Commerce, Boulder, 1991).
22. N. M. Astaf'eva, Usp. Fiz. Nauk **166** (11), 1145 (1996) [Phys. Usp. **39**, 1085 (1996)].
23. A. Dzewonski, S. Block, and M. Landisman, Bull. Seismol. Soc. Am. **59**, 427 (1969).
24. V. I. Makarov, V. N. Obridko, A. Tlatov, and B. D. Shelting, Sol. Phys. (2001) (in press).
25. B. D. Shelting, V. N. Obridko, and F. A. Ermakov, Astron. Tsirk., No. 1540, 23 (1989).
26. V. N. Obridko and B. D. Shelting, Sol. Phys. **137**, 167 (1992).
27. V. N. Obridko and B. D. Shelting, Sol. Phys. (2001) (in press).

Translated by V. Badin

Astronomy Reports, Vol. 45, No. 12, 2001, pp. 929–934. Translated from Astronomicheskiĭ Zhurnal, Vol. 78, No. 12, 2001, pp. 1059–1065.

Microlensing by a Noncompact Spheroidal Gravitational Lens

M. B. Bogdanov

Chernyshevskiĭ State University, ul. Moskovskaya 155, Saratov, 410601 Russia

Received March 19, 2001

Abstract—In the process of their evolution, small-scale clusters of weakly interacting massive particles (WIMPs) that formed in the early Universe can acquire rotational momentum and spheroidal shape. Even small oblateness of a cluster similar to that of the critical Roche surface can lead to the appearance of caustics in the plane of a source lensed by the object. The multiple source images that form in this case cannot be resolved in modern observations, and the cluster behaves like a noncompact spheroidal lens. The caustic crossing that occurs in the case of relative motion of the observer, the cluster of particles, and the lensed star can produce a large variety of flux curves, including those such as have been observed during microlensing events and interpreted as manifestations of binary gravitational lenses. Therefore, we cannot rule out the possibility that at least some of these events might actually be associated with clusters of WIMPs. © *2001 MAIK "Nauka/Interperiodica"*.

1. INTRODUCTION

One approach to the solution of the dark-matter problem supposes the existence of weakly interacting massive particles (WIMPs) that formed at an early stage of the evolution of the Universe. Because of their gravitational interaction, these particles should have produced a hierarchical structure of clusters with certain scaling properties [1]. The masses of the smallest objects are of the order of a solar mass. The particles interact weakly both with each other and with external matter, so that the detection of such clusters seems very unlikely. Gurevich and Zybin [2] pointed out that, if such objects are located along the line of sight connecting an observer and a normal star, they can deflect the light rays from the star; in view of the masses of the clusters involved, this can be considered gravitational microlensing.

Byalko [3] and Paczynski [4] were the first to provide a theoretical basis for the possibility of observing gravitational microlensing of stars by compact clusters of dark matter. Since then, several groups of observers have undertaken searches for the effects of microlensing of stars by massive compact halo objects (MACHOs), efforts that eventually were successful in 1993 [5]. Despite the small probability of such events, the MACHO, OGLE, GMAN, PLANET, and other international teams have already observed several hundred microlensing events for stars of the Magellanic Clouds and Galactic bulge. The results of these observations are of great interest both for refining our knowledge of the structure of the Galaxy and for very high angular resolution analyses of the brightness distributions over the disks of the lensed stars [6–9]. More detailed information about microlensing of stars can be found in [10, 11]. Recent data indicate that the masses of the gravitational lenses lie in the interval 0.15–$0.90 M_{\odot}$; however, the nature of these objects remains unclear. The flux-variation curves for most events can adequately be described by point-lens models (Schwarzschild lenses). In some cases, the observed manifestations of caustics appear to indicate that the corresponding gravitational lenses are binary.

Gurevich *et al.* [12] were the first to compute flux-variation curves for the gravitational microlensing of stars by compact lenses made up of WIMP clusters. The shapes of these curves can be rather similar to those of a Schwarzschild lens [13, 14], with a symmetric profile and a sharp maximum, albeit with broader wings. In their comparison of these curves with observational data obtained by the OGLE group, Sazhin *et al.* [15] showed that in two of eight cases the observed light curves can be better described by a noncompact lens model. Later, however, it was shown that the broadening of the wings of these flux curves can also be explained in a simpler way—by either blending [16] or by the radiation of the lens itself, if it is a normal star [17].

Recently, Zakharov [18] analyzed a spherically symmetric nonsingular model for a noncompact gravitational microlens, which describes the expected density distribution in a WIMP cluster better than earlier models. Under certain conditions, such a microlens can produce a symmetric lensing curve with

1063-7729/01/4512-0929$21.00

two maxima and a dip between them. Similar curves can also be produced by binary gravitational lenses and have already been observed in some microlensing events.

The aim of the current paper is to analyze a nonsingular model for a noncompact spheroidal microlens produced by a rotating cluster of particles. We show below that this model can qualitatively describe nearly any microlensing curve shape observed thus far.

2. POSSIBLE BREAKDOWN OF THE SPHERICAL SYMMETRY OF A WIMP CLUSTER

Gurevich *et al.* [1] fitted the mass density of dark-matter particles in a small-scale noncompact object with the following function of the distance r from the center of the object:

$$\rho(r) = \begin{cases} \rho_0, & 0 \le r \le r_c \\ \rho_0 (r/r_c)^{-\alpha}, & r_c \le r \le R_x \\ 0, & r > R_x. \end{cases} \qquad (1)$$

The exponent in (1) is also a scaling parameter, equal to $\alpha = 1.8$. The radius of the core, which has a constant density ρ_0, is denoted r_c and can range from 0.05 to 0.1 of the cluster radius R_x. Integration of (1) shows that the mass M_x of the object is related to the distribution parameters by the formula

$$M_x = \frac{4\pi\rho_0}{3-\alpha}\left(r_c^\alpha R_x^{3-\alpha} - \frac{\alpha}{3} r_c^3\right). \qquad (2)$$

According to [1], a typical cluster has a mass of $M_x = 0.1\text{–}1.0 M_\odot$ and a radius of $R_x \sim 10^{14}\text{–}10^{15}$ cm.

In reality, the spherical symmetry of the density distribution in a noncompact object can break down. One factor that can lead to such a disruption of the symmetry is the tidal deformation of WIMP clusters as a result of their interactions with each other or with stars of the Galaxy. The possibility of such deformations was pointed out by Gurevich *et al.* [1]. However, the probability of a close encounter involving appreciable tidal forces is very low. Another factor—the oblateness of the particle cluster by rotation—seems more likely.

Note that, even if the density distribution in the cluster is spherically symmetric, the resulting gravitational lens is subject to the gravitational field of the Galaxy, an effect referred to as the quadrupole lens. A detailed description can be found in [13], and we do not consider this effect further here.

Rotation is a general property of systems that form as a result of the gravitational condensation of matter. Rotation explains, for example, the observed oblate shapes of elliptical galaxies and globular star clusters. In the origin of rotation in such systems, an important role should be played by gas-dynamical effects, which are obviously absent in the case of weakly interacting particles. There is, however, a mechanism capable of inducing rotation of the particles exclusively via gravitational interactions. This mechanism, first suggested by Hoyle [19] and then developed in more detail by Peebles [20], is based on the mutual attraction of tidally deformed clusters. In this case, the orbital momentum associated with the relative motion of the clusters is transformed into rotational momentum of each of the interacting clusters. In the early Universe, when WIMP clusters formed, their spatial density was substantially higher than now. Close encounters occurred rather frequently, and the Hoyle–Peebles mechanism could be fairly efficient.

3. DISTRIBUTION OF SURFACE MASS DENSITY FOR A NONCOMPACT SPHEROIDAL MICROLENS

The observed manifestations of a gravitational lens depend on the distribution of the surface mass density $\Sigma(\xi)$, where ξ is a vector defining the position of a point in the plane of the lens. Here and below, we write vector names in bold font. For the spherically symmetric law (1) in a coordinate system whose origin coincides with the projection of the center of the particle cluster onto the plane of the lens, $\Sigma(\xi)$ is given by the integral

$$\Sigma(\xi) = 2\int_0^{\sqrt{R_x^2-\xi^2}} \rho\left(\sqrt{\xi^2+z^2}\right) dz. \qquad (3)$$

It is obvious that the distribution of the surface mass density in this case is rotationally symmetric. Further, we consider the dimensionless density

$$\kappa(\xi) = \Sigma(\xi)/\Sigma_{cr}, \qquad (4)$$

where the so-called critical density Σ_{cr} is determined by the relation

$$\Sigma_{cr} = \frac{c^2 D_s}{4\pi G D_d D_{ds}}. \qquad (5)$$

In (5), c is the speed of light, G the gravitational constant, D_s the distance between the observer and lensed source, D_d the distance between the observer and lens, and D_{ds} the distance between the lens and source.

Let us adopt the radius of the cluster R_x as a scaling parameter ξ_0 and introduce dimensionless vectors in the plane of the lens $\mathbf{x} = \xi/\xi_0$ and the plane of the source $\mathbf{y} = \eta/\eta_0$, where $\eta_0 = \xi_0 D_s/D_d$, $\xi_0 = R_x$, $\mathbf{x}(x_1, x_2)$, and $\mathbf{y}(y_1, y_2)$. We use $\alpha(\mathbf{x})$ to denote the normalized vector $\alpha^0(\xi_0\mathbf{x})$:

$$\boldsymbol{\alpha}(\mathbf{x}) = \frac{D_d D_d s}{\xi_0 D_s}\boldsymbol{\alpha}^0(\xi_0\mathbf{x}).$$

The gravitational lens equation [13, 14] can then be written in the form

$$\mathbf{y} = \mathbf{x} - \boldsymbol{\alpha}(\mathbf{x}). \quad (6)$$

We estimated integral (3) numerically to an accuracy of 10^{-5} for $r_c = 0.07R_x$. The resulting distribution $\kappa(x)$ is shown by the solid curve in Fig. 1. We set the dimensionless density at the lens center equal to unity.

The possibility of WIMP clusters being oblate by rotation can hardly provoke any fundamental objections. However, the questions of the oblate cluster's shape and density distribution have no simple answers. The branch of celestial mechanics that studies the equilibrium shapes of rotating bodies assumes them to be comprised of a viscous incompressible fluid, which is clearly inappropriate for systems of weakly interacting particles. Nonetheless, some conclusions may be of interest for our case as well. Given the presence of a small dense core and a rapid decrease of the particle density with distance from the cluster center, we can describe this density distribution to a first approximation using a Roche model, which assumes that the entire mass of the rotating body is concentrated at its center [21]. This type of model has been used earlier to study planetary atmospheres and protoplanetary disks. The oblateness of the marginally stable surface of the Roche model was fairly small, with a polar-to-equatorial-axis ratio equal to 2/3 [21].

Models with a nonsingular power-law elliptical distribution of the surface mass density have been widely used in studies of transparent gravitational lenses:

$$\kappa(\mathbf{x}) = \frac{q}{(u^2 + x_1^2 + ex_2^2)^n}. \quad (7)$$

This model has a constant-density core of radius u at the center. The contours of equal surface density are ellipses with fixed semiminor to semimajor axis ratio $e = b/a$. Models of the form (7) are believed to adequately describe the surface mass density distributions in galaxies for a wide range of degrees of oblateness.

We first analyzed the case of a nonrotating cluster and tried to fit the density distribution of a WIMP cluster (4) using the model (7) with $e = 1$, choosing model parameters to minimize the sum of squared residuals. The solution of the corresponding optimization problem on a uniform 200-point grid yielded the best-fit parameter values $q = 1.04$, $u = 0.09$, and $n = 0.68$. The dashed curve in Fig. 1 shows the surface density distribution for model (7) with these parameters, which is a good fit to the initial distribution.

We then assumed that, as the particle cluster rotates, the parameters q, u, and n remain constant and the ellipses of equal density experience oblateness equal to that of the marginally stable surface in the Roche model: $e = 2/3$.

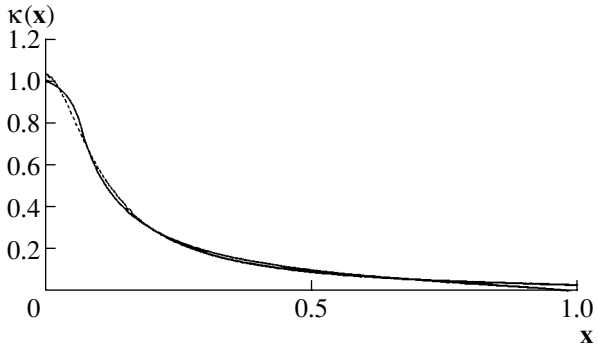

Fig. 1. Distributions of the dimensionless surface mass density for a small-scale cluster of weakly interacting massive particles (solid curve) and the nonsingular power-law elliptical model (7) with $q = 1.04$, $u = 0.09$, $n = 0.68$, and $e = 1$ (dashed curve).

4. COMPUTATION OF THE CRITICAL AND CAUSTIC CURVES

It is well known that a transparent gravitational lens with surface density distribution (7) can have caustics in the source plane, which, when crossed by a lensed star, can produce a large variety of light-curve shapes. For this to happen, it is sufficient for a point $\mathbf{x}$ with $\kappa(\mathbf{x}) > 1$ to exist in the plane of the lens [13, 14]. This condition can be satisfied by the particle clusters considered. Let us fix $R_x = 10^{14}$ cm and $M_x = 0.5M_\odot = 10^{33}$ g. It then follows from (2) that $\rho_0 = 1.8 \times 10^{-8}$ g/cm^3, and the computation of integral (3) yields a surface density of $\Sigma(0) = 3.4 \times 10^5$ g/cm^2 at the lens center. We find from (5) that the critical density is $\Sigma_{cr} = 5.3 \times 10^4$ g/cm^2 and $\Sigma_{cr} = 1.7 \times 10^5$ g/cm^2 for typical cases of lensing of stars in the Large Magellanic Cloud by an object located in the Galactic halo ($D_d = 8$ kpc, $D_s = 46$ kpc, and $D_{ds} = 38$ kpc) and lensing of Galactic bulge stars ($D_d = 4$ kpc, $D_s = 8$ kpc, and $D_{ds} = 4$ kpc), respectively. Thus, the required excess of the density over its critical level is quite possible.

Let us assume for the sake of simplicity that the rotational axis of the cluster lies in the plane of the lens and that the major axes of the ellipses of equal surface density form intervals on the x_1 axis. Barkana [22] has developed an efficient algorithm for solving the gravitational-lens equation (6) using the density distribution (7) and written a FORTRAN code implementing this algorithm. For a given vector $\mathbf{x}$,

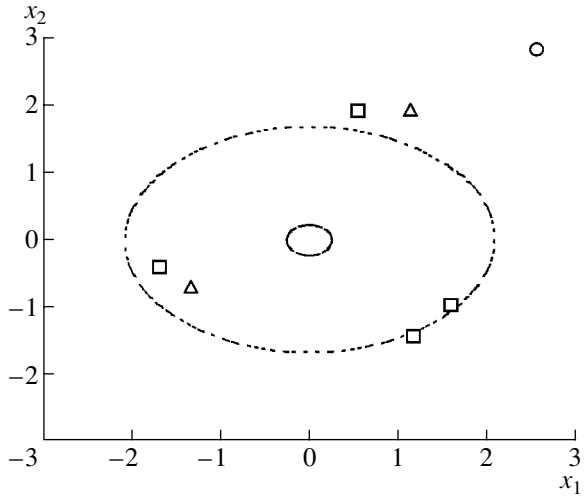

Fig. 2. Critical curves in the plane of the lens (dashed). The symbols indicate the positions of images of the three sources shown in Fig. 3.

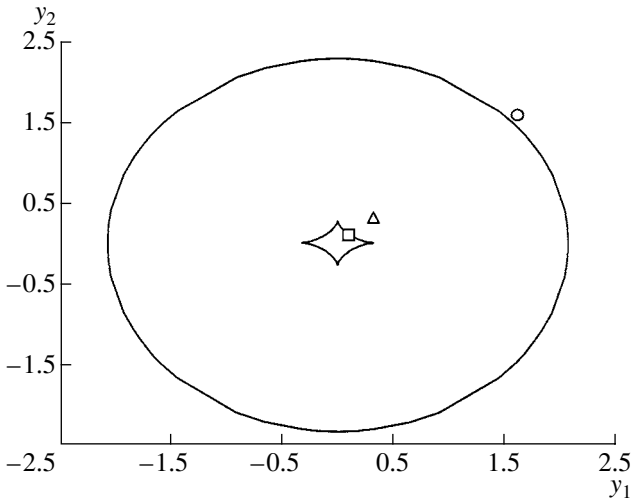

Fig. 3. Caustic curves of the lens in the plane of the source (solid). The symbols indicate the positions of three sources, whose images are shown in Fig. 2.

the code computes the components of the deflection-angle vector $\alpha(\mathbf{x})$ and the elements of the Jacobi matrix $A_{i,j} = \partial y_i/\partial x_j$.

To verify the operation of this code, we used it to compute lensing effects for a nonsingular isothermal model of an elliptical gravitational lens. In this case, the parameters of interest can be expressed analytically by formulas presented by Schneider *et al.* [13] and Zakharov [14]. However, since these formulas are rather cumbersome, we applied Schneider's FORTRAN code based on exact formulas, which is available from his Internet site. The errors in the quantities computed using Barkana's code did not exceed 10^{-5} in any of the examples we considered.

Our computations for model (7) with the parameters adopted here demonstrated the existence of critical curves in the plane of the lens, defined by the condition $\det A = 0$. These are shown by the dashed curves in Fig. 2; the corresponding caustics are shown by the solid curves in Fig. 3. The outer and inner caustics correspond to the inner and outer curves, respectively. When a point source crosses the caustic, the gravitational lens amplification factor $\mu = 1/|\det A|$ can formally approach infinity. For a source with a finite angular size, μ is finite but can achieve rather large values.

It is well known that a lens with a system of caustics such as that shown in Fig. 3 is capable of producing multiple source images. To illustrate this in the case of our noncompact lens model, we chose three point sources located along the diagonal of the first quadrant at $y_1 = y_2 = 1.60$, 0.32, and 0.10, shown in Fig. 3 by a circle, triangle, and square, respectively. We determined the images of each source by searching for roots of the lens equation (6) on grids with decreasing cell size down to $\Delta x_1 = \Delta x_2 = 0.0001$. The resulting positions of the source images are shown by the corresponding symbols in Fig. 2, and their coordinates are given in the table, which also gives for each image the corresponding determinant of the Jacobi matrix $\det A$, its trace $\mathrm{Sp}A$, and the amplification factor μ. The last column of the table gives the type of the image: I (positive parity, or direct image; $\det A > 0$, $\mathrm{Sp}A > 0$) or II (negative parity, or inverted; $\det A < 0$). The images of each source are numbered in order of increasing x_1.

At first glance, our results seem to contradict the well-known theorem of Burke [23], which states that the number of images produced by a transparent gravitational lens with a limited deflection angle must always be odd. Bray [24] showed that this conflict is a result of the finite accuracy of the computed $\boldsymbol{\alpha}(\mathrm{x})$ and the discrete coordinate grid used. As a result, two images can essentially blend and become unresolved in Fig. 2. A comparison of our results with those from the analytical study of Bourassa and Kantowski [25] for a qualitatively similar model with a Schmidt density distribution shows that, when the source is located inside the caustic boundaries, the missing image should be located in the third quadrant and merge with image number one. In this case, this image should be of type III (positive parity or twice inverted; $\det A > 0$, $\mathrm{Sp}A > 0$) in order for the consequence of the Burke theorem $n_{\mathrm{I}} + n_{\mathrm{III}} = 1 + n_{\mathrm{II}}$ to be satisfied, where n with a subscript denotes the number of images of the corresponding type.

Characteristics of images of three sources produced by a noncompact spheroidal gravitational lens

No.	x_1	x_2	$\det A$	$\mathrm{Sp}A$	μ	Type
Source 1 ($y_1 = y_2 = 1.60$)						
1	2.5343	2.7988	0.6847	1.7320	1.46	I
Source 2 ($y_1 = y_2 = 0.32$)						
1	−1.3284	−0.6848	−0.5288	0.9157	1.89	II
2	1.1243	1.9166	0.3215	1.4856	3.11	I
Source 3 ($y_1 = y_2 = 0.10$)						
1	−1.6759	−0.3928	−0.3050	1.0344	3.28	II
2	0.5397	1.9054	0.2240	1.4325	4.46	I
3	1.1680	−1.4322	0.0488	1.3055	20.48	I
4	1.5855	−0.9735	−0.0527	1.2170	18.98	II

5. RESULTS AND DISCUSSION

For the adopted size of the particle cluster, the unit scale length in the plane of the lens for $D_d = 4$ kpc corresponds to an angle of $0''.0017$, which is much smaller than the resolution of current telescopes. As a result, the object should show up as a microlens, with the total flux from all its images being observed. Due to the orbital motion of the observer, particle cluster, and lensed star, the observed flux should vary with time. Exact computation of the light curves is very computer intensive and does not seem justified. However, it is easy to obtain a qualitative description of the observational picture.

When a source of finite angular size crosses the outer caustic, two additional source images should appear in Fig. 3 and the observed flux should increase. However, the flux amplification factor on this caustic is comparatively small, and the caustic crossing could escape detection. When the source crosses the inner caustic, two more source images appear, resulting in a sharp increase of the flux followed by a slower decrease. At the second crossing of the inner caustic, the two images merge and disappear, inverting the pattern of the flux variations. When the line of the relative motion of the lensed star in Fig. 3 passes far from the cusp and is parallel to the coordinate axes when it crosses the inner caustic, the flux-variation curves have symmetric profiles with two maxima and a dip at the center. Such curves can be realized in the noncompact microlens model analyzed by Zakharov [18]. If the star moves along a line at some angle to the y_1 axis, either the first or second crossing of the inner caustic should take place closer to the corresponding cusp. As a result of the difference in the amplification factors, the light curve becomes asymmetric and either its first or second maximum becomes stronger. Similar light-curve shapes can appear in the cases of binary gravitational lenses and have been observed in actual microlensing events.

When the star goes beyond the outer caustic, comparative modest flux variations will again be observed as a flux increase followed by a more abrupt decrease. If the lensed star does not cross the outer caustic, the flux-variation curve is symmetrical and has a single maximum.

The microlensing pattern considered above depends on a large number of parameters. Obviously, it is possible to obtain a large variety of light curves by changing the lens orientation and varying the parameters for the density distribution and the relative motion of the lensed star. The caustic manifestations observed in a number of microlensing events could therefore be associated with noncompact clusters of weakly interacting particles.

6. CONCLUSIONS

Our analysis shows that small-scale clusters of weakly interacting massive particles can, in the course of their evolution, acquire rotational momentum and spheroidal shape. Even a small degree of oblateness similar to that of the critical surface for a Roche model can result in the appearance of caustics in the plane of a lensed source. The multiple images that form cannot be resolved using current telescopes, and the cluster is manifest as a noncompact, spheroidal gravitational microlens. The crossing of caustics in the case of relative motion of the observer, particle cluster, and lensed star can produce a large variety of flux curves, including some observed in actual microlensing events that have been interpreted as manifestations of binary gravitational lenses. We must therefore bear in mind the possibility that at least some such events could in reality be associated with WIMP clusters.

The accuracy of photometric measurements in crowded stellar fields observed during searches for microlensing events is comparatively low. Moreover, observational datasets inevitably have gaps. At the same time, microlensing by a noncompact, spheroidal lens is characterized by a large number of free parameters whose variation can provide a satisfactory agreement with observational data. Therefore, analyses of light curves alone cannot be used to distinguish a WIMP cluster lens from, for example, a binary gravitational lens with orbital motion of its components. Other tools must be used to identify the lensing objects. In the case of noncompact neutralino lenses, one such tool is detection of gamma-ray emission produced by the annihilation of these particles [1].

7. ACKNOWLEDGMENTS

I am grateful to R. Barkana and P. Schneider for sharing their computer codes and to A.F. Zakharov for reading the article and making comments. This work was supported by the Universities of Russia Program and the Competitive Center for Fundamental Science.

REFERENCES

1. A. V. Gurevich, K. P. Zybin, and V. A. Sirota, Usp. Fiz. Nauk **167**, 913 (1997) [Phys. Usp. **40**, 869 (1997)].
2. A. V. Gurevich and K. P. Zybin, Phys. Lett. A **208**, 276 (1995).
3. A. V. Byalko, Astron. Zh. **46**, 998 (1969) [Sov. Astron. **13**, 784 (1969)].
4. B. Paczynski, Astrophys. J. **304**, 1 (1986).
5. C. Alcock, C. W. Akerlof, R. A. Allsman, *et al.*, Nature **365**, 621 (1993).
6. C. Alcock, W. H. Allen, R. A. Allsman, *et al.*, Astrophys. J. **491**, 436 (1997).
7. M. D. Albrow, J.-P. Beaulieu, J. A. R. Caldwell, *et al.*, Astrophys. J. **522**, 1011 (1999).
8. M. B. Bogdanov and A. M. Cherepashchuk, Astron. Zh. **76**, 688 (1999) [Astron. Rep. **43**, 601 (1999)].
9. M. B. Bogdanov and A. M. Cherepashchuk, Astron. Zh. **77**, 842 (2000) [Astron. Rep. **44**, 745 (2000)].
10. A. F. Zakharov and M. V. Sazhin, Usp. Fiz. Nauk **168**, 1041 (1998) [Phys. Usp. **41**, 945 (1998)].
11. C. Alcock, R. A. Allsman, D. R. Alves, *et al.*, Astrophys. J. **542**, 281 (2000).
12. A. V. Gurevich, K. P. Zybin, and V. A. Sirota, Phys. Lett. A **214**, 232 (1996).
13. P. Schneider, J. Ehlers, and E. E. Falco, *Gravitational Lenses* (Springer-Verlag, Berlin, 1992).
14. A. F. Zakharov, *Gravitational Lens and Microlens* [in Russian] (Yanus-K, Moscow, 1997).
15. M. V. Sazhin, A. G. Yagola, and A. V. Yakubov, Phys. Lett. A **219**, 199 (1996).
16. P. Wozniak and B. Paczynski, Astrophys. J. **487**, 55 (1997).
17. M. B. Bogdanov and A. M. Cherepashchuk, Astron. Zh. **75**, 261 (1998) [Astron. Rep. **42**, 229 (1998)].
18. A. F. Zakharov, Astron. Zh. **76**, 379 (1999) [Astron. Rep. **43**, 325 (1999)].
19. F. Hoyle, in *Problems of Cosmical Aerodynamics* (Central Air Documents Office, Dayton, 1949), p. 195.
20. P. J. E. Peebles, Astrophys. J. **155**, 393 (1969).
21. M. F. Subbotin, *Course of Celestial Mechanics* [in Russian] (Gostekhizdat, Moscow, 1949), Vol. 3.
22. R. Barkana, Astrophys. J. **502**, 531 (1998).
23. W. L. Burke, Astrophys. J. Lett. **244**, L1 (1981).
24. I. Bray, Mon. Not. R. Astron. Soc. **208**, 511 (1984).
25. R. R. Bourassa and R. Kantowski, Astrophys. J. **195**, 13 (1975).

Translated by A. Dambis

Astronomy Reports, Vol. 45, No. 12, 2001, pp. 935–941. Translated from Astronomicheskiĭ Zhurnal, Vol. 78, No. 12, 2001, pp. 1066–1072.

Spectral Characteristics of Faint Radio Sources of the *KHOLOD* Survey

N. S. Soboleva and A. V. Temirova

St. Petersburg Branch of the Special Astrophysical Observatory, Russian Academy of Sciences, Pulkovo, St. Petersburg, 196140 Russia

Received July 12, 2000

Abstract—Radio sources detected at 3.94 GHz in RATAN-600 observations made in 1980–1981 (the *KHOLOD* Survey) have been identified with objects from the NVSS catalog down to 5 mJy at 1.4 GHz, and their spectral indices have been estimated. Of the 1311 NVSS objects in the *KHOLOD* survey region, 836 are present in both catalogs. The average flux density of the common objects is 40 mJy, and the median flux density is 14 mJy. The average spectral indices of these objects for four flux-density intervals were calculated. The average spectral index grows with flux density. The fraction of objects with inverted spectra is 2–4%, and the average flux density of these sources is about 10 mJy. Optical identifications of the NVSS objects in the *KHOLOD* survey region have been carried out to $R = 20.5^m$ using the Palomar plates. About 20% of the radio sources are identified with optical objects in all the radio flux-density intervals.

1. INTRODUCTION

In the early 1990s, we published the RC catalog of radio sources at 3.94 GHz (7.6 cm) [1, 2], derived from data obtained during the *KHOLOD* ("*COLD*") experiment using the RATAN-600 radio telescope in 1980–1981 with the highest sensitivity available at that time [3, 4]. We fixed the absolute positions on the sky using the Texas UTRAO catalog of radio sources at 365 MHz (80 cm), kindly supplied by J. Douglas prior to publication. We collected all spectral information available at that time for the RC objects and published a spectral catalog [5, 6], which included about half the RC sources (529 objects).

The UTRAO catalog, which has a limiting flux density of 150–200 mJy, has enabled us to distinguish a subsample of the RC objects with ultrasteep spectra ($\alpha > 0.9$, $S \propto \nu^{-\alpha}$). This formed a basis for an international program involving three large telescopes—the VLA (NRAO, USA), RATAN-600, and the 6-meter optical telescope of the Special Astrophysical Observatory (Russia)—to search for very distant radio galaxies ($z > 1$) [7–12].

When the strip of sky for the *KHOLOD* Survey was surveyed at 1.4 GHz using the VLA with a spatial resolution close to the RATAN-600 resolution at 3.94 GHz, and when the qualitatively new NVSS catalog [13] (with a threshold sensitivity of 2.5 mJy) became available, the hope to obtain spectral information for the majority of the RC objects appeared. Furthermore, it became possible to improve the completeness of the RC catalog at low flux densities; i.e., to detect objects that had been missed earlier for various reasons.

Use of the improved NVSS positions, automatic plate measuring (a method developed in England [14]), and the internet enabled us to make POSS optical identifications of all the objects detected in the *KHOLOD* experiment.

Even basic information about the spectral indices of radio objects at various flux densities is useful for tests of models of evolution of radio sources (see, for example, [15]). The flux-density interval of 1–10 mJy, where objects with flatter spectra—AGN, FR I radio galaxies, BL Lac objects, star burst galaxies—begin to dominate [16] is of special interest. For some studies, even placing upper limits on the number of objects with inverted spectra is important. For instance, when investigating fluctuations of the cosmic microwave background, this enables more reliable extrapolation of the statistical properties of radio objects to the poorly studied region of wavelengths shorter than 1 cm, where objects with inverted spectra [17] may dominate.

The present work is devoted to a study of the spectral characteristics of faint radio sources and a search for populations of objects with flat and inverted spectra that could not be distinguished earlier.

1063-7729/01/4512-0935$21.00

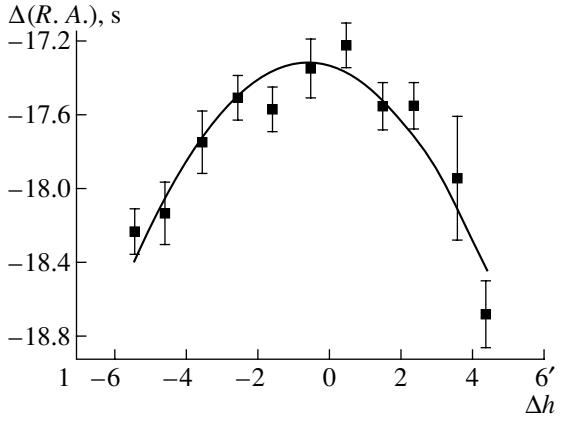

Fig. 1. Correction to the time of source transit through the radio telescope beam due to the feed offset from the focus along the focal line *versus* $\Delta h = \mathrm{dec}_{app}(\mathrm{SS\,433}) - \mathrm{dec}_{app}(\mathrm{NVSS})$.

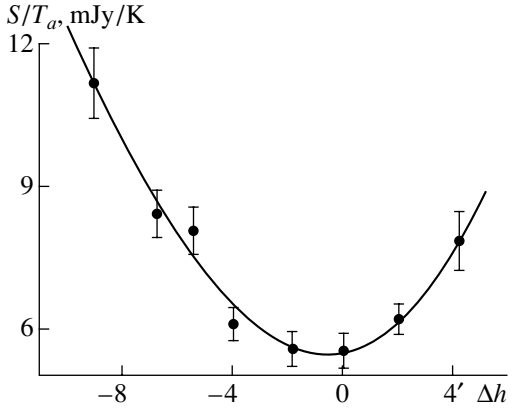

Fig. 2. Ratio of the flux density at 1.4 GHz to the antenna temperature as a function of Δh.

2. SPECTRAL PROPERTIES OF THE *KHOLOD* SURVEY OBJECTS

To compare the RC and NVSS objects, we selected right ascensions for which weather conditions permitted a somewhat-higher sensitivity to be achieved in the *KHOLOD* observations (4^{h}–21^{h}). (Note, however, that the sensitivity varied fairly widely from hour to hour in this interval.) This interval was divided into two approximately equal groups, the first including hours 4^{h}, 6^{h}, 7^{h}, 10^{h}, 13^{h}, 16^{h}, 17^{h}, 18^{h}–$18^{\mathrm{h}}40^{\mathrm{m}}$, and $19^{\mathrm{h}}20^{\mathrm{m}}$–$20^{\mathrm{h}}$, and the second including 5^{h}, 8^{h}, 9^{h}, 11^{h}, 12^{h}, 14^{h}, 15^{h}, and 21^{h}. Given the width of the declination strip considered (10′), the size of the area studied was 45 square degrees. Since, as a rule, the fluctuation sensitivity was better than 0.4 mK (1.6 mJy), which is much higher than in centimeter-wavelength surveys of such large areas of the sky, we could hope to obtain a statistically significant estimate of the fraction of flat-spectrum and inverted-spectrum NVSS objects as a function of flux density down to 5 mJy at 1.4 GHz.

We carried out all studies for the entire database, as well as for each group separately, and then compared the results for the two groups. The NVSS objects were selected according to two criteria:

(1) the radio source should lie within ±5′ (the vertical beam width at 3.94 GHz) of the central declination of the *KHOLOD* survey (the declination of SS 433); i.e., the apparent declination of an NVSS source at the *KHOLOD* survey epoch should differ by no more than ±5′ from the apparent declination of SS 433;

(2) the flux density of the radio source at 1.4 GHz S should be ≥ 5 mJy.

We consider that, with the sensitivity of our receiver at 3.94 GHz, we should have detected the overwhelming majority of flat- and inverted-spectrum NVSS objects with such flux densities. In the standard processing of the *KHOLOD* survey observations, the daily transit curves in both meridian and azimuth were divided into two subgroups containing from 12 to 17 records each. We studied the half-sums and half-differences of the transit curves for the subgroups for each right ascension, removed the background, and performed a Gaussian analysis of these curves [3].

For identification with the *KHOLOD* objects (detected via the Gaussian analysis), the positions of all NVSS objects in a sufficiently broad declination strip were recalculated to the apparent positions for the epochs of the *KHOLOD-1* (meridian observation, 1980) and *KHOLOD-2* (observation at azimuth 30°, 1981) surveys. We considered NVSS and *KHOLOD* objects to be identified with each other if, taking into account the feed offset from the focus along the focal line, they coincided within a fraction of a second of time on the transit curves in both meridian (*KHOLOD-1*) and azimuth (*KHOLOD-2*). In spite of the processing technique used, we cannot completely exclude the possibility of spurious identifications.

The corrections for the off-axis position of the feed (*KHOLOD-1*) as a function of $\Delta h = \mathrm{dec}_{app}(\mathrm{SS\,433}) - \mathrm{dec}_{app}(\mathrm{NVSS})$ were determined using the curve in Fig. 1, plotted for reference bright objects lying in a strip ±5′ from the position of SS 433.

Figure 2 shows the ratio of the flux density to the antenna temperature as a function of Δh (*KHOLOD-1*, meridian observation). For convenience in the calculations, instead of converting the antenna temperatures at 3.94 GHz to flux densities, we have inverted the problem and used this curve to recalculate the flux densities of the NVSS objects at 1.4 GHz to antenna temperatures. In this case, the spectral index is determined by the relationship

$$\alpha = \log(T_{a1.4\,\mathrm{GHz}}/T_{a3.94\,\mathrm{GHz}})/\log(\nu_{3.94\,\mathrm{GHz}}/\nu_{1.4\,\mathrm{GHz}}). \quad (1)$$

In total, in the $\pm 5'$ declination strip in the right ascension interval 4^{h}–21^{h}, 836 NVSS objects with flux densities $S \geq 5$ mJy were identified with *KHOLOD* sources. Figure 3 shows the distribution of these objects in flux density at 1.4 GHz. The average flux density is 40 mJy, with a median of 14 mJy (the bright object PKS 2128+04 has been excluded).

There were 475 NVSS objects with flux densities $S \geq 5$ mJy that were not identified with *KHOLOD* sources at 3.94 GHz. Below, we give the number of *KHOLOD* objects identified and not identified with NVSS objects in various flux-density intervals at 1.4 GHz.

Flux density, mJy	5–10	10–20	20–30	30–40	>40
Unidentified	341	106	17(3)	4(1)	7(3)
% of total	61	29	13	6	4
Identified	215	254	117	65	185
% of total	39	71	87	94	96
Total	556	360	134	69	192

Thus, of the total of 1311 NVSS objects that fell into the area of the sky we have studied at 7.6 cm, 836 sources (61%) could be detected in the transit curves of the RATAN-600 *KHOLOD* survey.

A careful analysis has shown that some of the unidentified NVSS objects with flux densities >20 mJy near the bright source Her A are not objects with ultrasteep spectra. They are spurious sources that have arisen from insufficient cleaning of the VLA maps around Her A. The figures in parentheses show the number of spurious NVSS objects in the preceding number of sources. Three objects with flux densities of 47, 61, and 139 mJy are probably variable (they are distinguished by the Gaussian analysis in the mean transit curves for 1981 but are absent from the mean transit curves for 1980).

The spectral indices of the sources identified with the NVSS objects were found using (1). Figure 4 presents the distributions of the spectral indices for the 1.4 GHz flux-density intervals $S = 5$–10, 10–20, 20–30, and $S \geq 30$ mJy. The average and median spectral indices in these flux-density intervals are given below.

Flux density, mJy	5–10	10–20	20–30	≥30
α (average)	0.16	0.30	0.54	0.66
α (median)	0.09	0.22	0.45	0.65

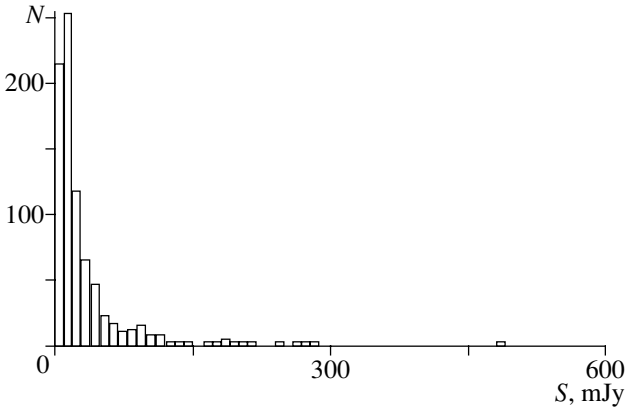

Fig. 3. Distribution of the 1.4-GHz flux densities of the NVSS objects identified with *KHOLOD* survey objects.

Even for objects with $S > 30$ mJy, for which the *KHOLOD* survey is expected to be 100% complete, the average spectral index turned out to be somewhat smaller than expected. The origin of this discrepancy requires a separate study. The above data testify that the average and median spectral indices grow with increasing flux density. To a considerable extent, this could be explained by a selection effect: the limited sensitivity of the 3.94 GHz receivers does not enable us to detect steep-spectrum objects at such flux-density levels. However, other origins are also possible.

Below, we give the number of objects with spectral indices $-0.3 < \alpha < 0.2$ in various flux-density intervals and the fraction of such sources in the total number of NVSS objects in our strip of sky.

Flux density, mJy	5–10	10–20	20–30	≥ 30
$-0.3 \leq \alpha \leq 0.2$	87	93	28	21
% of total	15	26	22	12

It follows that the fraction of flat-spectrum objects tends to decrease with increasing flux density. If we adopt the hypothesis that the fraction of flat-spectrum objects should be the same in each flux-density interval and be equal to 12% (as for $S \geq 30$ mJy, where the completeness of the survey is close to 100%), the χ^2 criterion indicates that the higher fraction of flat-spectrum sources at flux densities $S < 30$ mJy does not represent a chance fluctuation. Generally speaking, the decrease in the fraction of flat-spectrum objects at $S = 5$–10 mJy could be the result of incomplete detection of objects, even of those with flat spectral indices.

The dependence we have found is consistent with theoretical predictions: in evolutionary models, a growth of the fraction of flat-spectra objects is

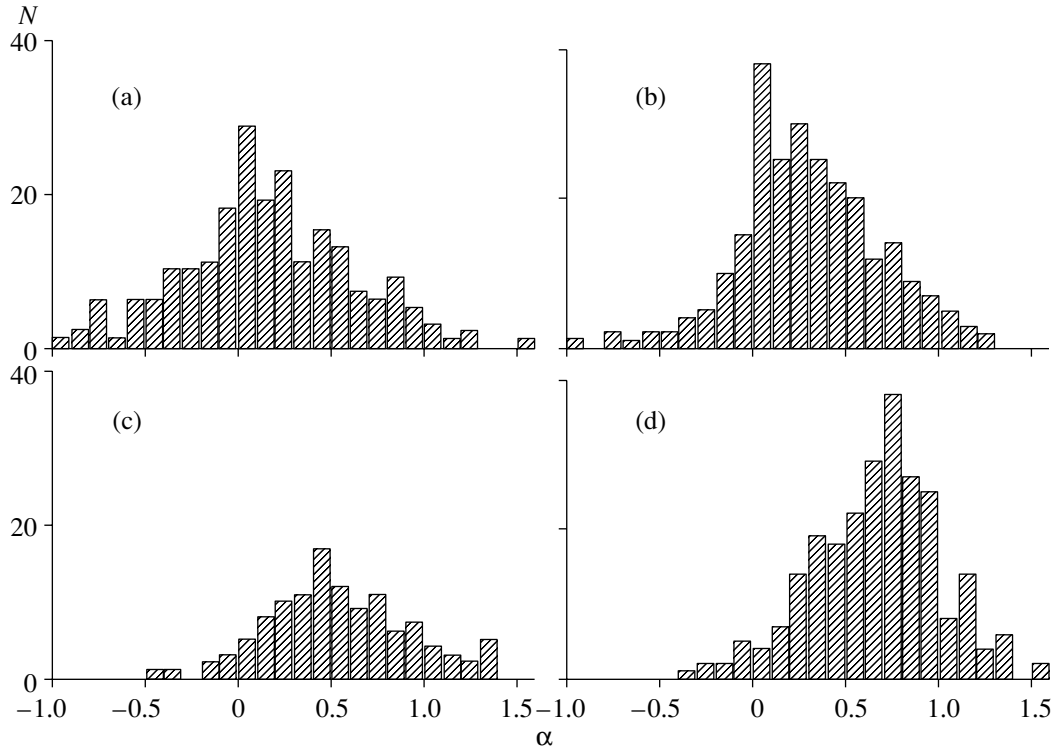

Fig. 4. Distribution of the spectral indices for objects common to the NVSS catalog and the *KHOLOD* Survey in the 1.4-GHz flux-density intervals (a) $S = 5$–10 mJy, (b) 10–20 mJy, (c) 20–30 mJy, and (d) $S > 30$ mJy. The horizontal axis shows the two-frequency spectral index α between 1.4 and 3.94 GHz.

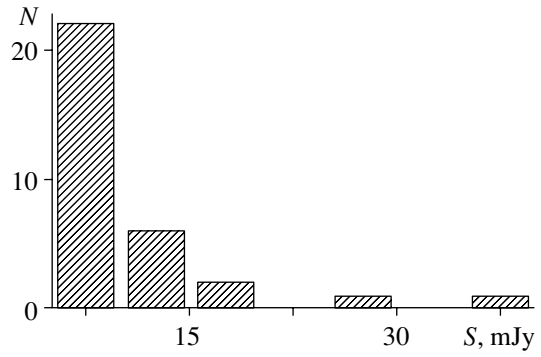

Fig. 5. Distribution of 1.4-GHz flux densities for inverted-spectrum objects common to the NVSS and RC catalogs.

expected in the transition from flux densities $S = 20$–100 mJy to $S = 1$–10 mJy [17].

There are 32 inverted-spectrum objects at the flux densities considered, which is about 4% of the total number of sources. We consider spectra to be inverted if $\alpha < -0.4$, taking into account the uncertainty in the spectral index; only 2% of the objects have $\alpha < -0.7$. The distribution of 1.4-GHz flux densities for inverted-spectrum objects is shown in Fig. 5. The average flux density of these sources is 9.9 mJy, with a median of 8 mJy.

Seventy-two of our sample sources are included in the UTRAO catalog. We have calculated spectral indices for these objects in the frequency intervals 0.365–1.4 and 1.4–3.94 GHz. The mean difference of the low- and high-frequency spectral indices is 0.15 ± 0.04, and the median is 0.145. One-hundred-seventeen of our objects are identified with sources from the catalog of Gregory *et al.* [18] at 4.85 GHz. For these objects, the mean difference of the spectral indices α(1.4–3.94 GHz) and α(1.4–4.85 GHz) is -0.031, with a median difference of 0.049, indicating fairly good agreement.

3. OPTICAL IDENTIFICATIONS

The radio luminosity of radio galaxies is a nonlinear function of their optical luminosity ($L_{radio} = K \times L_{opt}^{2.4}$ [19]) down to limiting values of 10^{47} erg/s. For the limiting radio luminosities of FR II radio sources, $L_{radio} = L_{opt}$. In particular, a powerful radio galaxy with $S = 100$ mJy at 21 cm is typically identified with a giant galaxy having $R = 22^m$—23^m, while a normal galaxy with the same radio flux density would be identified with an object 10^m—15^m brighter; i.e., with $R = 8^m$—13^m.

Results of optical identification

S (1.4 GHz), mJy	Number of sources	% of optically identified sources	R^m				Total
			19–20.5	18–19	17–18	<17	
5–15	377	21	32	19	12	16	79
15–25	165	18	15	8	3	4	30
25–35	85	27	12	6	2	3	23
35–45	46	26	4	2	3	3	12
45–55	36	11	3	0	0	1	4
55–65	18	22	1	2	0	1	4
>65	109	24	15	4	2	5	26

Objects with comparatively low radio luminosities are much fainter in the optical. Therefore, we did not expect to obtain POSS identifications with luminous radio galaxies for objects brighter than 100 mJy at 21 cm [7]. However, many objects with low relative radio luminosities (from quasars to normal galaxies) should be brighter than the POSS limit ($R = 19^m$—20^m).

We have obtained optical identifications for the *KHOLOD* sources in the R and B bands using the NVSS positions, the internet, and the English automatic plate measuring software [14], as well as digitized sky survey images [20]. Table 1 lists the flux-density interval, total number of sources in this interval, fraction of radio sources identified with optical objects to $R = 20\overset{m}{.}5$, and number of sources identified with objects with $19^m < R < 20\overset{m}{.}5$, $18^m < R < 19^m$, $17^m < R < 18^m$, and $R < 17^m$ for objects common to the NVSS catalog and *KHOLOD* survey.

This table shows that, in all flux-density intervals, the mean fraction of radio sources identified with optical objects is 21%. According to the χ^2 criterion, the small decrease in this fraction in the interval 45–55 mJy is insignificant, although it is consistent with expectations. On the average, the fractions of identifications are about 10% for $19^m < R < 20\overset{m}{.}5$, 5% for $18^m < R < 19^m$, 2% for $17^m < R < 18^m$, and 5% for $R < 17^m$.

Analysis of the fractions of optically identified objects as a function of their spectral indices shows that objects with relatively flat spectra ($\alpha < 0.5$) are twice as likely to be identified with POSS objects as steep-spectra objects with $\alpha > 0.5$ (19% and 10%, respectively). This result is not unexpected, and is associated with the lower relative radio luminosity of such objects: at the same flux density level, they are hosted by more luminous galaxies. Among the identified objects, the fractions of galaxies and quasars are approximately the same.

We have also obtained optical identifications for NVSS objects located in the same strip of sky ($\pm 5'$ from the central transit section for SS 433) that were not detected in the *KHOLOD* experiment (RC catalog). The results of identifications of these NVSS objects are as follows.

S(1.4 GHz), mJy	% of optically identified sources
5–15	18.5
15–25	33
>25	0

We can see that the fraction of optically identified NVSS objects with low flux densities ($5 \le S < 15$ mJy) that are absent from the *KHOLOD* survey is close to the fraction of NVSS sources detected in the survey. As expected, a considerable fraction of NVSS objects with $15 \le S \le 25$ mJy at $\nu = 1.4$ GHz are identified with optically bright galaxies with $R < 19^m$. The absence of these radio sources from the *KHOLOD* survey indicates that their spectral indices are $\alpha > 0.5$.

4. DISCUSSION

In 1998, Bursov [21] published a statistical analysis of the spectral properties of NVSS sources located in the strip of sky surveyed in the *KHOLOD* experiment. He concluded that the spectral indices of the sources did not depend statistically on the flux density at $\nu = 1.4$ GHz down to 2.5 mJy and was equal to 0.85. The analysis of [21] was based on observations of the later *KHOLOD* survey in 1993. The NVSS objects were sorted according to their flux densities, and the average flux density in a given interval was adopted. Sections of the 3.94-GHz transit curves where NVSS objects were expected were then averaged, and the spectral index of this averaged object

determined. This method is completely free from the effect of saturation, and even early tests demonstrated the possibility of studying submillijansky objects by cross-correlating large catalogs with the *KHOLOD* survey database.

The probability of identifying NVSS objects with *KHOLOD* sources decreases with increasing spectral index of the object. Our lists are sufficiently complete for objects with flat and inverted spectra, but not for sources with steep spectra ($\alpha > 0.7$).

The results of [21] and the current paper can be reconciled if we assume that the dispersion in the spectral indices grows with decreasing flux density at 1.4 GHz. We also cannot exclude methodical errors, namely:

(1) there could be a large number of spurious NVSS objects at low flux densities (although there are probably some spurious faint objects in the NVSS catalog, this explanation seems to us improbable);

(2) the declination strip adopted by Bursov [21] for the averaging was too broad, $\pm 20'$; correction for the beam shape in declination (the beam halfwidth is $10'$) could cause difficulties and systematic effects.

We intend to investigate these possibilities and to perform a statistical estimate of the average spectral index for objects with flux densities of 5–20 mJy directly in the area of sky in question.

We believe that virtually all objects with flat and inverted spectra in this area of sky have been detected down to $S > 10$ mJy at 21 cm. Only 2–4% of objects have inverted spectra, and their average flux density is about 10 mJy. Even knowledge of the average spectral index for objects with $S > 5$ mJy would enable estimation of the fraction of objects with ultrasteep spectra.

At the same time, we envisage using the entire *KHOLOD* database for very deep (down to the saturation level, at less than 1 mJy) individual identification of *KHOLOD* objects with sources in the NVSS catalog, whose position accuracy is, as a rule, sufficient for optical identification. We also plan to classify the optically identified objects according to their morphology and colors and to distinguish the populations of quasars, BL Lac objects, active galactic nuclei, etc..

Finally, we note that studies at the millijansky level supplement both very deep observations of small areas of sky (such as the VLA survey [22, 23]) and complete low-sensitivity sky surveys in an important way. Here, the main interest is in finding populations of radio sources fainter than the objects included in GB-type catalogs, but with a low surface density (less than one per solid angle of the VLA survey areas of 1–10 square arcmin).

ACKNOWLEDGMENTS

This work was supported by the Russian Foundation for Basic Research (project no. 99-02-17114), the State Program in Astronomy (grant 1.2.2.4), INTAS (grant 97-1192), and the Integration Program (grant 508). The authors are grateful to Yu.N. Parijskij for his interest in this work, to A.V. Savastene for help with the preparation of the manuscript, and to N.E. Gol'neva for participation in the optical identification of the objects.

REFERENCES

1. Yu. N. Parijskij, N. N. Bursov, N. M. Lipovka, *et al.*, Astron. Astrophys., Suppl. Ser. **87**, 1 (1991).
2. Yu. N. Parijskij, N. N. Bursov, N. M. Lipovka, *et al.*, Astron. Astrophys., Suppl. Ser. **96**, 583 (1992).
3. Yu. N. Parijskij and D. V. Korolkov, Astrophys. Space Rev. **5**, 1 (1986).
4. A. B. Berlin, E. V. Bulaenko, V. Ya. Gol'nev, *et al.*, Pis'ma Astron. Zh. **7**, 290 (1981) [Sov. Astron. Lett. **7**, 161 (1981)].
5. N. N. Bursov, A. V. Chepurnov, N. M. Lipovka, *et al.*, Astron. Astrophys., Suppl. Ser. **101**, 447 (1993).
6. N. N. Bursov, N. M. Lipovka, N. S. Soboleva, *et al.*, Bull. Spec. Astrophys. Obs. **42**, 5 (1996).
7. Yu. N. Parijskij, W. M. Goss, A. I. Kopylov, *et al.*, Bull. Spec. Astrophys. Obs. **40**, 5 (1996).
8. A. I. Kopylov, V. M. Goss, Yu. N. Parijskij, *et al.*, Astron. Zh. **72**, 437 (1995); [Astron. Rep. **39**, 383 (1995)]; Astron. Zh. **72**, 613 (1995) [Astron. Rep. **39**, 543 (1995)].
9. Yu. N. Parijskij, V. M. Goss, A. I. Kopylov, *et al.*, Astron. Zh. **75**, 483 (1998) [Astron. Rep. **42**, 425 (1998)].
10. S. N. Dodonov, Yu. N. Parijskij, V. M. Goss, *et al.*, Astron. Zh. **76**, 323 (1999) [Astron. Rep. **43**, 275 (1999)].
11. T. Pursimo, K. Nilson, P. Teerikorpi, *et al.*, Astron. Astrophys., Suppl. Ser. **134**, 505 (1999).
12. Yu. N. Parijskij, W. M. Goss, A. I. Kopylov, *et al.*, Astron. Astrophys. Trans. **19**, 297 (2000).
13. J. J. Condon, W. D. Cotton, E. W. Greisen, *et al.*, Astron. J. **115**, 1693 (1998); www.cv.nrao.edu/NVSS/NVSS.html.
14. M. Irwin, S. Maddox, and R. McMahon, Spectrum, No. 2, 14 (1994); www.ast.cam.ac.uk/mike/apmcat/.
15. C. A. Jackson and J. V. Wall, Mon. Not. R. Astron. Soc. **304**, 160 (1999).
16. L. Toffolatti, F. Argueso Gomez, G. de Zotti, *et al.*, astro-ph/9 711 085 (1997).

17. A. Franceschini, L. Toffolatti, L. Danese, and G. De Zotti, Astrophys. J. **344**, 35 (1989).
18. P. C. Gregory, W. K. Scott, K. Douglas, and J. J. Condon, Astrophys. J., Suppl. Ser. **103**, 427 (1996).
19. S. Iskudaryan and Yu. N. Parijskij, Izv. Glavn. Astron. Obs. Akad. Nauk SSSR **24** (182), 175 (1967).
20. Digitized Sky Surveys cadcwww.dao.nrc.ca/cadcbin/getdss/.
21. N. N. Bursov, Preprint No. 127 (St. Petersburg State Univ., St. Petersburg, 1998).
22. E. B. Fomalont, in *Extragalactic Radio Sources (IAU Symposium 175),* Ed. by R. Ekers, C. Fanti, and L. Padrielli (Kluwer, Boston, 1996), p. 555.
23. R. A. Windhorst, E. B. Fomalont, R. B. Partridge, and J. D. Lowenthal, Astrophys. J. **405**, 498 (1993).

Translated by G. Rudnitskiĭ

Astronomy Reports, Vol. 45, No. 12, 2001, pp. 942–948. Translated from Astronomicheskiĭ Zhurnal, Vol. 78, No. 12, 2001, pp. 1073–1080.

A Magnetized Disk around an O Star in W75N. A VLBI Map of the OH Maser

V. I. Slysh[1], I. E. Val'tts[1], and V. Migenes[2]

[1] *Astro Space Center, Lebedev Physical Institute, Russian Academy of Sciences, Profsoyuznaya ul. 84/32, Moscow 117810, Russia*
[2] *University of Guanajuato, Department of Astronomy, Apdo Postal 144, Guanajuato, GTO, CP36000, Mexico*

Received April 15, 2001

Abstract—W75N is a star-forming region containing ultracompact H II regions as well as OH, H_2O, and methanol masers. The VLBA maps obtained show that the masers are located in a thin disk rotating around an O star, which is the exciting star for the ultracompact H II region VLA1. A separate group of maser spots is associated with the ultracompact H II region VLA2. The radial velocity of the maser spots varies across the disk from 3.7 to 10.9 km/s. The disk diameter is 4000 AU. The maser spots revolve in Keplerian orbits around the O9 star. © *2001 MAIK "Nauka/Interperiodica"*.

1. INTRODUCTION

OH masers were the first among a new class of astronomical phenomena characterized by intense narrow-band polarized variable emission at frequencies of molecular transitions. It was found that the sources of this emission are compact clumps of neutral gas at the peripheries of H II regions created by recently formed massive O and B stars. High-angular-resolution studies of the masers have shown that they consist of clusters of bright compact maser spots distributed over an area of several arcseconds. The spots have sizes from 2 to 70 mas; in some masers, they are even smaller, below the resolution limits of modern VLBI systems. The task of high-angular-resolution studies of OH masers is to determine the relative arrangement of the maser spots and their intensities, as well as to map the spots themselves. Determination of the sizes and shapes of the maser spots is important for improving our understanding of the mechanisms for the maser emission and the limits of the brightness temperatures to which they give rise. The shapes of maser spots can also point toward the physical phenomena responsible for the generation of the maser emission.

Several probable sites of maser emission have been proposed: ionization fronts at the boundaries of H II regions, interfaces between molecular outflows and surrounding molecular clouds, and protoplanetary accretion disks around young stars. The sizes and shapes of the maser spots are important characteristics of the maser emission, provided that they are intrinsic to the source and are not due to the effects of propagation through the interstellar medium, such as interstellar scattering.

W75N is a maser located in the Cygnus X complex. In the VLBI observations of Haschick *et al.* [1], the maser consisted of nine maser spots located in a 1.″5 area elongated in position angle 20°. The maser coincides with an ultracompact H II region. Haschick *et al.* [1] proposed a model in which the masers were located in a disk rotating around a protostellar system formed from the remains of the material from which the stars had formed. The higher-angular-resolution MERLIN observations of Baart *et al.* [2] are not consistent with a rotating-disk model. Baart *et al.* proposed a model in which the masers are located in a compressed region between the shock front and ionization front of the compact H II region. Baart *et al.* [2] mapped the OH maser in both circular polarizations and found linearly polarized spots and spots with Zeeman components.

Torrelles *et al.* [3] mapped the W75N region in the H_2O maser line and in the continuum. Based on these data, they proposed a model in which the ultracompact H II region is a biconical ionized-gas jet aligned with the large-scale molecular outflow in this region and the H_2O (as well as OH) masers are located along the jet axis and trace the molecular outflow near its origin.

Previous observations of the OH maser in W75N had insufficient angular resolution to distinguish between these models; furthermore, there was no com-

1063-7729/01/4512-0942$21.00

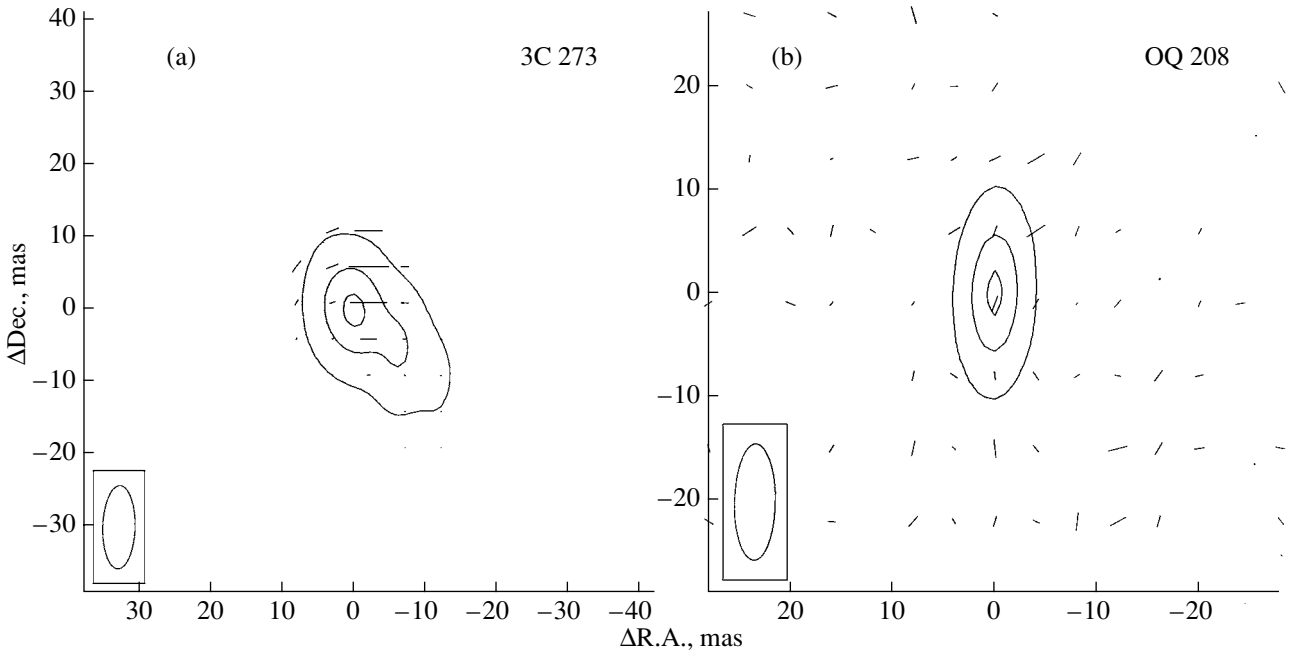

Fig. 1. Maps of the continuum calibration sources. (a) Total-intensity contours of 3C 273 at $I = 0.9, 4.5$, and 8.2 Jy/beam with vectors indicating the linearly polarized intensity; the maximum vector length is 0.125 Jy/beam, $m_{\rm L} = 0.8\%$, and $m_{\rm C} = 1.8\%$. (b) Total-intensity contours of OQ 208 at $I = 0.085$, 0.45, and 0.77 Jy/beam with vectors indicating the linearly polarized intensity; 1 mas = 0.0004 Jy/beam, $m_{\rm L} \leq 0.8\%$, and $m_{\rm C} = 1.8\%$.

plete polarization analysis. In this work, we present the results of VLBA observations of the OH maser W75N with much higher angular and frequency resolution in all four OH lines (1612, 1665, 1667, and 1720 MHz).

2. OBSERVATIONS AND DATA REDUCTION

The observations were obtained on July 1, 1998, as a part of a survey of compact OH masers carried out as preparation for possible future observations with a ground–space interferometer. The observations were carried out on the VLBA in snapshot mode, with 5 min of observing time scheduled for each source. The synthesized beam of the array at 1665/1667 MHz was 12×4 mas in position angle $-5°$. The observations were performed in all four OH lines in a 125-kHz (25 km/s) band divided into 128 channels at each of the four OH frequencies, providing a spectral resolution of 0.176 km/s. Each of the ten VLBA radio telescopes had two receivers, independently measuring right (R) and left (L) circular polarizations.

The signals were processed on the VLBA correlator of the National Radio Astronomy Observatory in Socorro in complete cross-correlation mode, providing correlated RR, LL, RL, and LR spectra for each pair of antennas. These spectra can be used to derive the Stokes parameters using the standard method (RR and LL refer to the correlation of signals for receivers of the same circular polarization at the two antennas in a baseline, while RL and LR refer to the correlation of signals for receivers of opposite circular polarizations):

$$I = \frac{1}{2}(\mathrm{RR} + \mathrm{LL}), \quad V = \frac{1}{2}(\mathrm{RR} - \mathrm{LL}), \quad (1)$$
$$Q = \frac{1}{2}(\mathrm{RL} + \mathrm{LR}), \quad U = \frac{i}{2}(\mathrm{LR} - \mathrm{RL}).$$

The amplitudes were calibrated using the receiver noise temperatures and antenna gains as functions of elevation supplied by the VLBA data-analysis group. The continuum sources 3C 273 and OQ 208 were used to calibrate the spectral passband and polarization; however, we did not calibrate the absolute value of the linear-polarization position angles.

Figure 1 shows contour images of 3C 273 and OQ 208 with superposed vectors displaying the linearly polarized intensity. The peak vector in Fig. 1a corresponds to a linear polarization of $m_{\rm L} = 1.4\%$; the circular polarization measured for 3C 273 is $m_{\rm C} = 1.8\%$. The linear-polarization position angle was not calibrated, as noted above. For OQ 208, the linear-polarization vectors correspond to $m_{\rm L} \leq 0.1\%$, and are randomly distributed over the entire field; the circular polarization is the same as that for 3C 273, $m_{\rm C} = 1.8\%$. OQ 208 is known to be unpolarized [4],

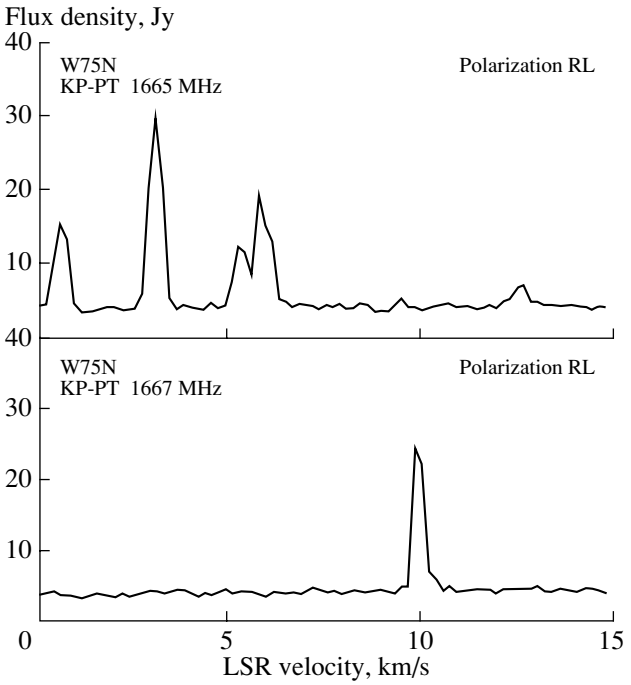

Fig. 2. Cross-polarized (RL) spectra of W75N on the Kitt Peak–Pie Town baseline at the OH line frequencies 1665 MHz (top) and 1667 MHz (bottom).

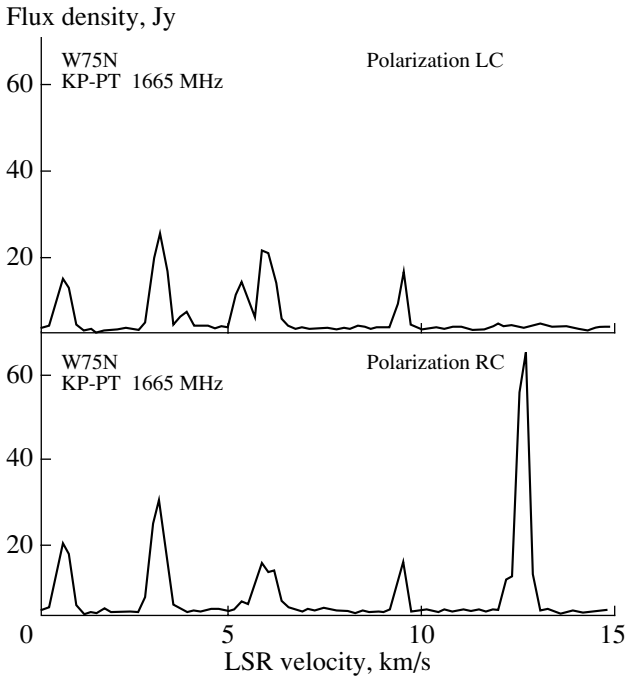

Fig. 3. Cross-correlation spectrum of the circularly polarized emission of W75N on the Kitt Peak–Pie Town baseline at the OH line frequency 1665 MHz. Top: left-circular polarization (LC), bottom: right-circular polarization (RC).

while the linear polarization of the nucleus of 3C 273 at 18 cm is $m_{\rm L} = 1.8$—2.15% [5], similar to our value in Fig. 1a if we take into account the crude character of measurements in snapshot mode.

In any case, values of linear polarization smaller than 1% should not be considered trustworthy. The circular polarizations of both calibration sources are known to be zero, and the agreement in our measurements for the two sources implies an unaccounted-for instrumental polarization, in the sense that the intensity of the right-circular polarization systematically exceeds that of the left-circular polarization. We have corrected our data for the OH maser for this instrumental error by subtracting 1.8% from all values of the degree of circular polarization $m_{\rm C}$. These corrections are small in comparison with the degrees of circular polarization of individual spectral features in the OH lines.

Calibration was performed relative to a reference spectral feature (using self-calibration) using the FRING procedure in the AIPS package. We chose the reference feature so that the receiver channels could be calibrated in both right- and left-circular polarizations. This is possible if the spectral feature is sufficiently strong in both polarizations. To satisfy this requirement, this feature should be either unpolarized or linearly polarized. Unpolarized spectral features are rare in OH masers; therefore, we searched for a linearly polarized feature. Figure 2a shows the RL cross-polarization spectrum for the Kitt Peak–Pie Town baseline. The features in this cross-polarization spectrum (i.e., the spectrum for the correlation between signals of opposite circular polarizations at the two antennas in the baseline) reveal the presence of linear polarization. We found seven linearly polarized features in the spectrum that could be taken as reference features. We chose a feature at a velocity of 5.65 km/s, which had the maximum correlated flux on the longest baseline, Mauna Kea–Saint Croix, and could therefore be used to calibrate all antennas of the array.

Global fringe fitting was performed for the data for the reference feature. We corrected the position of the phase center adopted during correlation using the absolute coordinates of the reference feature, which we derived from fringe-rate mapping. It is known that the spatial separations of various spectral features in W75N are rather wide compared to the map size, and we accordingly performed the mapping in two stages. We first found an approximate position of each spectral feature relative to the reference feature using fringe-rate mapping, and then constructed maps of spectral features centered on these intermediate positions. We obtained the relative coordinates and

angular sizes by fitting two-dimensional Gaussians to these maps, restored with the antenna beams. Some maps of the spectral features were obtained in all Stokes parameters: I, Q, U, and V. The first three Stokes parameters yielded maps of the total-intensity I and linear polarization.

We considered the 1667-MHz data to be independent of the 1665-MHz data and calibrated them separately, using the feature at 9.8 km/s as the reference. The absolute position of the reference feature at 1667 MHz was determined using the fringe-rate method independent of the 1665-MHz measurements, with a lower accuracy than that achieved in the relative position measurements.

3. RESULTS

3.1. The Spectrum

The cross-correlation circularly-polarized spectra at 1665 and 1667 MHz are shown in Fig. 3. A comparison with the spectra obtained in 1975 by Davies *et al.* [6] reveals a number of differences. The strongest feature, which is right-circularly polarized and at a velocity of about 12 km/s, has the same flux, but its radial velocity has shifted from 12.0 to 12.45 km/s. The nearby weaker feature at 13 km/s in 1975 is not present in our spectra. Two new right-circularly polarized features have appeared at velocities of 0.65 and 3.0 km/s. New features at 9.4 km/s and 0.65 km/s have appeared in the left-circular polarization spectrum. The 1667-MHz spectrum has fewer spectral features, and they are concentrated in a narrower velocity interval. The total-intensity cross-correlation spectra at 1665 and 1667 MHz are presented in Fig. 4. There is no clear correspondence between spectral features of the two main OH lines. We found no emission features in the satellite lines at 1612 and 1720 MHz.

3.2. Absolute Positions

The absolute coordinates of the reference feature at 1665 MHz are given in the footnote to the table. They are a factor of three more precise than those obtained earlier by Haschick *et al.* [1]; however, the two measurements agree within the errors. The absolute coordinates of the strongest 1667-MHz feature, which has a velocity of 9.8 km/s, were measured independently. We found that the coordinates of the 1667 MHz feature differ from those of the reference feature at 1665 MHz by 175 ± 69 mas in right ascension and -661 ± 42 mas in declination.

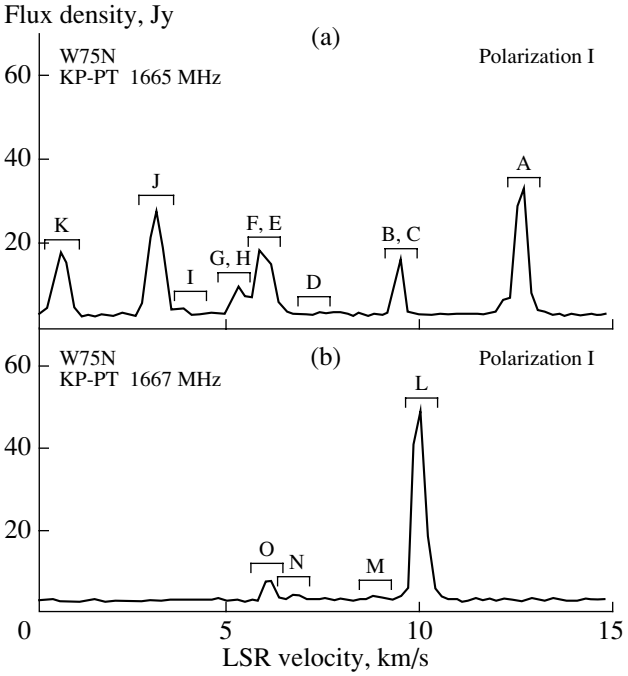

Fig. 4. Total intensity I of the cross-correlation power spectrum of W75N at frequencies of (a) 1665 MHz and (b) 1667 MHz. The letters A to O denote spectral features we have mapped. Their polarization parameters and the parameters of the maps are listed in the table.

3.3. Distribution of the Maser Spots

We detected 11 maser spots at 1665 MHz and four at 1667 MHz. The table lists the parameters of the maser spots derived from the spectra and polarization maps: radial velocity, Stokes parameters (I, V, Q, U), degree of circular (m_C) and linear (m_L) polarization in per cent, position angle for linear polarization, position offsets in right ascension and declination from the position of the reference feature, restored angular sizes of the fitted elliptical Gaussians, and their position angles.

The error in the relative positions is less than 1 mas. The position error of spot L at 1667 MHz is much larger because it was determined using the fringe rate method, but the position errors of other spots at 1667 MHz with respect to spot L are smaller than 1 mas. Figure 5 shows the positions of the maser spots and of the ultracompact H II regions VLA1 and VLA2, taken from Torrelles *et al.* [3]. Most spots are arranged along an almost straight line (the length is 1.″6, or 3200 AU) at some distance from VLA1. The spots at 1667 MHz do not coincide with any spot at 1665 MHz, although they are located in the same region.

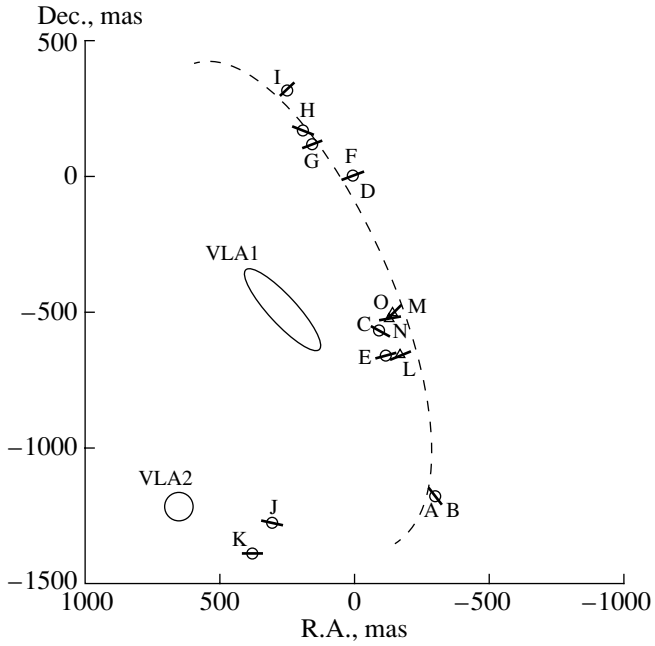

Fig. 5. VLBA map of the OH maser spots showing features at 1665-MHz (circles) and 1667 MHz (triangles). The notation is the same as in the table. The vectors show the magnetic field direction. The ellipse and circle labeled VLA1 and VLA2 show the positions and sizes of the ultracompact H II regions from Torrelles *et al.* [3]. The dashed curve shows part of a possible disk centered on VLA1, inclined by 12° to the line of sight.

The line-of-sight velocity varies from 3.8 to 10.9 km/s (this is the average velocity for features A and B, which are cospatially formed as a Zeeman pair) along a north–south line. The two individual spots J and K are located near the other ultracompact H II region VLA2. This map is very similar to the MERLIN map of Baart *et al.* [2]. All 1665-MHz maser spots on our map can be identified on the map of [2] except for spot K at 0.65 km/s. However, there are some weak spots on the MERLIN map that are absent from our map. Our 1667 MHz map is the first published and cannot be compared with earlier maps. There is also a good agreement with the VLBI map of Haschick *et al.* [1]. The only significant difference between our map and the earlier maps of Baart *et al.* [2] and Haschick *et al.* [1] is that the spot at 12.15 km/s is displaced by 140 mas. Note that the radial velocity of this feature has also changed by 0.45 km/s. We cannot be sure that feature A is identical to the 12-km/s feature on earlier maps. It is possible that the earlier 12-km/s feature has disappeared and that A is a new feature that flared near the spot having a velocity of 12 km/s. On the other hand, the identification of feature A with the 12 km/s feature observed earlier is supported by the fact that it dominates and has approximately the same flux in both spectra.

3.4. Sizes and Brightness Temperatures of the Maser Spots

All the maser spots are partially resolved. We can see from the table that the largest are spot K (20 mas × 12 mas) and spot N (14 mas × 3 mas), which may consist of several smaller spots. Other spots can be approximated by Gaussians with major axes from 4.4 to 10.7 mas and minor axes from 0.7 to 4.6 mas. Since the beam width is 12 mas × 4 mas, a size as small as 0.7 mas should be considered only a formally fitted solution. The true minor axes could be much smaller than the sizes indicated above, which are essentially upper limits. The brightness temperature of one of the brightest spots at 1665 MHz (the reference feature) is 1.6×10^{12} K for an integrated flux of 18.1 Jy. Spot L with an integrated flux 31.9 Jy, which is the brightest spot at 1667 MHz, has a brightness temperature of 1.9×10^{12} K. These values should be considered lower limits, since most spots are probably not resolved along their minor axes.

All the spots in the maps are elongated, with axial ratios of three or more. It is interesting to consider the orientation of their major axes. The table shows that most spots are aligned in approximately the same direction, with a position angle for the major axis of about 90°. This can be seen in the histogram in

Maser spots in W75N

Spot	V_{LSR}, km/s	I, Jy/beam	V, Jy/beam	Q, Jy/beam	U, Jy/beam	m_C	m_L	χ	RA, mas	Dec., mas	Size, mas	θ
1665 MHz												
A	12.45	16.88	16.24	<0.04	−1.56	94.4	9.3	−45.0	−301.7	−1176.7	5.9 × 1.4	95°
B	9.38	3.92	−3.24	−0.17	−0.68	−84.4	17.9	−52.2	−301.1	−1177.3	5.5 × 4.6	86
C	9.35	3.27	3.50	0.11	−0.19	105.3	6.9	−29.8	−98.2	−573.5	5.6 × 4.1	61
D	7.35	0.61	0.62	<0.02	<0.02	101.2	<5.0	...	−1.0	−32.7	4.4 × 1.1	83
E	6.00	5.76	<0.02	4.71	2.69	<0.3	94.2	14.9	−122.7	−663.6	5.9 × 2.2	92
F*	5.65	10.16	−0.81	6.93	7.12	−9.8	97.8	22.9	0.0	0.0	5.4 × 1.2	96
G	5.29	3.30	−0.78	2.37	1.87	−25.4	91.4	19.2	155.5	114.2	7.6 × 2.9	59
H	5.11	2.86	−2.24	1.41	−1.45	−80.0	70.7	−22.9	186.9	167.1	5.1 × 2.5	94
I	3.70	1.18	−1.28	<0.02	0.13	−110.8	10.8	40.6	249.0	317.9	6.5 × 2.9	77
J	3.00	8.16	0.79	7.61	−3.05	7.9	100.5	−10.9	299.8	−1275.8	10.7 × 2.4	114
K	0.65	0.83	0.22	0.78	<0.009	24.2	93.7	0.0	376.5	−1385.3	19.7 × 11.9	142
F1	−0.65	0.040	<0.003	0.035	0.023	<10	87	20.5	0.14	0.47	6.5 × 0.7	74
1667 MHz												
L	9.80	21.33	−4.46	6.01	6.54	−22.7	41.6	23.7	−175.4	−661.2	6.2 × 1.9	91
M	8.65	1.49	1.26	<0.01	0.14	82.5	9.4	45.0	−149.9	−506.1	5.4 × 0.7	90
N	6.55	0.55	−0.61	0.045	<0.01	−112.8	8.5	8.0	−136.2	−526.8	14.2 × 3.2	176
O	5.95	2.46	−2.23	<0.01	0.17	−92.5	7.1	45.0	−149.7	−505.0	7.4 × 2.5	113

* Position of the reference feature: $\alpha_{2000} = 20^h38^m36\overset{s}{.}414 \pm 0\overset{s}{.}003$, $\delta_{2000} = 42°37'35\overset{''}{.}44 \pm 0\overset{''}{.}03$.

Fig. 6a, which presents the distribution of the major-axis position angles. The average position angle is 93°, with a dispersion of 28°. This orientation of the ellipses could be an intrinsic property of the masers if the maser spots are formed in a common structure, such as a disk, as proposed by Haschick *et al.* [1]. The position angle of this proposed disk is 20°; in this case, the major axis of the maser spots is roughly perpendicular to the disk. If the maser-spot sizes are not their true sizes and the above values are affected by interstellar scattering, the spot orientations could be a consequence of anisotropy of this scattering.

4. MODEL FOR THE MASER EMISSION

Physical parameters of the maser spots can be derived from maser models, which require gas densities of $n_{H_2} = 10^7$ cm^{-3}, kinetic temperatures of 100 K, dust temperatures of 150 K, and OH abundances of 10^{-5} [7]. Such parameters can provide inversion of the 1665-MHz OH transition in models with overlapping far-infrared lines and a velocity gradient of about 0.025 km/s per AU [7]. For a magnetic field intensity of about 10 mG, the model of Gray and Field [7] provides the presence of 100% elliptically polarized σ components and the complete suppression of π components, quite consistent with our results for W75N. Maser-spot sizes of 10 AU and molecular hydrogen densities of 10^7 cm^{-3} correspond to maser-spot masses of about $2 \times 10^{-7} M_\odot$, less than the Earth's mass.

If the maser spots are separate physical objects, such as dense gas clumps, surrounded by a lower-density medium, they must be confined by external pressure. A gas clump with a density of 10^7 cm^{-3} and temperature of 100 K can be in equilibrium with gas with a density of 10^5 cm^{-3} and temperature of 10^4 K. A different model was proposed for class-II methanol masers by Slysh *et al.* [8]. This model proposes that the maser spots are in the extended gas envelopes of solid ice planets revolving around O or B stars outside their H II regions. In this case, OH molecules formed by the dissociation of water, as well as methanol molecules, are continuously supplied to the envelope due to the evaporation of ice from the

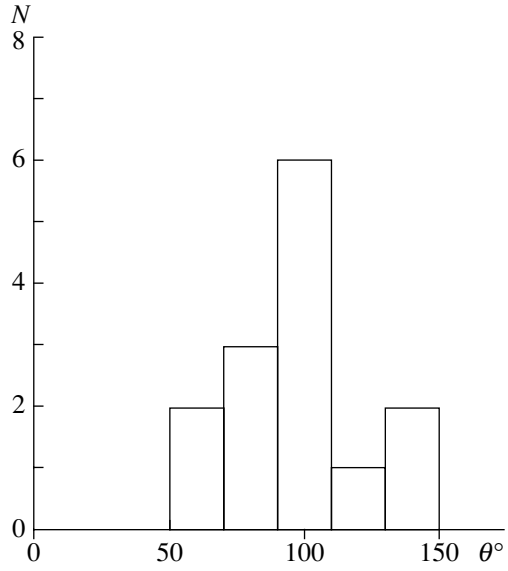

Fig. 6. Distribution of position angles θ of the major axes for the maser spot sizes in W75N; $\theta = 93° \pm 28°$.

planet's surface. In W75N, the compact H II region VLA1 indicates the presence of a central star with a luminosity of $1.4 \times 10^5 L_\odot$ [9], which corresponds to an O9 main-sequence star with a mass of $20M_\odot$. The largest distance from VLA1 to the maser spot is about 1000 mas, or 2000 AU. At such a distance, the velocity of a body in orbit around a $20M_\odot$ star is 3 km/s, comparable to the observed range of the maser spots' velocities in W75N.

5. CONCLUSIONS

(1) Most of the maser spots are elongated in approximately the same direction; the position angle of the major axis is about 90°. This elongation may be an intrinsic property of the maser.

(2) The OH masers are located in a thin disk rotating around a star, which is also the exciting star for the ultracompact H II region. The disk diameter is 4000 AU.

(3) The maser spots are revolving in Keplerian orbits around an O9 star.

(4) Another two maser spots are associated with the ultracompact H II region VLA2.

ACKNOWLEDGMENTS

VIS and IEV gratefully acknowledge partial support from the Russian Foundation for Basic Research (project no. 01-02-16902) and INTAS (grant 97-11451).

REFERENCES

1. A. D. Haschick, M. J. Reid, B. F. Burke, *et al.,* Astrophys. J. **244**, 76 (1981).
2. E. E. Baart, R. J. Cohen, R. D. Davies, *et al.,* Mon. Not. R. Astron. Soc. **219**, 145 (1986).
3. J. M. Torrelles, J. F. Gomez, L. F. Rodriguez, *et al.,* Astrophys. J. **489**, 744 (1997).
4. C. Stanghellini, D. Dallacasa, C. P. O'Dea, *et al.,* Astron. Soc. Pac. Conf. Ser. **164**, 177 (1998).
5. R. G. Conway, S. T. Garrington, R. A. Perley, and J. A. Biretta, Astron. Astrophys. **267**, 347 (1993).
6. R. D. Davies, R. S. Booth, and J.-N. Perbet, Mon. Not. R. Astron. Soc. **181**, 83 (1977).
7. M. D. Gray and D. Field, Astron. Astrophys. **298**, 243 (1995).
8. V. I. Slysh, I. E. Val'tts, S. V. Kalenskiĭ, and G. M. Larionov, Astron. Zh. **76**, 751 (1999) [Astron. Rep. **43**, 657 (1999)].
9. T. J. T. Moore, G. M. Mountain, and T. Yamashita, Mon. Not. R. Astron. Soc. **248**, 79 (1991).

Translated by G. Rudnitskiĭ

Astronomy Reports, Vol. 45, No. 12, 2001, pp. 949–959. Translated from Astronomicheskiĭ Zhurnal, Vol. 78, No. 12, 2001, pp. 1081–1091.

Twenty-Year-Long Monitoring of the H_2O Maser S269

E. E. Lekht[1,*], M. I. Pashchenko[2], and I. I. Berulis[3]

[1] *Instituto Nacional de Astrofísica, Óptica y Electrónica, Luis Enrique Erro No. 1, Apdo Postal 51 y 216, 72840 Tonantzintla, Puebla, México*
[2] *Sternberg Astronomical Institute, Universitetskiĭ pr. 13, Moscow, 119899 Russia*
[3] *Pushchino Radio Astronomy Observatory, Astro Space Center, Lebedev Physical Institute, Russian Academy of Sciences, Pushchino, 142292 Russia*
Received March 7, 2001

Abstract—Results of observations of the H_2O maser in S269 carried out from October 1980 to February 2001 on the 22-m telescope (RT-22) of the Pushchino Radio Astronomy Observatory are presented. During the monitoring of S269, variability of the integrated flux of the maser emission with a cyclic character and an average period of 5.7 years was observed. This may be connected with cyclic activity of the central star during its formation. Emission at radial velocities of 4–7 km/s was detected. Thus, the H_2O maser emission in S269 extends from 4 to 22 km/s, and is concentrated in three radial-velocity intervals: 4–7, 11–14, and 14–22 km/s. In some time intervals, the main group of emission features (14–22 km/s) had a triplet structure. The central velocity of the total spectrum is close to the velocity of the CO molecular cloud and HII region, differing from it by an amount that is within the probable dispersion of the turbulent gas velocities in the core of the CO molecular cloud. A radial-velocity drift of the component at $V_{\rm LSR} \approx 20$ km/s with a period of ≈ 26 years has been detected. This drift is likely due to turbulent (vortical) motions of material. © *2001 MAIK "Nauka/Interperiodica".*

1. INTRODUCTION

Among H_2O masers associated with star-forming regions, sources with triplet spectra are of special interest. Papers devoted to the study of such sources include those of Elmegreen and Morris [1], Grinin and Grigor'ev [2], Cesaroni [3], Lekht *et al.* [4], and Pashchenko *et al.* [5]. Triplet spectra can form in an expanding envelope or in a purely rotating torus-shaped disk (Keplerian disk) observed edge-on.

One such source whose maser emission consists of essentially three emission features is the H_2O maser S269. Its main characteristic feature is that the lateral features are located asymmetrically about the central feature; the difference between their velocities is small and does not exceed 5 km/s.

The H_2O maser is located toward the compact HII region S269. We take the distance to S269 to be the photometric distance, 3.8 kpc [7], rather than the kinematic distance, since S269 lies in the direction of the Galactic anticenter. In this case, the HII region is $\sim 3.9 \times 2.8$ pc in size, and its radial velocity, determined using a Fabry–Perot interferometer, is 16.45 ± 0.03 km/s [8]. The HII region is located in the core of a molecular cloud, which has been mapped in CO [9]. The size of the CO cloud at the half-maximum level is $7' \times 10'$, and the radial velocity of the cloud center is 17.7 km/s.

The HII region hosts the very young double infrared source IRS2 (East and West); the angular distance between its components is $4.1''$ (8×10^{17} cm) [10]. The western source, IRS2 W, is especially bright and has a large IR excess, indicating that it is very young. IRS2 W coincides spatially with and is associated with the young source IRAS 06117+1350 and, as is especially important, with type I OH and H_2O masers. Gas motions with a very high velocity (about 400 km/s) relative to the HII region are observed toward HH 191 [6].

The water-vapor maser in S269 was discovered by Lo and Burke [11] in 1973. At the time of their observations, the H_2O spectrum consisted of two emission peaks with fluxes of 70 Jy at 16.5 km/s

[*] e-mail: lekht@inaoep.mx

1063-7729/01/4512-0949$21.00

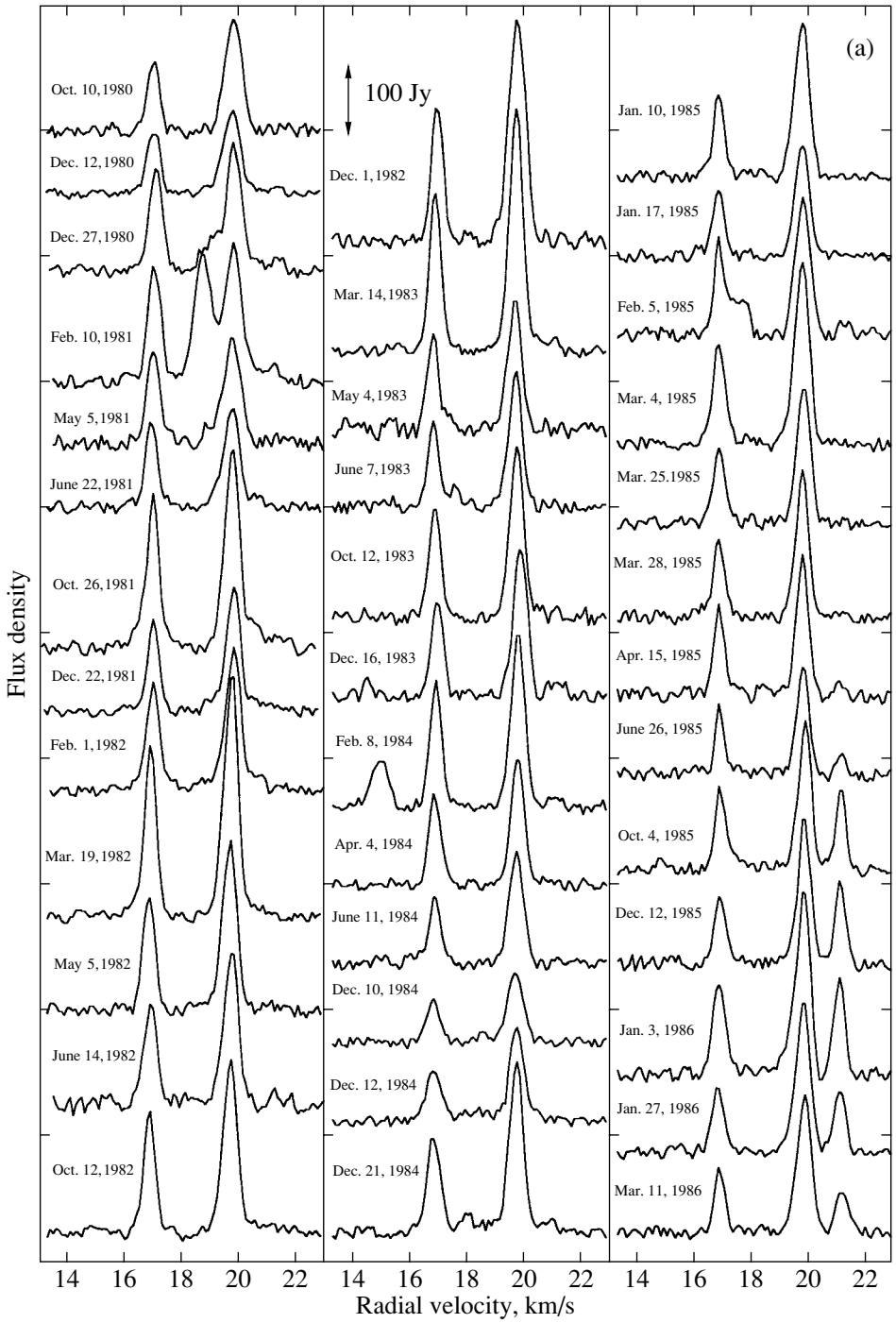

Fig. 1. Spectra of the H_2O maser emission source S269 obtained in 1980–2001. The vertical arrows in Fig. 1e show the radial velocities of the HII region and CO molecular cloud core.

and 30 Jy at 18.5 km/s. Subsequent observations [12] showed the presence of three emission features in the spectrum. Since the discovery of the H_2O maser, the emission at a velocity of about 16.5 km/s has remained most intense. The variability of this component over two years (1975–1977) was studied by White and Macdonald [13]. The triplet structure of the H_2O spectrum was also observed by Cesaroni [3] in 1988, when the central feature was the strongest.

VLBI observations in June 1996 [14] showed that

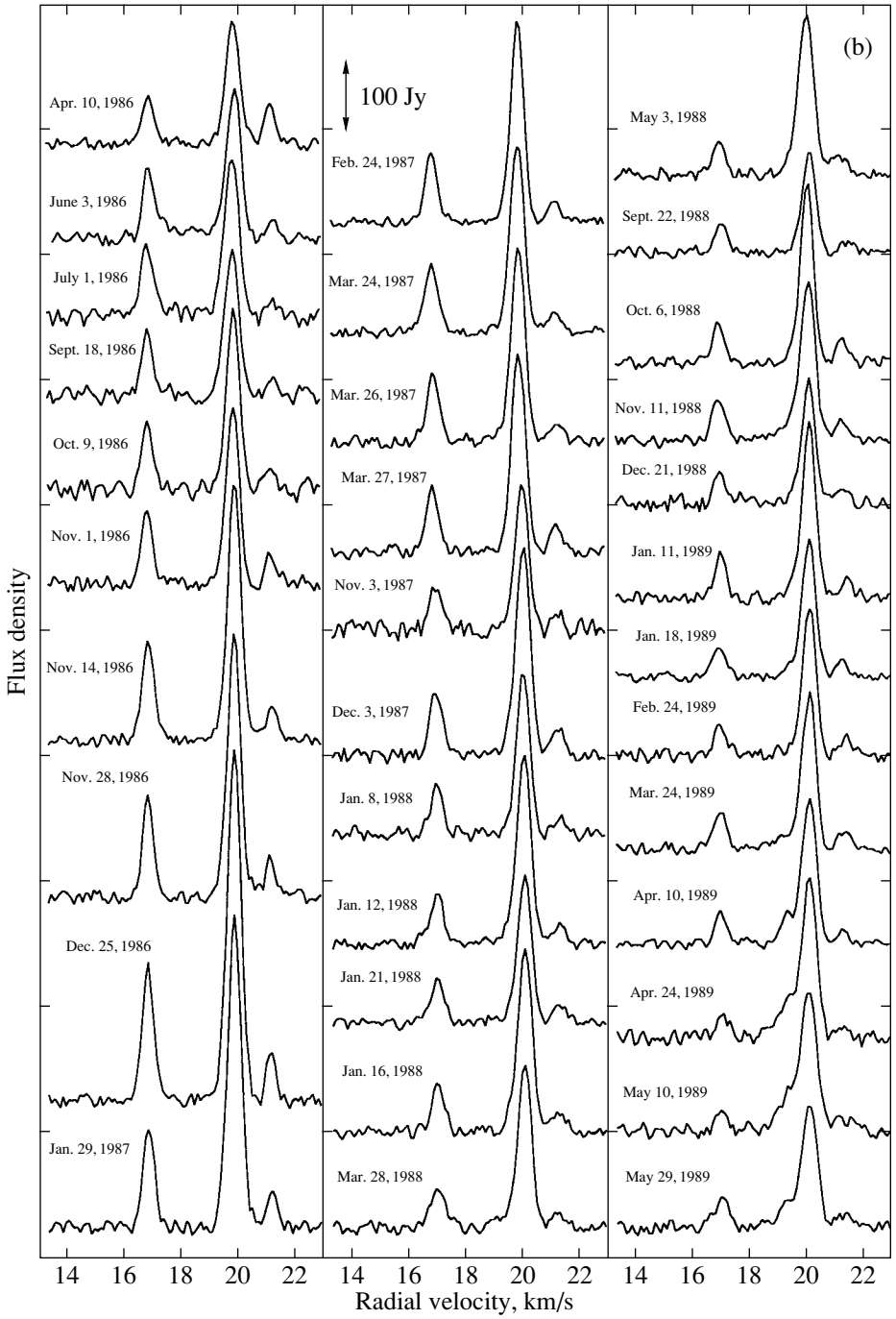

Fig. 1. (Contd.)

the maser emission probably comes from two regions separated by $\sim 1.3''$. Unfortunately, these observations were carried out during the period of lowest maser activity in the entire interval 1980 to 2001, and they therefore do not provide us with a clear picture of the H_2O maser structure in S269.

In the current work, we have studied the evolution of the H_2O maser emission in S269 on the basis of monitoring data obtained in 1980 to 2001.

2. OBSERVATIONS AND DATA PRESENTATION

Observations of the H_2O maser emission in S269 ($\alpha_{1950} = 06^h11^m46.6^s$, $\delta_{1950} = 13°50'39''$) were carried out on the 22-m telescope of the Pushchino Radio Astronomy Observatory during the roughly 20 years from October 1980, to February 2001. The mean interval between observations was 1.5 months.

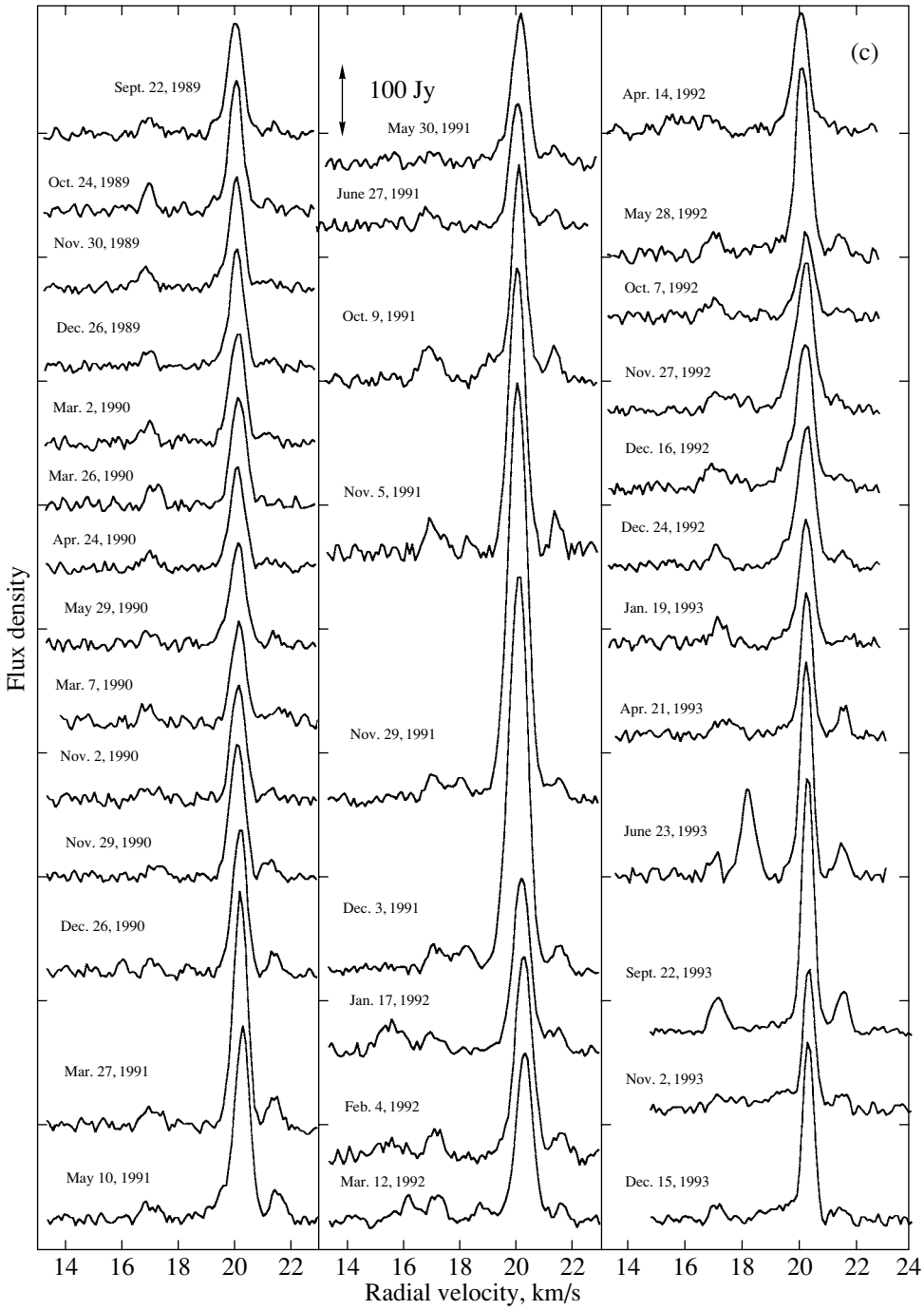

Fig. 1. (Contd.)

The noise temperature of the system with its cooled transistor amplifier was 150–230 K. There was a gap in the observations from September to December 2000, due to the installation of a new front end amplifier. The radiometer upgrade made it possible to lower the system temperature to 100–130 K. The signal analysis was performed using a 96-channel (128-channel starting in July 1997) filter-bank spectrum analyzer with a resolution of 7.5 kHz.

Figure 1 presents the results of our observations of the H_2O maser in S269. The horizontal axis plots the radial velocity relative to the Local Standard of Rest in km/s, and the vertical axis the flux density in Janskys (the scale in Janskys is shown by vertical arrows). For convenience, all the spectra are given

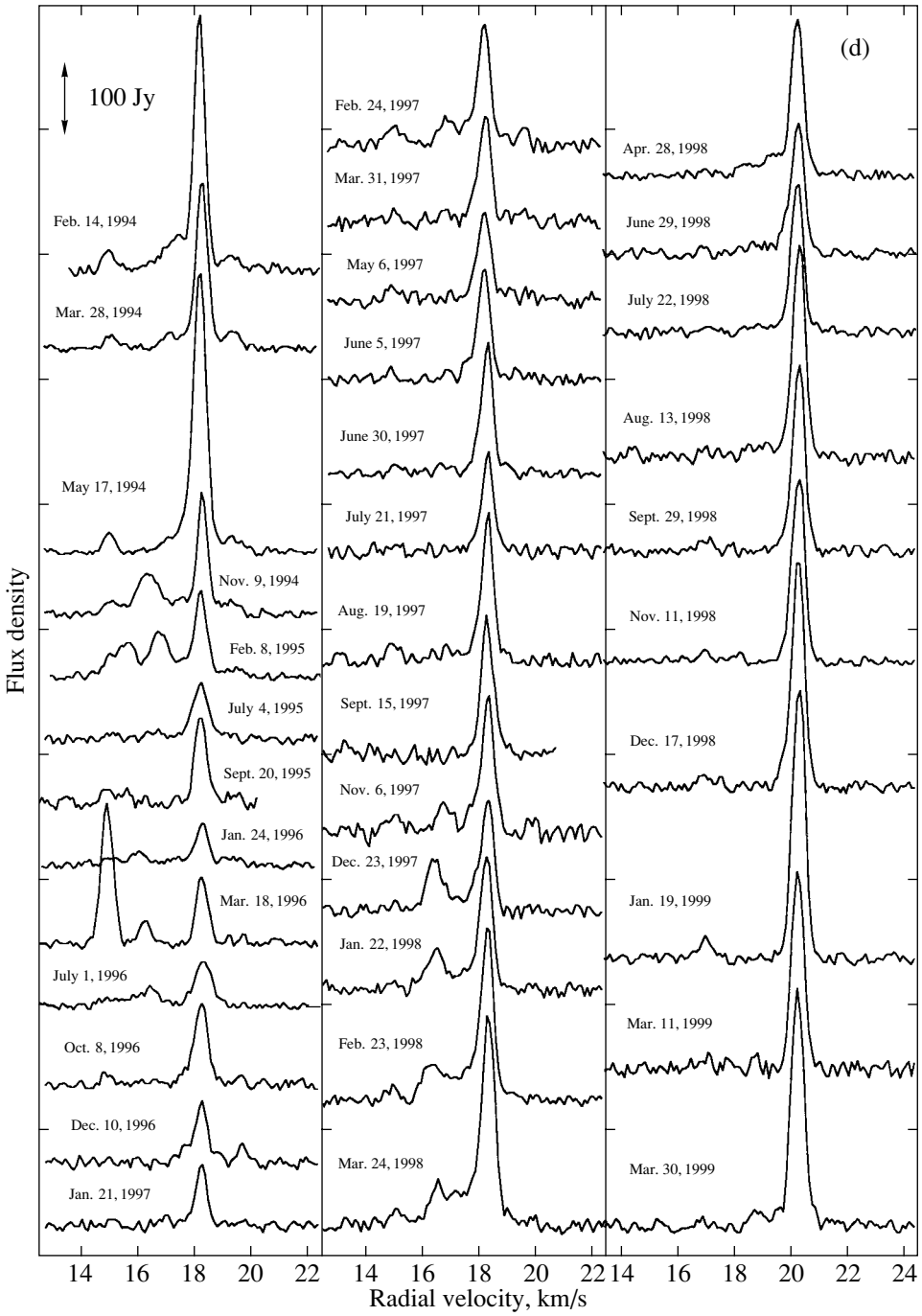

Fig. 1. (Contd).

on the same scale. We have corrected the fluxes of all spectra for atmospheric absorption. The method used for this correction is described in detail, e.g., by Rudnitskiĭ *et al.* [15]. The vertical arrows in Fig. 1e show the radial velocities of the HII region and CO molecular cloud core.

Figure 2 shows variations of the total (integrated) H_2O flux calculated for the radial-velocity interval 14–23 km/s. A cyclic variability of the total maser flux (dashed curve) can be traced. In addition, there were brief flares due to the appearance of individual short-lived emission features. In accordance with the periodic character of the variability, we have divided the interval 1980–2001 into four subintervals: (a) October 1980–January 1985, (b) February 1985–May 1990, (c) June 1990–June 1996, and (d) October 1996–February 2001. We used polynomial fitting to determine the positions of the maxima for each

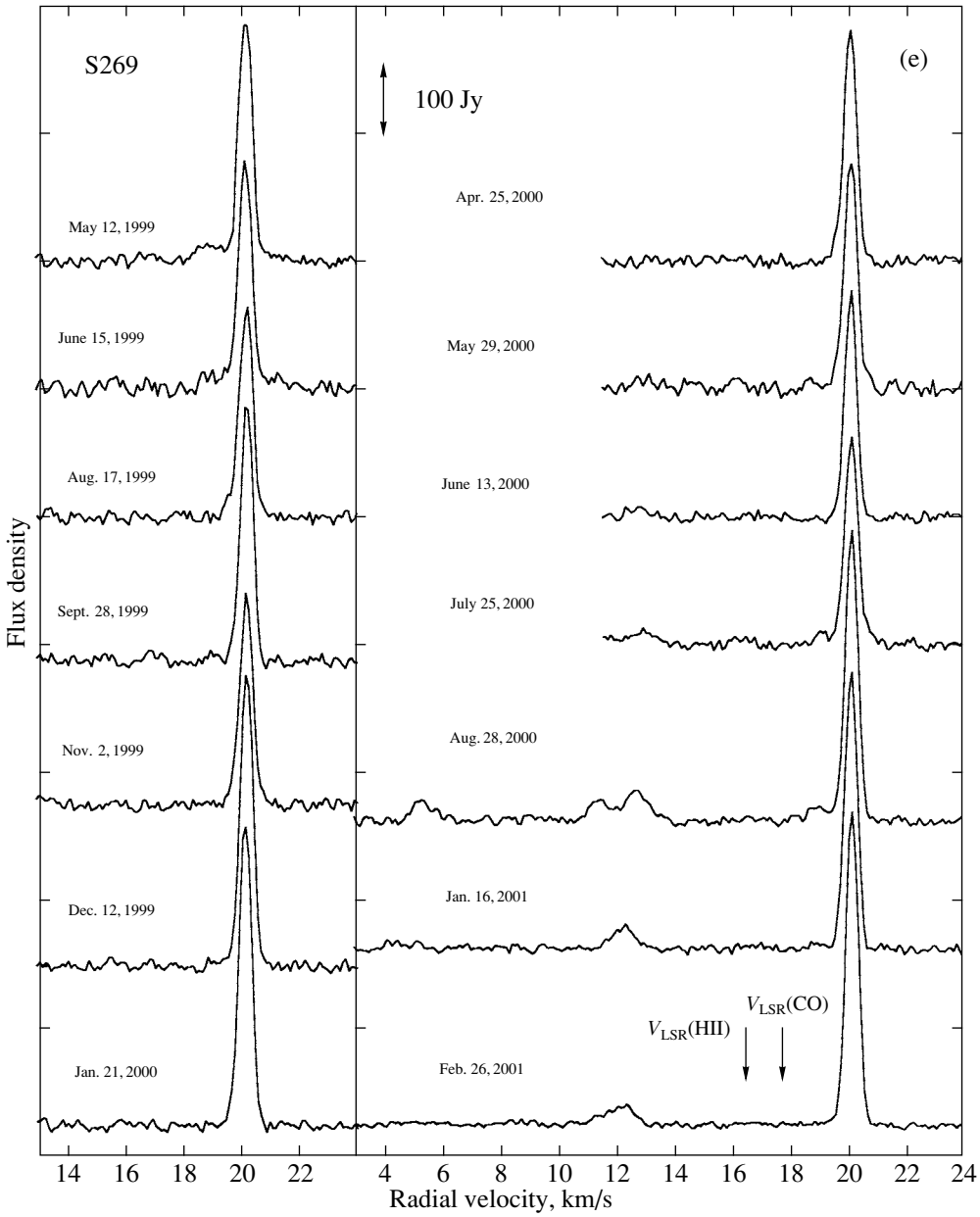

Fig. 1. (Contd.)

subinterval, which are shown in Fig. 2 by vertical arrows. The intervals between successive maxima were 4.6, 5.8, and 6.6 years; the mean period was 5.7 years.

For each time interval, we made a superposition of the spectra (Fig. 3) and an average spectrum (Fig. 4). We can clearly see that the maser emission is primarily concentrated in three radial-velocity intervals: 16.2–17.7, 19.0–20.8, and 20.8–22.0 km/s. The emission of the central group displays a drift in radial velocity. In addition, short-lived flares of the maser emission appeared episodically at radial velocities from 14–22 km/s. Similar patterns have been observed in S140 [4] and S255IR [5].

We note especially the detection of two groups of features at velocities of 4.5–7 and 11–14 km/s. Earlier (April 1985), Wouterloot *et al.* [6] observed only weak emission at 11.2 km/s. The detection of these two groups of features has considerably extended the range of the H_2O maser emission in S269. It is quite possible that the triplet structure is also present in the groups of emission features at 4.5–7, 11–14 and 16–22 km/s, not only in individual features of the third (main) group.

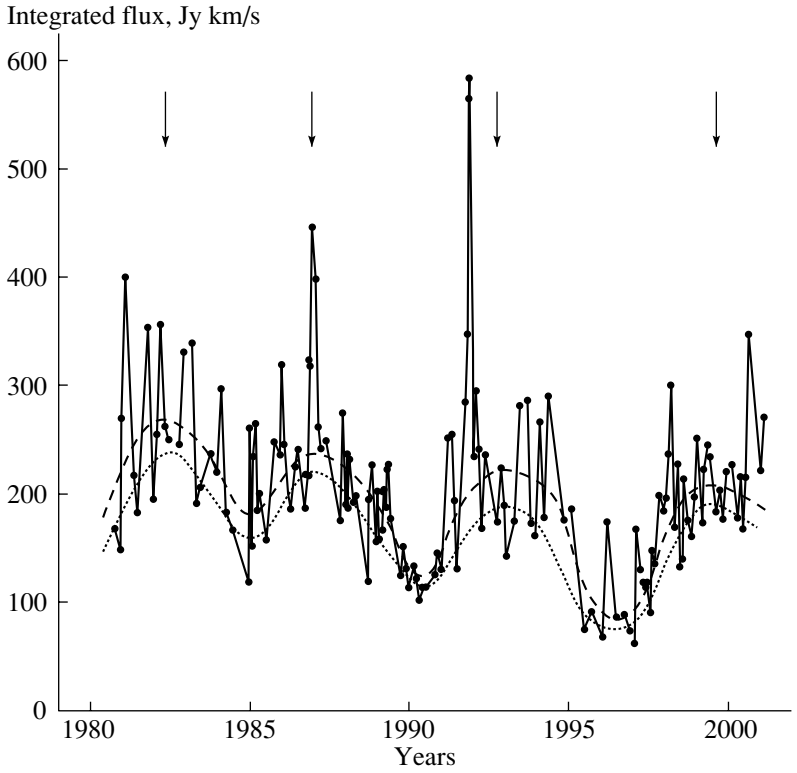

Fig. 2. Variations of the integrated flux of the H_2O maser emission of S269. The arrows show the epochs of maxima of the total flux determined from the fitted Gaussians.

Note also that the main emission peak (V_{LSR} = 20 km/s)—i.e., the most intense one during our observations—was present in all the spectra. Thus, this feature was active for at least 20 years. Figure 5 shows variations of the radial velocity of this feature. The dashed curve is the fitted polynomial and the dotted line marks the weighted mean radial velocity. We used the fitted polynomial to estimate the period and amplitude of the radial-velocity variations for the emission feature, which are 26 years and 0.27 km/s, respectively.

3. DISCUSSION

We have studied the long-term variability of the total maser flux based on our 20-year monitoring of S269 in the 1.35-cm water line. We have also traced the evolution of the main emission peak with a mean radial velocity of about 20 km/s in 1980–2001 by deriving curves for the variations of the flux, radial velocity, and line width (an analysis of these parameters will be presented in a future publication). This feature was absent from H_2O spectra obtained by other authors before 1980.

We observed another emission feature ($V_{LSR} \approx$ 17 km/s) consistently until the end of 1994, after which it only appeared episodically. There were few observations between the discovery of the maser in 1973 and the onset of our monitoring, but this feature was always present in the spectra. Hence, the lifetime of this component was also at least 20 years. Thus, both long-lived components of the S269 H_2O maser spent at least 20 years in an active emission state, however with a relative time delay of at least 7 years. The existence of an H_2O feature for more than 20 years is not typical for maser emission, and distinguishes S269 among other masers. A similar feature was observed in G43.8–0.1 at V_{LSR} = 42.2 km/s [16]. According to [4], both the long-lived emission features in S269 form a single group of maser spots. The estimated linear size of this group is 10^{16} cm.

3.1. Variability of the Integrated Flux

Our long-term monitoring of the H_2O maser S269 has enabled the detection of cyclic variability of the total maser flux. We have distinguished four cycles of the H_2O maser activity, with time intervals between the maxima of 4.6, 5.8, and 6.8 years (dashed curve in Fig. 2). In addition, there were rapid, aperiodic changes in the total flux by factors of 1.5–2.5 on timescales of about one year. The rapid variability was primarily due to variations in the flux of the main

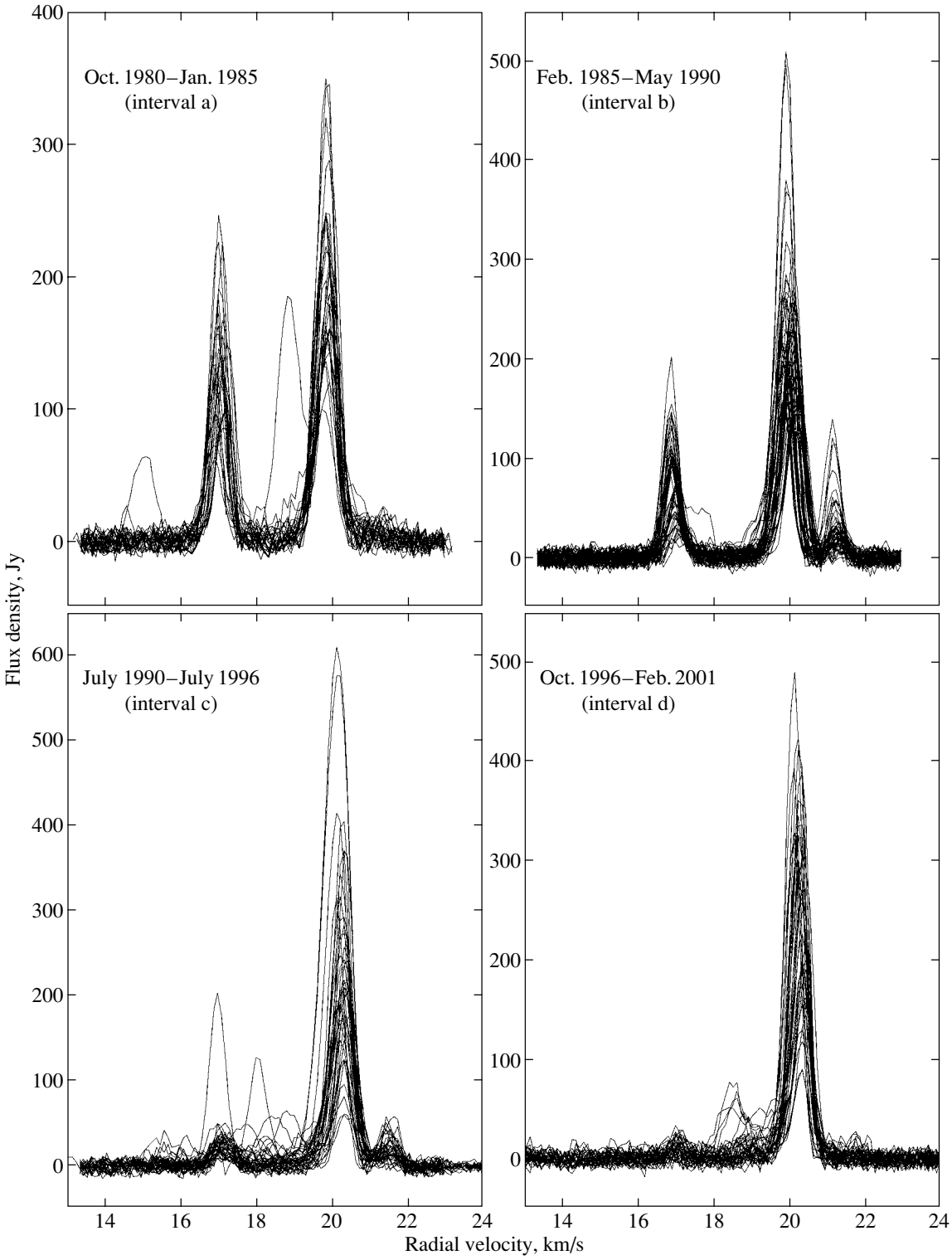

Fig. 3. Superposition of spectra of the H_2O maser S269 for various time intervals.

(long-lived) features. In some cases, there were brief flares of a single (not main) feature.

The total-flux variations can be represented by a superposition of long-period and flaring components. In this case, the long-period component of the H_2O maser variability in S269 will be described by a different curve (the dotted curve in Fig. 2), whose shape differs only slightly from that of the previous curve.

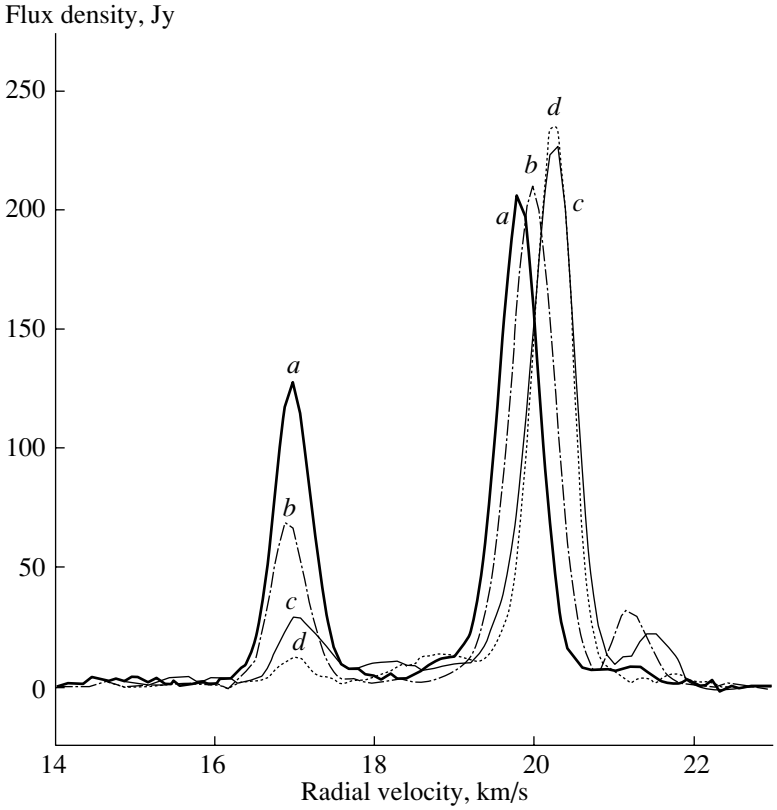

Fig. 4. Average spectra of the S269 H_2O maser for the same time intervals in Fig. 3 (curves are labeled with corresponding letters).

In spite of the rather simple H_2O spectrum of S269, the variations of the total maser flux are complex. The long-term variability with an average period of about six years could be associated with nonstationarity of the formation of the central star. This process is reflected in cyclic variations of the stellar activity, and, hence, of the H_2O maser.

Flares of individual emission features did not take place only in intervals with enhanced stellar activity, and were observed fairly regularly. It is probable that most had a local character, possibly associated with changing conditions for pumping and maser amplification.

3.2. The Structure of the H_2O Spectra

The H_2O maser spectra retained their triplet structure in some time intervals. The longest was 1985–1989. In other time intervals, only two main features were observed (here, we do not take into account weak, short-lived emission features or weak, more-or-less long-lived features in the wings of the main feature). Disappearances of individual features in the spectrum occurred independently of changes in other features; i.e., there was no anticorrelation of features' intensities, as was observed in S255 IR [5].

As noted above, in S269 (and in S140 [4]) the peculiar velocity of the water-vapor maser with respect to the molecular cloud is small. This conclusion is based on the fact that, in all previous observations, the H_2O spectrum extended in radial velocity only from 14–22 km/s. Such a narrow spectrum is not typical of masers that are associated with Keplerian disks. In view of the group of features we have detected (4.5–7 km/s), the spectrum has become considerably more extended and has obtained a form similar to the spectrum of S140. In this case, the central velocity is about 13.5 km/s, and the peculiar velocity of the source is slightly greater than 4 km/s; this is plausibly within the dispersion of turbulent gas velocities in the CO molecular cloud core.

3.3. Variability of the Radial Velocity of the Main Emission Feature

Throughout the time interval covered by our observations of S269 (1980–2001), the H_2O spectrum always contained a feature at a radial velocity of about 20 km/s. Its velocity showed nearly sinusoidal time variations (Fig. 5). Extrapolation yields a period of about 26 years. The drift amplitude was

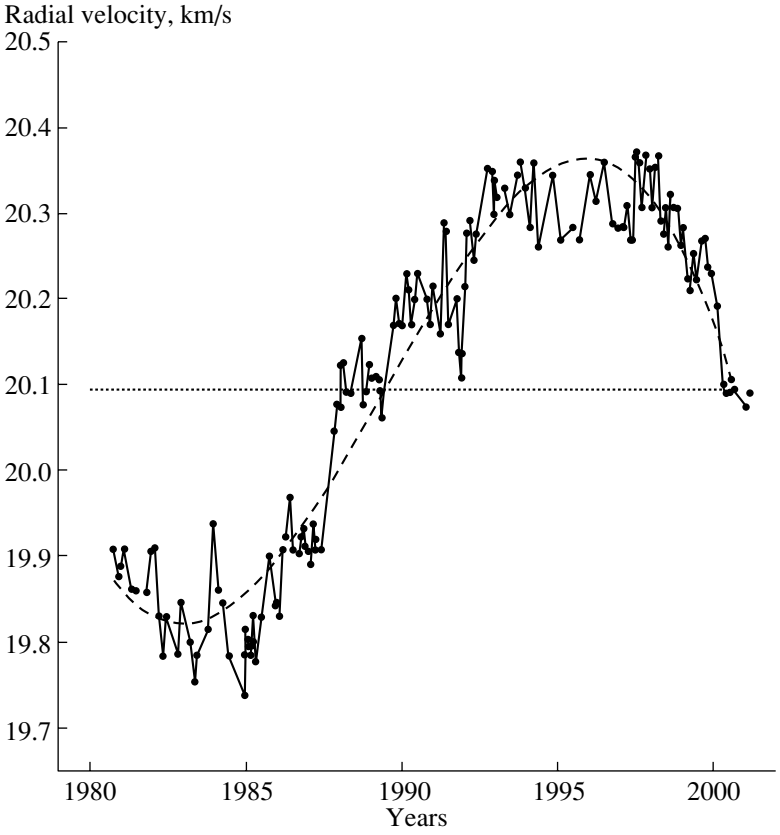

Fig. 5. Variations of the radial velocity of the main emission feature of the H_2O maser S269.

small: 0.27 km/s with respect to the mean value of 20.1 km/s. Such small changes of the radial velocity cannot be a consequence of Keplerian motion of a clump of matter (protoplanet), and most likely represent turbulent (vortical) motion of the clump.

4. CONCLUSION

We have presented the results of our monitoring of the H_2O maser S269 in 1980–2001. The following main results have been obtained.

(1) In 1980–1999, the H_2O spectra of S269 included a small number of features, which were basically located in three radial-velocity intervals: 16.2–17.7, 19.0–20.8, and 20.8–22.0 km/s.

(2) In August 2000, emission at radial velocities of 4.5–7 km/s was detected. In addition, rather than a weak single feature, emission in the range 11–14 km/s was observed.

(3) The integrated flux variations had a cyclic character with a period of from 4.8 to 6.6 years. The observed variability is most likely associated with nonstationarity of the star-formation process. This process could result in more or less cyclic variations in activity of the star and, consequently, the H_2O maser.

(4) The main emission feature ($V_{LSR} = 20$ km/s) drifted in radial velocity. The estimated period of the velocity variations is 26 years, and the amplitude is 0.27 km/s. The drift could be due to turbulent (vortical) motion of matter in a fairly stable maser region corresponding to the component at a radial velocity of about 20 km/s.

ACKNOWLEDGMENTS

The operation of the Pushchino 22-m radio telescope is supported by the Ministry of Science, Technology, and Education of the Russian Federation (facility registration number 01-10). This work was supported by the Russian Foundation for Basic Research (project no. 99-02-16293). The authors are grateful to the staff of the Pushchino Radio Astronomical Observatory for their immense help with the observations.

REFERENCES

1. B. G. Elmegreen and M. Morris, Astrophys. J. **229**, 593 (1979).
2. V. P. Grinin and S. A. Grigor'ev, Astron. Zh. **60**, 512 (1983) [Sov. Astron. **27**, 298 (1983)].

3. R. Cesaroni, Astron. Astrophys. **223**, 513 (1990).
4. E. E. Lekht, S. F. Likhachev, R. L. Sorochenko, and V. S. Strel'nitskiĭ, Astron. Zh. **70**, 731 (1993) [Astron. Rep. **37**, 367 (1993)].
5. M. I. Pashchenko, E. E. Lekht, and I. I. Berulis, Astron. Zh. **78**, 696 (2001) [Astron. Rep. **45**, 600 (2001)].
6. G. A. Wouterloot, J. Brand, and K. Fiegle, Astron. Astrophys., Suppl. Ser. **98**, 589 (1993).
7. A. F. G. Moffat, M. P. Fitzgerald, and P. D. Jackson, Astron. Astrophys., Suppl. Ser. **38**, 197 (1979).
8. S. Golbout, G. Joncas, D. Durand, and R. Arsenault, Astrophys. J. **478**, 271 (1997).
9. J. M. Carpenter, R. L. Snell, and F. P. Schloerb, Astrophys. J. **362**, 147 (1990).
10. C. Eroa, M. M. Casali, L. F. Miranda, and E. Ortiz, Astron. Astrophys. **290**, 599 (1994).
11. K. Y. Lo and B. F. Burke, Astron. Astrophys. **26**, 487 (1973).
12. R. Genzel and D. Downes, Astron. Astrophys., Suppl. Ser. **30**, 145 (1977).
13. G. J. White and G. M. Macdonald, Mon. Not. R. Astron. Soc. **98**, 589 (1979).
14. V. Migenes, S. Horiuchi, V. I. Slysh, *et al.*, Astrophys. J., Suppl. Ser. **123**, 487 (1999).
15. G. M. Rudnitskiĭ, E. E. Lekht, and I. I. Berulis, Pis'ma Astron. Zh. **25**, 467 (1999) [Astron. Lett. **25**, 398 (1999)].
16. E. E. Lekht, Astron. Astrophys., Suppl. Ser. **141**, 185 (2000).

Translated by G. Rudnitskiĭ

Astronomy Reports, Vol. 45, No. 12, 2001, pp. 960–966. Translated from Astronomicheskiĭ Zhurnal, Vol. 78, No. 12, 2001, pp. 1092–1098.

The Formation of Polarized Lines: Allowance for the Hanle Effect

S. I. Grachev

Sobolev Astronomical Institute, St. Petersburg State University,
Bibliotechnaya pl. 2, Petrodvorets, St. Petersburg, 198904 Russia

Received January 29, 2001

Abstract—The paper formulates the standard theory for the transport of polarized radiation in the presence of resonance scattering in an atmosphere with a weak magnetic field, so that the Zeeman splitting is small compared to the Doppler line width. For an atmosphere with conservative scattering, this reduces to the Milne problem, which consists of computing a polarized radiation field in a medium with sources lying in infinitely deep layers. In the approximation of complete frequency redistribution, the problem reduces to solving a Wiener-Hopf integral equation for a (6×6)-matrix source function. Asymptotic and numerical solutions for the standard problem are obtained, including solutions for the Milne problem, for the case of a Doppler absorption profile. The line polarization profiles for the emergent flux at various angular distances from the disk center are derived, and the dependence of the limiting degree of polarization (at the line center at the disk edge) on the direction of the magnetic field is computed. For nearly conservative scattering with photon destruction probability $\epsilon \ll 1$, the limiting degree of polarization varies with ϵ in accordance with a simple empirical law similar to that found earlier for a medium with zero magnetic field.

1. INTRODUCTION

The transport of polarized radiation in the presence of resonance scattering in an atmosphere with a magnetic field has become a topical problem in the past two decades, in connection with the high degrees of polarization discovered in numerous Fraunhofer lines observed near the solar limb. The effect of the magnetic field on resonance polarization (the Hanle effect) leads to the depolarization of resonance radiation and rotation of the plane of linear polarization. Numerical computations are already being carried out in order to simulate the Hanle effect, applying rather general assumptions (see, e.g., [1]). In our opinion, however, simpler models have not yet been fully analyzed.

Here, we formulate the so-called standard problem of the theory of transport of polarized radiation with allowance for the Hanle effect, and solve this problem using asymptotic and numerical methods developed earlier at the Astronomical Institute of St. Petersburg State University for the analysis of resonance polarization in a medium with zero magnetic field [2, 3]. We consider a plane-parallel medium with two-level atoms embedded in a uniform magnetic field, assumed to be sufficiently weak that induced Zeeman splitting can be neglected compared to the Doppler line width. The lower level is assumed to be unpolarized, and stimulated radiation is neglected. In this case, as was shown by Landi Degl'Innocenti *et al.* [4] and Faurobert-Scholl [5], the approximation of complete frequency redistribution reduces the problem to the solution of a vector Wiener-Hopf equation for some reduced six-component source function that depends only on the optical depth. We use a more general (matrix) form of this equation for the 6×6 matrix source function. In the standard problem, the distribution of primary sources of partially polarized radiation is assumed to be uniform (independent of depth) so that, in the limiting case of an atmosphere with conservative scattering, the sources are located at infinite depth; this corresponds to generalizing the Milne problem to the case of resonance polarization with allowance for the Hanle effect.

Section 2 presents the principle equations and relations for the standard problem including the Hanle effect. Section 3 presents asymptotic and numerical solutions for the case of a Doppler absorption profile, with subsections 3.1 and 3.2 devoted to nonconservative scattering and the Milne problem (conservative scattering with sources at infinite depth), respectively.

2. PRINCIPLE EQUATIONS AND RELATIONS

Landi Degl'Innocenti *et al.* [4] derived the principle integral equation for the density matrix ρ^K_Q ($K = 0$, $Q = 0$ and $K = 2$, $Q = 0, \pm 1, \pm 2$) of the upper level in two-level atoms under the assumptions indicated above. The density matrix is such that $\left[\rho^K_Q\right]^* = (-1)^Q \rho^K_{-Q}$, where an asterisk denotes complex conjugation. This relation enables reduction of the complex equation for ρ^K_Q to a real matrix

1063-7729/01/4512-0960$21.00

equation for the six-component vector consisting of ρ^0_0, ρ^2_0, as well as the real and imaginary parts of ρ^2_1 and ρ^2_2. Following Frisch [6], we consider the vector $\mathbf{s}=(\rho^0_0, -\rho^2_0, -2\mathrm{Re}\rho^2_1, 2\mathrm{Im}\rho^2_2, 2\mathrm{Re}\rho^2_2, 2\mathrm{Im}\rho^2_2)^{\mathrm{T}}$. We introduce the 6×6 matrix $\mathbf{S}(\tau)$ in place of the six-component column vector $\mathbf{s}(\tau)$. Then the principal integral equation for the matrix source function in the approximation of scattering with complete frequency redistribution can be written in the form:

$$[\mathbf{E}+\gamma_B\mathbf{L}(\mathbf{n}_B)]\mathbf{S}(\tau) = \int_0^\infty \mathbf{K}(\tau-\tau')\mathbf{S}(\tau')d\tau' + \mathbf{S}^*, \quad (1)$$

where γ_B depends on the magnetic field B:

$$\gamma_B = \frac{eBg_{J'}}{2mc(A+C_{J'J}+D^{(2)})}, \quad (2)$$

and the matrix $\mathbf{L}(\mathbf{n}_B)$ depends on the field direction:

$$\mathbf{L}(\mathbf{n}_B) = \begin{pmatrix} 0 & 0 & 0 & 0 & 0 & 0 \\ 0 & 0 & -\sqrt{\frac{3}{2}}\sin\theta_B\sin\varphi_B & \sqrt{\frac{3}{2}}\sin\theta_B\cos\varphi_B & 0 & 0 \\ 0 & \sqrt{6}\sin\theta_B\sin\varphi_B & 0 & \cos\theta_B & \sin\theta_B\sin\varphi_B & \sin\theta_B\cos\varphi_B \\ 0 & -\sqrt{6}\sin\theta_B\cos\varphi_B & -\cos\theta_B & 0 & \sin\theta_B\cos\varphi_B & -\sin\theta_B\sin\varphi_B \\ 0 & 0 & -\sin\theta_B\sin\varphi_B & -\sin\theta_B\cos\varphi_B & 0 & -2\cos\theta_B \\ 0 & 0 & -\sin\theta_B\cos\varphi_B & \sin\theta_B\sin\varphi_B & 2\cos\theta_B & 0 \end{pmatrix}. \quad (3)$$

In Eq. (2), A is the Einstein coefficient for spontaneous transitions; $C_{J'J}$ and $D^{(2)}$ are the rates of inelastic (type II impacts) and elastic (depolarizing) collisions, respectively; J and J' are the total angular momentum quantum numbers of the lower and upper levels, respectively; and $g_{J'}$ is the Landé factor of the upper level. In Eq. (3), $\mathbf{n}_B$ is a unit vector along the magnetic field $\mathbf{B}$; θ_B is the angle between the normal to the layers and magnetic-field vector $\mathbf{B}$; and φ_B is the azimuthal angle of the magnetic field.

The kernel matrix is normalized so that

$$\int_{-\infty}^{+\infty}\mathbf{K}(\tau)d\tau = \boldsymbol{\lambda} \equiv \mathbf{E}-\boldsymbol{\epsilon}. \quad (4)$$

Here, the single-scattering matrix albedo is:

$$\boldsymbol{\lambda} = \mathrm{diag}\{\lambda, \lambda_Q, \lambda_Q, \lambda_Q, \lambda_Q, \lambda_Q,\}, \quad (5)$$

where λ is the usual albedo,

$$\lambda_Q = \frac{7}{10}W_2\lambda', \quad \lambda' = \frac{\lambda}{1+\lambda\delta^{(2)}}, \quad (6)$$

$\delta^{(2)} = D^{(2)}/A$ is the ratio of the rate of elastic depolarizing collisions to the Einstein coefficient for spontaneous transitions (see equations (58)–(61) in [4]), and the factor W_2 takes into account depolarization due to scattering. The kernel matrix can be written as a superposition of exponential functions:

$$\mathbf{K}(\tau) = \int_0^\infty e^{-|\tau|/z}\mathbf{G}(z)dz/z \quad (7)$$

and has the form:

$$\mathbf{K}(\tau) = \begin{pmatrix} K_{11}(\tau) & K_{12}(\tau) & 0 & 0 & 0 & 0 \\ K_{21}(\tau) & K_{22}(\tau) & 0 & 0 & 0 & 0 \\ 0 & 0 & K_{33}(\tau) & 0 & 0 & 0 \\ 0 & 0 & 0 & K_{33}(\tau) & 0 & 0 \\ 0 & 0 & 0 & 0 & K_{44}(\tau) & 0 \\ 0 & 0 & 0 & 0 & 0 & K_{44}(\tau) \end{pmatrix}. \quad (8)$$

In this representation, the matrices $\mathbf{L}(\mathbf{n}_B)$ and $K(\tau)$ coincide with the corresponding matrices of Frisch [6]. Explicit expressions for the kernels were derived by Landi Degl'Innocenti *et al.* [4], who used a different normalization condition [equations (56) and (61)]. In particular, the kernels $K_{12}(\tau)$ and $K_{21}(\tau)$ have signs opposite to those used in this paper. Note that $\mathbf{K}(\tau) = \boldsymbol{\lambda}\tilde{\mathbf{K}}(\tau)$, where $\tilde{\mathbf{K}}(\tau)$ is a symmetric matrix.

The explicit representation for these kernels are:

$$K_{11}(\tau) = \frac{\lambda}{2}\int_{-\infty}^{\infty}\phi^2(x)E_1(\tau\phi(x))dx, \quad (9)$$

$$K_{11}(\tau) = \lambda\frac{\sqrt{W_2}}{4\sqrt{2}} \quad (10)$$
$$\times\int_{-\infty}^{\infty}\phi^2(x)[E_1(\tau\phi(x)) - 3E_3(\tau\phi(x))]dx,$$

$$K_{21}(\tau) = \frac{\lambda'}{\lambda}K_{12}(\tau),$$

$$K_{ii}(\tau) = \lambda' W_2 c_{i0} \quad (11)$$
$$\times\int_{-\infty}^{\infty}\phi^2(x)[c_{i1}E_1(\tau\phi(x)) + c_{i3}E_3(\tau\phi(x))$$
$$+c_{i5}E_5(\tau\phi(x))]dx,$$

where $\phi(x)$ is the absorption coefficient profile; $E_n(z) = \int_0^1 e^{-z/\mu}\mu^{n-2}d\mu$ is the nth integral exponent; and $i = 2, 3, 4$, $c_{20} = 1/8$, $c_{21} = 5$, $c_{23} = -12$, $c_{25} = 9$; $c_{30} = 3/8$, $c_{31} = 1$, $c_{33} = 1$, $c_{35} = -2$; $c_{40} = 3/16$, $c_{41} = 1$, $c_{43} = 2$, $c_{45} = 1$.

We have, according to [7],

$$\mathbf{L}_B(\mathbf{n}_B) \equiv \mathbf{L}_B(\theta_B, \varphi_B) \quad (12)$$
$$= \mathbf{R}(\varphi_B)\mathbf{L}_B(\theta_B, 0)\mathbf{R}(-\varphi_B),$$

where

$$R(\varphi) = \begin{pmatrix} 1 & 0 & 0 & 0 & 0 & 0 \\ 0 & 1 & 0 & 0 & 0 & 0 \\ 0 & 0 & c_1 & -s_1 & 0 & 0 \\ 0 & 0 & s_1 & c_1 & 0 & 0 \\ 0 & 0 & 0 & 0 & c_2 & s_2 \\ 0 & 0 & 0 & 0 & -s_2 & c_2 \end{pmatrix}, \quad (13)$$

$c_1 = \cos\varphi, s_1 = \sin\varphi, c_2 = \cos 2\varphi, s_2 = \sin 2\varphi$. Since the matrix $\mathbf{R}(\varphi)$ commutes with $\mathbf{K}(\tau)$, if it also commutes with the primary source function matrix (as, e.g., in the standard problem), we obtain

$$\mathbf{S}(\tau;\varphi_B) = \mathbf{R}(\varphi_B)S(\tau;0)\mathbf{R}(-\varphi_B), \quad (14)$$

if φ_B does not depend on depth.

The relation to the Stokes components $\mathbf{s} = (s_I, s_Q, s_U)^{\mathrm{T}}$ (the superscript T denotes transposition) for the source function in the case of sources of unpolarized radiation is given by the equation (see [6]):

$$\mathbf{s} \equiv \mathbf{s}(\tau,\mu,\varphi) = \mathbf{A}(\mu,\varphi)\mathbf{S}(\tau)\mathbf{e}_1 \quad (15)$$

where $\mathbf{e}_1 = (1,0,0,0,0,0)^{\mathrm{T}}$,

$$\mathbf{A}(\mu,\varphi) = \begin{pmatrix} 1 & \sqrt{\frac{W_2}{8}}(1-3\mu^2) & \frac{\sqrt{3W_2}}{2}\mu\sqrt{1-\mu^2}\cos\varphi & \frac{\sqrt{3W_2}}{2}\mu\sqrt{1-\mu^2}\sin\varphi & \frac{\sqrt{3W_2}}{4}(1-\mu^2)\cos 2\varphi & -\frac{\sqrt{3W_2}}{4}(1-\mu^2)\sin 2\varphi \\ 0 & \sqrt{\frac{W_2}{8}}3(1-\mu^2) & \frac{\sqrt{3W_2}}{2}\mu\sqrt{1-\mu^2}\cos\varphi & \frac{\sqrt{3W_2}}{2}\mu\sqrt{1-\mu^2}\sin\varphi & -\frac{\sqrt{3W_2}}{4}(1+\mu^2)\cos 2\varphi & \frac{\sqrt{3W_2}}{4}(1+\mu^2)\sin 2\varphi \\ 0 & 0 & -\frac{\sqrt{3W_2}}{2}\sqrt{1-\mu^2}\sin\varphi & \frac{\sqrt{3W_2}}{2}\sqrt{1-\mu^2}\cos\varphi & \frac{\sqrt{3W_2}}{2}\mu\sin 2\varphi & \frac{\sqrt{3W_2}}{2}\mu\cos 2\varphi \end{pmatrix}. \quad (16)$$

According to (15), we have for the Stokes vector of the emergent radiation $i = (I, Q, U)^{\mathrm{T}}$

$$\mathbf{i} \equiv \mathbf{i}(0,\mu,\varphi,x) = \mathbf{A}(\mu,\phi)\mathbf{I}(\mu,\phi(x))e_1, \quad (17)$$

where

$$\mathbf{I}(z) = \int_0^{\infty}\mathbf{S}(\tau)e^{-\tau/z}d\tau/z, \quad (18)$$

$\phi(x)$ is the profile of the absorption coefficient, and x is the dimensionless frequency shift relative to the line center in units of the Doppler width. In the general case of polarized sources, the column vector e_1 in (15) and (17) should be replaced by $\mathbf{e} = (1,1,1,1,1,1)^{\mathrm{T}}$.

3. ASYMPTOTIC AND NUMERICAL SOLUTIONS OF THE STANDARD PROBLEM

Numerical and asymptotic solutions are more conveniently derived using the following alternative form of the principal integral equation (1), obtained by integrating its right-hand side by parts:

$$[\boldsymbol{\epsilon} + \gamma_B\mathbf{L}_B + \mathbf{K}_2(\tau)]\mathbf{S}(\tau) \quad (19)$$
$$= \mathbf{S}^* - \int_0^{\tau}[\mathbf{K}_2(\tau') - \mathbf{K}_2(\tau)]\mathbf{S}'(\tau-\tau')d\tau'$$
$$+\int_0^{\infty}\mathbf{K}_2(\tau')\mathbf{S}'(\tau+\tau')d\tau',$$

where $\mathbf{S}'(\tau) = d\mathbf{S}(\tau)/d\tau$, and

$$\mathbf{K}_2(\tau) = \int_{\tau}^{\infty}\mathbf{K}(\tau')d\tau' \equiv \int_0^{\infty}e^{-|\tau|/z}\mathbf{G}(z)dz \quad (20)$$

is the so-called second kernel matrix. The transition to (19) is actually a regularization of the initial equation, which becomes ill conditioned at $1-\lambda \ll 1$. The accuracy of the numerical solution can be verified using the matrix law $\sqrt{\epsilon}$, which, for the standard problem (when $\mathbf{S}^* = \boldsymbol{\epsilon}^{1/2}$) with $\varphi_B = 0$, can be written [8]:

$$\mathbf{S}^{\mathrm{T}}(0)\mathbf{D}(\mathbf{E} + \gamma_B\mathbf{L}_B)\mathbf{S}(0) \quad (21)$$

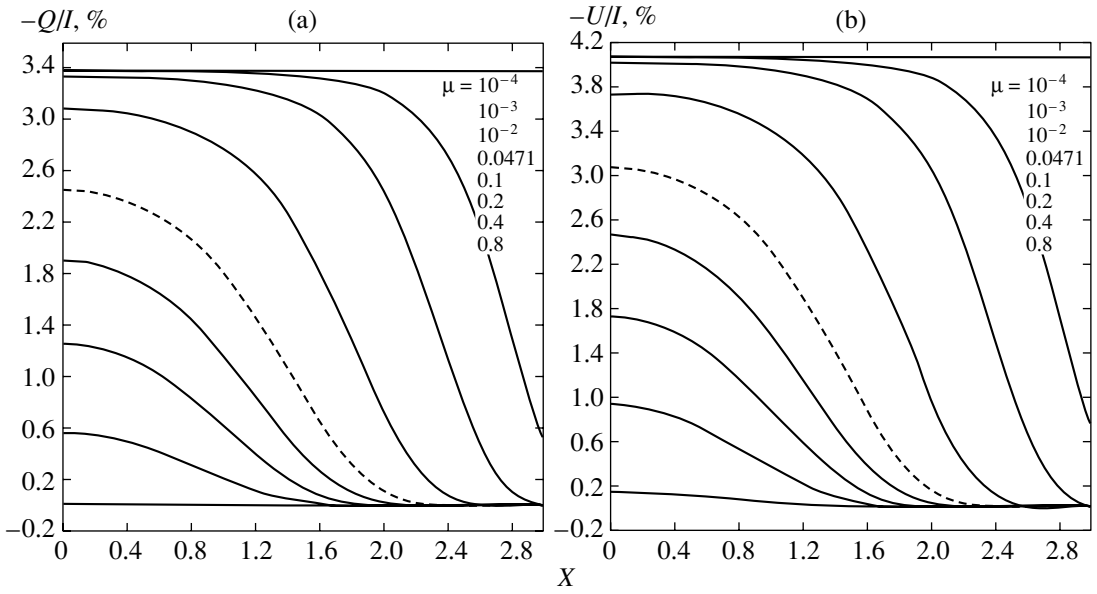

Fig. 1. Polarization profiles for the radiation emergent from the medium in the $\varphi = 0$ plane at various angles $\theta = \arccos\mu$ to the normal (curves are given in order, with the upper horizontal curve corresponding to $\mu = 0$). The horizontal axis plots the wavelength shift from the line center in units of Doppler widths. The parameter values are $\epsilon = 10^{-4}$, $\epsilon_Q = 0.3$, $\gamma_B = 1$, $\theta_B = 45^\circ$, $\varphi_B = 0$.

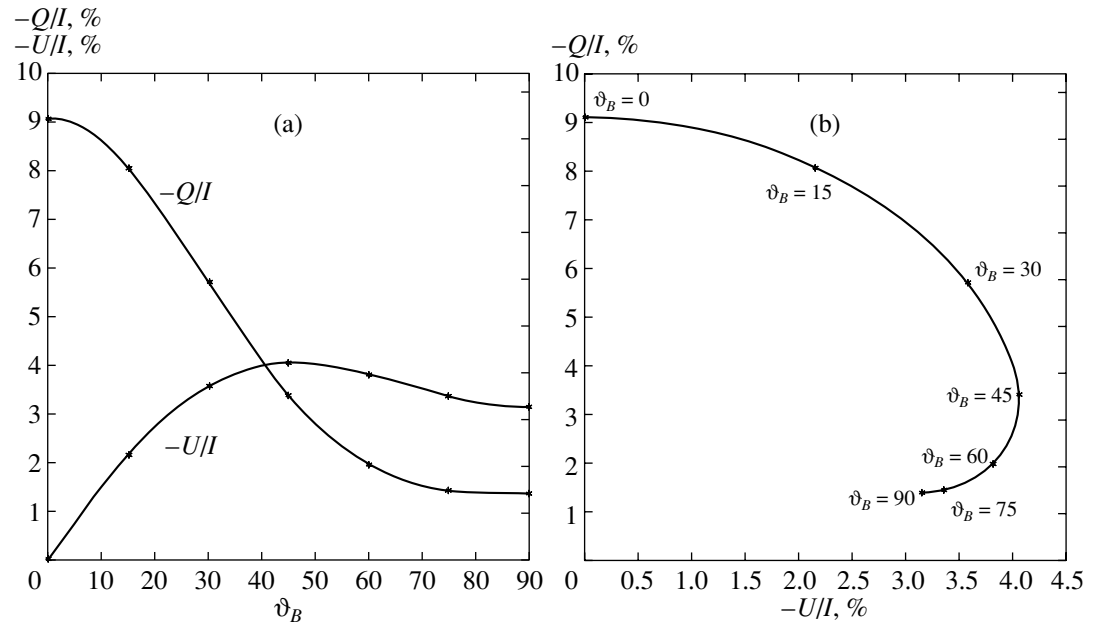

Fig. 2. Dependence of the limiting degree of polarization (for $x = 0$, $\mu = 0$, and $\varphi = 0$) on the polar angle of the magnetic field θ_B. Parameter values are the same as in Fig. 1.

$$= \mathbf{D}[\mathbf{E} + \gamma_B \boldsymbol{\epsilon}^{-1/2}\mathbf{L}_B\boldsymbol{\epsilon}^{-1/2}]^{-1},$$

where the diagonal matrix is

$$\mathbf{D} = \mathrm{diag}\left\{\frac{\lambda'}{\lambda},\ 1, \frac{1}{2},\ -\frac{1}{2},\ \frac{1}{2},\ -\frac{1}{2}\right\}. \qquad (22)$$

Asymptotic expansions of the matrix $\mathbf{I}(z)$ follow (as in the case of zero magnetic field) from the linear equation obtained by applying a Laplace transform to (1):

$$[\boldsymbol{\epsilon} + \gamma_B\mathbf{L}_B]\mathbf{I}(z) \qquad (23)$$

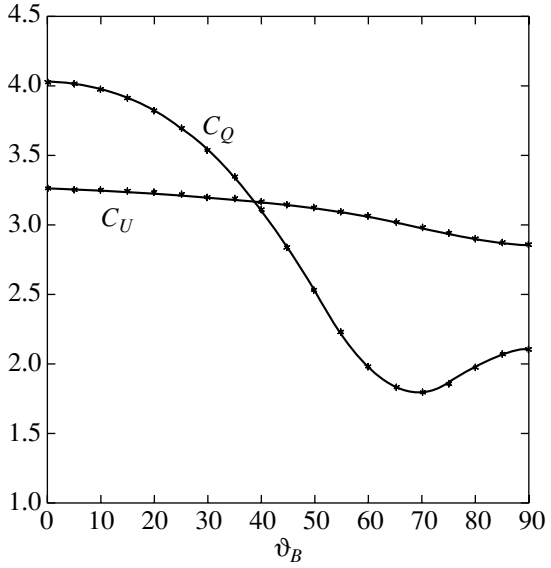

Fig. 3. Dependence of coefficients $c_{Q,U}$ on θ_B in the empirical law $\delta_{Q,U}(\epsilon) = \delta_{Q,U}(0)(1 - c_{Q,U}\sqrt{\epsilon})$ for the limiting degree of polarization.

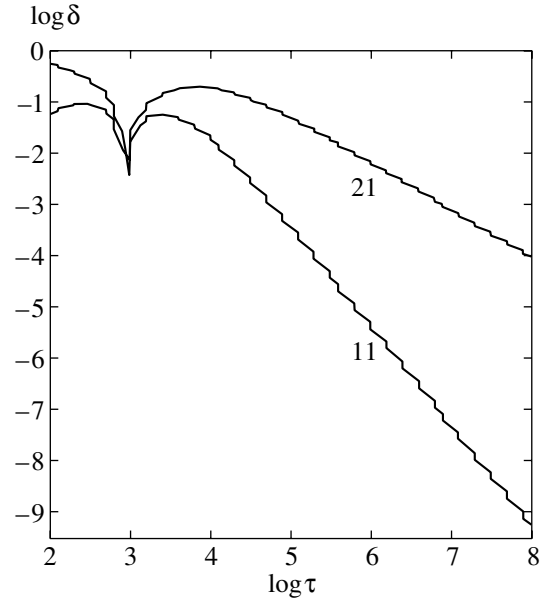

Fig. 4. Comparison of asymptotic and numerical solutions for the matrix source function. The vertical axis plots the logarithm of the absolute value of the corresponding difference. The parameter values are $\epsilon = 10^{-4}$, $\epsilon_Q = 0.3$, $\gamma_B = 1$, $\theta_B = 90^\circ$, $\varphi_B = 0$.

$$= \mathbf{S}^* + \int_0^\infty \mathbf{G}(z')[(z+z')\mathbf{I}(z') - 2z'\mathbf{I}(z)]\frac{z'dz'}{z'^2 - z^2}.$$

This equation can also be rewritten in the (regularized) form

$$[\boldsymbol{\epsilon} + \gamma_B\mathbf{L}_B + \mathbf{W}(z)]\mathbf{I}(z) \qquad (24)$$

$$= \mathbf{S}^* + \int_0^\infty \mathbf{G}(z')[\mathbf{I}(z') - \mathbf{I}(z)]\frac{z'dz'}{z' - z},$$

where

$$\mathbf{W}(z) = \int_o^\infty \mathbf{G}(z')\frac{z'dz'}{z' + z}. \qquad (25)$$

We also earlier [8] obtained the following nonlinear equation for the matrix $\mathbf{I}(z)$ for the standard problem (when $\mathbf{S}^* = \boldsymbol{\epsilon}^{1/2}$) with $\varphi_B = 0$:

$$\mathbf{I}(z)[\mathbf{E} + \gamma_B\boldsymbol{\epsilon}^{-1/2}\mathbf{L}_B\boldsymbol{\epsilon}^{1/2}] \qquad (26)$$
$$\times \left[\boldsymbol{\epsilon}^{1/2} + \int_0^\infty \mathbf{D}^{-1}\mathbf{I}^{\mathrm{T}}(z')\mathbf{D}\mathbf{G}(z')\frac{z'dz'}{z + z'}\right] = \mathbf{E},$$

where the diagonal matrix $\mathbf{D}$ is given by (22) above. Note that the structure of $\mathbf{L}_B$ is such that the first element of $\boldsymbol{\epsilon}^{-1/2}$ does not enter the product $\boldsymbol{\epsilon}^{-1/2}\mathbf{L}_B\boldsymbol{\epsilon}^{-1/2}$. Namely,

$$\boldsymbol{\epsilon}^{-1/2}\mathbf{L}_B\boldsymbol{\epsilon}^{-1/2} = \epsilon_Q^{-1}\mathbf{L}_B, \qquad (27)$$

where $\epsilon_Q = 1 - \lambda_Q$.

We obtained all solutions for the case of the Doppler absorption profile ($\phi(x) = \pi^{-1/2}e^{-x^2}$), neglecting depolarizing elastic collisions in the numerical computations ($\delta^{(2)} = 0$). As in the case of zero magnetic field [3], in the numerical solutions of (19), we approximated the matrix $\mathbf{S}$ as a quadratic spline on the grid $\{\tau_i\}$ $(i = 0, 1, \ldots, N)$, where $\tau_0 = 0$ and the logarithms of other grid points are distributed uniformly over the interval $-3 \le \log\tau_i \le 10$ $(i = 1, \ldots, N)$. To increase the speed of computation of the components $K_2^{ik}(\tau)(i = 1, 2)$, $K_2^{33}(\tau)$, and $K_2^{44}(\tau)$ of the second kernel matrix, we used high-accuracy rational approximations in τ for $\tau \le \tau_{ik}$ and in $\ln(\tau/\sqrt{\pi})$ for $\tau \ge \tau_{ik}$. The joining points τ_{ik} (different for different components) were chosen to provide maximum approximation accuracy for all τ. The new rational approximations of the kernel functions $K_2^{ik}(\tau)(i = 1, 2)$ proved to be more accurate than those in the literature, including those we used in our previous work [3]. For example, the maximum fractional error of the computed $K_2^{12}(\tau)$ and $K_2^{21}(\tau)$ decreased by an order of magnitude, and does not exceed 10^{-4} in the new computations.

We now consider the two main cases of scattering, taking into account the magnetic field (the Hanle effect): (1) nonconservative scattering ($\epsilon > 0, \epsilon_Q > 0$), and (2) conservative scattering ($\epsilon = 0, \epsilon_Q > 0$).

3.1. Nonconservative Scattering

Asymptotic expansions are derived in the same way as in the case of zero magnetic field [9]. We have, after discarding the integral terms on the right-hand side of (19),

$$\mathbf{S}(\tau) \sim [\boldsymbol{\epsilon} + \gamma_B \mathbf{L}_B + \mathbf{K}_2(\tau)]^{-1} \mathbf{S}^*. \quad (28)$$

Similarly, we obtain from (24)

$$\mathbf{I}(z) \sim [\boldsymbol{\epsilon} + \gamma_B \mathbf{L}_B + \mathbf{W}(z)]^{-1} (\mathbf{S}^* + \boldsymbol{\omega}/z), \quad (29)$$

where

$$\boldsymbol{\omega} = \int_0^\infty \mathbf{G}(z)[\mathbf{I}(\infty) - \mathbf{I}(z)] z dz. \quad (30)$$

As an example, we derived numerical solutions for the standard problem ($\mathbf{S}^* = \boldsymbol{\epsilon}^{1/2}$) for $\gamma_B = 1$, $\epsilon = 10^{-4}$ and $\epsilon = 10^{-6}$, $\epsilon_Q = 0.3$, $\gamma_B = 0$, and various θ_B. The number of discretization points (excluding $\tau_0 = 0$) was $N = 100$. We assumed that $\mathbf{S}'(\tau) = 0$ when $\tau \geq \tau_N$, and considered the case of nonpolarized primary radiation sources, which corresponds to the first column of the matrix $\mathbf{S}(\tau)$. We followed the solutions as they approached the asymptotic relation (28). Formula (17) was used to construct the polarization frequency profiles for the radiation emerging from the medium at various angles $\theta (\mu = \cos\theta)$ to the external normal, with the azimuth angle $\varphi = 0$ (Fig. 1). When $\theta_B = 0$, the pattern is obviously azimuthally symmetric and the magnetic field has no effect on the polarization characteristics of the radiation. The effect of the magnetic field increases with increasing θ_B: the degree of polarization $-Q/I$ decreases, and $-U/I$ increases. The polarization profiles (dashed curve in Fig. 1) are in qualitative (visual) agreement with those computed by Faurobert-Scholl [5]. Figure 2 shows the dependence of the limiting degree of polarization (at the line center at the disk limb) on the polar angle of the magnetic field. We verified that, as in the case of zero magnetic field [3], the maximum polarizations $\delta_Q(\epsilon) \equiv -Q(\mu = 0, x = 0)/I(\mu = 0, x = 0)$ and $\delta_U(\epsilon) \equiv -U(\mu = 0, x = 0)/I(\mu = 0, x = 0)$ obey the empirical law $\delta_{Q,U}(\epsilon) = \delta_{Q,U}(0)(1 - c_{Q,U}\sqrt{\epsilon})$. Figure 3 shows the dependence of the coefficients $c_{Q,U}$ on θ_B. The fractional difference between $\delta_{Q,U}(0)$ values extrapolated using this law and obtained from the numerical salutations for $\epsilon = 0$ (see next section) does not exceed 10^{-5}.

By means of illustration, Fig. 4 compares the asymptotic and numerical solutions for the components S_{11} and S_{21} of the matrix $\mathbf{S}$ for $\gamma_B = 1$, $\epsilon = 10^{-4}$, $\epsilon_Q = 0.3$, $\varphi_B = 0$, and $\theta_B = 90°$. (The plots of S_{k1} for $k > 2$ are indistinguishable from those of S_{21}.) The number of discretization points here has been doubled.

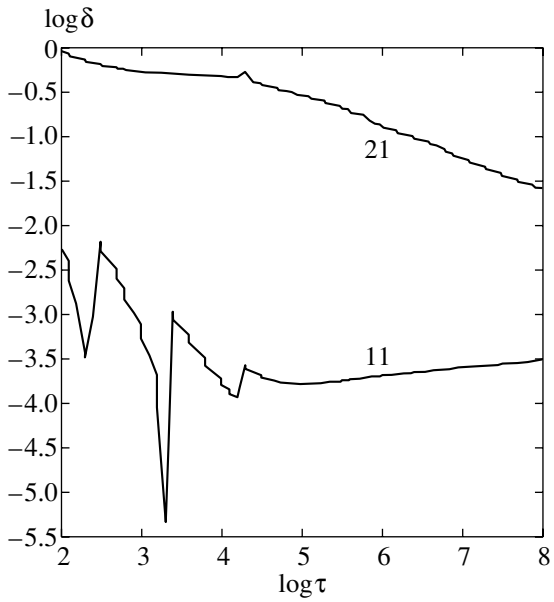

Fig. 5. Same as Fig. 4 for $\epsilon = 0$: conservative scattering (the Milne problem).

3.2. Conservative Scattering

Asymptotic expansions can be derived using the same method as in the case of zero magnetic field [9]. The asymptotic values of the elements of the matrix source function can be expressed explicitly in terms of the corresponding asymptotic values of the zero-field case, denoted $S_{ik}^{as}|_{B=0}$, $i, k = 1, 2$. Consider, for example, the first column of the source-function matrix $\mathbf{s} = (S_{11}, S_{21}, \ldots, S_{61})^{\mathrm{T}}$. The asymptotic expansion of the element $S_{11}(\tau)$ is the same as in the scalar case, and the expansions of other elements making up the column vector $\tilde{\mathbf{s}} \equiv (S_{21}, S_{31}, \ldots, S_{61})^{\mathrm{T}}$ have the same form as the asymptotic expansion of the element S_{21} in the case of zero field. To be more exact, these latter expansions are derived from the solution of the following system of linear equations:

$$\left(\tilde{\mathbf{E}} + \frac{\gamma_B}{\epsilon_Q}\tilde{\mathbf{L}}_B\right) \mathbf{s}^{as}(r) = |_{B=0}, \tilde{\mathbf{s}}^{as}(\tau)|_{B=0}, \quad (31)$$

where $\tilde{\mathbf{E}} = \mathrm{diag}\{1, 1, 1, 1, 1\}$, $\tilde{\mathbf{L}}_B$ is the matrix $\mathbf{L}_B$ without its first column and first row (a 5×5 matrix), and $\tilde{\mathbf{s}}^{as}(\tau)|_{B=0} = (S_{21}^{as}|_{B=0}, 0, 0, 0, 0)^{\mathrm{T}}$. We then have for the elements of the first row S_{1k} ($k = 2, \ldots, 6$):

$$S_{1k}^{as} = c_{2k} S_{12}^{as}|_{B=0}, \quad (32)$$

where c_{2k} are the elements of the first row of $\mathbf{c}$ determined from (34) below. The expansions of other elements S_{ik} ($i, k = 2, \ldots, 6$) making up the 5×5 matrix $\tilde{\mathbf{S}}$ have the same form as the expansion of S_{22} in the case of zero magnetic field:

$$\tilde{\mathbf{S}}(\tau) \sim \epsilon_Q^{1/2} \mathbf{c} + \left[S_{22}^{as}(\tau)|_{B=0} - \epsilon_Q^{-1/2}\right] \mathbf{b}. \quad (33)$$

Here, the matrix $\mathbf{c} = \{c_{ik}\}$, $i, k = 2, \ldots, 6$ is determined from the equation

$$\left(\tilde{\mathbf{E}} + \frac{\gamma_B}{\epsilon_Q}\tilde{\mathbf{L}}_B\right)\mathbf{c} = \tilde{\mathbf{E}} \tag{34}$$

and $\mathbf{b}$ is determined from the equation

$$\left(\tilde{\mathbf{E}} + \frac{\gamma_B}{\epsilon_Q}\tilde{\mathbf{L}}\right)\mathbf{b} = \tilde{\mathbf{c}}, \tag{35}$$

where $\tilde{\mathbf{c}}$ is the matrix $\mathbf{c}$ with only its first row preserved and other elements set equal to zero.

The asymptotic expansions of the matrix $\mathbf{I}(z)$ can be obtained in a similar way.

We obtained numerical solutions in the same way as in the case of zero magnetic field [3]. When computing the integral residuals, we took into account only terms of the form

$$\int_{\tau_N}^{\infty} \mathbf{K}_2(\tau' - \tau) S'_{11}(\tau') d\tau', \tag{36}$$

using the known (scalar) asymptotic expansion for $S_{11}(\tau)$.

Figure 5 compares the asymptotic and numerical solutions for components S_{11} and S_{21} of the matrix $\mathbf{S}$ for $\gamma_B = 1$, $\epsilon_Q = 0.3$, $\varphi_B = 0$, and $\theta_B = 90°$. (The plots for S_{k1} when $k > 2$ are indistinguishable from that for S_{21}.) As in Fig. 4, the number of discretization points used for these plots was doubled, $N = 200$. We can see that the accuracy of the asymptotic expansions for components $S_{k1}(\tau)$ with $k \geq 2$ is much lower than for $S_{11}(\tau)$, and that, when $\tau > 10^5$, the asymptotic expansion of $S_{11}(\tau)$ yields more accurate results than the numerical solution. Note that the accuracy of the asymptotic expansions is virtually independent of the polar angle θ_B of magnetic field.

4. CONCLUSIONS

We have shown that the analytical and numerical solutions for the standard problem of polarized radiation transport theory with resonance scattering developed in [2, 3] can be easily generalized to the case of atmospheres with weak magnetic fields (the so-called Hanle effect). The resulting asymptotic expansions of the source-function matrix $\mathbf{S}(\tau)$ and the matrix $\mathbf{I}(z)$ (actually the Laplace transform of $\mathbf{S}(\tau)$) are similar in both form and accuracy to those derived earlier for the case of zero magnetic field. These expansions were used to efficiently monitor the accuracy of the numerical computations.

5. ACKNOWLEDGMENTS

I am grateful to V.V. Ivanov and D.G. Sidorin for useful discussions in the course of the work. This work was supported by the Russian Foundation for Basic Research (project no. 00-02-16870a), the Council for the Support of Leading Scientific Schools (project no. 00-15-96607), and the Federal Research and Technology Program "Astronomy."

REFERENCES

1. K. N. Nagendra and J. O. Stenglo, *Proceedings of the 2nd Solar Polarization Workshop: Solar Polarization* (Dordrecht, Kluwer, 1999).
2. V. V. Ivanov, S. I. Grachev, and V. M. Loskutov, Astron. Astrophys. **318**, 315 (1997).
3. V. V. Ivanov, S. I. Grachev, and V. M. Loskutov, Astron. Astrophys. **321**, 968 (1997).
4. E. Landi Degl'Innocenti, V. Bommier, and S. Sahal-Brechot, Astron. Astrophys. **235**, 459 (1990).
5. M. Faurobert-Scholl, Astron. Astrophys. **246**, 469 (1991).
6. H. Frisch, Astron. Astrophys. **338**, 683 (1998).
7. K. N. Nagendra, H. Frisch, and M. Faurobert-Scholl, Astron. Astrophys. **332**, 610 (1998).
8. S. I. Grachev, Astrofizika **44**, 455 (2001).
9. S. I. Grachev, Astrofizika **43**, 95 (2000).

Translated by A. Dambis

Astronomy Reports, Vol. 45, No. 12, 2001, pp. 967–971. Translated from Astronomicheskiĭ Zhurnal, Vol. 78, No. 12, 2001, pp. 1099–1103.

Acceleration of Close Binaries in Supernova Explosions

V. D. Pal'shin and A. I. Tsygan

Ioffe Physicotechnical Institute, Russian Academy of Sciences, Politekhnicheskaya ul. 26, St. Petersburg, 194021 Russia

Received January 18, 2001

Abstract—We investigate the orientation of the orbital planes of X-ray binary systems relative to the direction of the additional velocity acquired by the binary in a supernova explosion or as a result of radiative acceleration. In the second case, the acceleration occurs due to X-ray radiation during a stage of intense accretion onto the neutron star, which has an asymmetric magnetic field. Observational consequences that could enable estimation of the role of each acceleration mechanism are discussed. The results are also applicable to binary millisecond radio pulsars, assuming that they have gone through an accretion stage.

1. INTRODUCTION

Recently, we indicated the possibility that X-ray binaries could be accelerated by their own radiation when the magnetic field of the neutron star in the system is not axisymmetric [1]. The acceleration results from the asymmetry of the X-ray radiation. After averaging over the rotation period of the neutron star, a force component remains and is directed along the rotation axis. The radiation reaction force $F = \xi L_X/c$ depends on the X-ray luminosity of the neutron star $L_X = \dot{m}c^2 r_g/2a$ ($\dot{m}$ is the rate of accretion from the normal companion, c the velocity of light, a the radius of the neutron star, r_g the gravitational radius of a neutron with a mass m_3, and $r_g/a = 0.4$ for $m_3 = 1.4M_\odot$ and $a = 10^6$ cm) and the asymmetry parameter of the X-ray radiation ξ ($\xi = \int \Psi(\theta,\phi)\cos\theta d\Omega$, where $\Psi(\theta,\phi)$ is the beam of the X-ray radiation of the neutron star in spherical coordinates with the z axis directed along the rotation axis of the neutron star, $\int \Psi(\theta,\phi)d\Omega = 1$).

For $\dot{m} = 3\times10^{-9}M_\odot/\mathrm{yr} = 2\times10^{17}$ g/s and $\xi = 0.2$, the force F_X is equal to 2.7×10^{26} dynes, which exceeds the gravitational attraction of a binary in the Sun's Galactic orbit toward the Galactic center by a factor of 2.6 (for a mass of the system equal to $2.5M_\odot$). In the case of disk accretion onto a neutron star, its rotation axis should fairly quickly become normal to the plane of the disk (and to the orbital plane), over a time of $\sim 10^5$ yrs for a magnetic field $\sim 10^{12}$ G (as compared to the timescale for mass transfer, $\tau \sim 10^7$ yrs). Thus, the binary will be accelerated normal to the orbital plane by the asymmetric X-ray radiation.

The system acquires an additional velocity $v_s = \int F_X dt/(m_2+m_3) = (c\xi r_g/2a)(m_2+m_3)^{-1}\times\int \dot{m}dt$, which is specified by the mass $\Delta m = \int \dot{m}dt$ of matter that has flowed onto the neutron star; m_2 is the mass of the companion and m_3 the mass of the neutron star (this formula is valid when the accretion time τ is much shorter than the orbital period of the binary about the Galactic center, $T \simeq 2.2\times10^8$ yrs for a Galactocentric radius of 8.5 Kpc). We assume that the strength of the magnetic field affecting the accretion flux and forming the asymmetrical beam of X-ray radiation is $\gtrsim 10^9$ G. During the accretion, the magnetic field of the neutron star may evolve such that the asymmetry parameter varies (and even changes sign). However, it is reasonable to assume that the asymmetry parameter ξ does not vary significantly over the time τ.

For $\Delta m = 0.1M_\odot$ and $m_2 + m_3 = 2.5M_\odot$, we obtain $v_s = 2.4\times10^3\xi$ km/s [1]. This estimate indicates that low-mass X-ray binaries with $\xi \simeq 0.2$ acquire fairly high velocities and can reach large heights above the Galactic plane z. It is obvious that binaries whose orbital planes lie in the plane of the Galaxy should predominate among such systems. On the contrary, binaries with orbital planes oriented normal to the plane of the Galaxy should predominate near the Galactic plane. Note that low-mass X-ray binaries have characteristic heights above the Galactic plane of about 900 pc [2]. These arguments are also applicable to millisecond radio pulsars in binary systems if they have gone through a stage of intense accretion during the spin-up of the neutron star [3, 4]. The mechanism proposed by Harrison and Tademaru [5] (acceleration of the neutron star by asymmetric

1063-7729/01/4512-0967$21.00

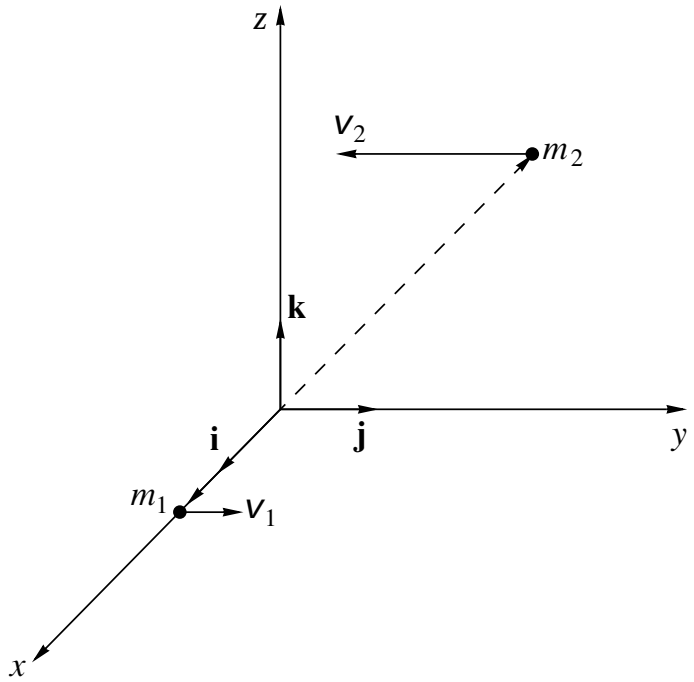

Fig. 1. Coordinate system used to describe the binary. The z axis is normal to the orbital plane of the binary before the explosion. The x axis is chosen so that the stars lie along this axis at the time of the explosion.

radiation generated by a rotating magnetic dipole displaced relative to the center of the star) is effective only for rapidly rotating neutron stars ($\Omega \sim 10^4$ s^{-1} for magnetic fields $\sim 10^{12}$ G); in this case, the acceleration continues for about a year. Another better-known way in which a binary can acquire an additional velocity is in the supernova explosion (symmetrical or asymmetrical) that led to the formation of the neutron star. Note that, in a symmetrical supernova explosion, the additional velocity acquired by the binary $\mathbf{v}_s$ is in the orbital plane of the system. This is not the case for an asymmetrical supernova.

2. ORBITAL PLANE OF THE BINARY RELATIVE TO THE ADDITIONAL VELOCITY ACQUIRED IN AN ASYMMETRICAL SUPERNOVA EXPLOSION

Let us consider a binary system with components with masses m_1 and m_2, with circular orbits in the center-of-mass coordinate frame:

$$m_2\mathbf{r}_2 + m_1\mathbf{r}_1 = 0, \qquad (1)$$
$$m_2\mathbf{v}_2 + m_1\mathbf{v}_1 = 0.$$

The relative velocity is

$$\mathbf{v} = \mathbf{v}_1 - \mathbf{v}_2 = \mathbf{v}_1 + \frac{m_1}{m_2}\mathbf{v}_1 = \frac{m_1 + m_2}{m_2}\mathbf{v}_1. \qquad (2)$$

The velocity v is determined by the expression

$$v^2 = \frac{G(m_1 + m_2)}{r},$$

where $\mathbf{r} = \mathbf{r}_1 - \mathbf{r}_2$ is the distance between the stars and G is the gravitational constant.

Let the star with mass m_2 explode as a supernova, forming a neutron star with mass m_3 and ejecting a mass $\Delta m = m_1 - m_3$. In an asymmetrical explosion, the neutron star acquires a recoil velocity $\mathbf{v}_k$. The additional velocity $\mathbf{v}_s$ acquired by the system with mass $m_2 + m_3$ after the explosion is determined by the relation:

$$(m_2 + m_3)\mathbf{v}_s = m_2\mathbf{v}_2 + m_3(\mathbf{v}_1 + \mathbf{v}_k),$$
$$\mathbf{v}_s = \frac{1}{m_2 + m_3}\left[m_3\mathbf{v}_k - \Delta m\mathbf{v}_1\right] =$$
$$\frac{m_3}{m_2 + m_3}\mathbf{v}_k - \frac{\Delta m}{m_1 + m_2}\frac{m_2}{m_2 + m_3}\mathbf{v}$$
$$\mathbf{v}_s = \nu\mathbf{v}_k - (\alpha - \nu)\mathbf{v}, \qquad (3)$$

where $\nu = m_3/(m_2 + m_3)$ and $\alpha = m_1/(m_1 + m_2)$. Further, all velocities will be expressed in units of the relative velocity v; i.e., $\mathbf{u} \equiv \mathbf{v}_s/v$, $\mathbf{u}_k \equiv \mathbf{v}_k/v$, or

$$\mathbf{u} = \nu\mathbf{u}_k - (\alpha - \nu)\mathbf{j}, \qquad (4)$$

where $\mathbf{j}$ is a unit vector along the y axis (see Fig. 1). The z axis is chosen to be normal to the orbital plane of the binary before the explosion. The x axis is chosen so that the stars lie along this axis at the moment of the explosion. After the explosion, a unit vector normal to the orbital plane $\mathbf{n}$ will rotate in the yz plane in accordance with the equation:

$$(\mathbf{v}_2 - \mathbf{v}_s) \times i = A\mathbf{n}, \qquad (5)$$

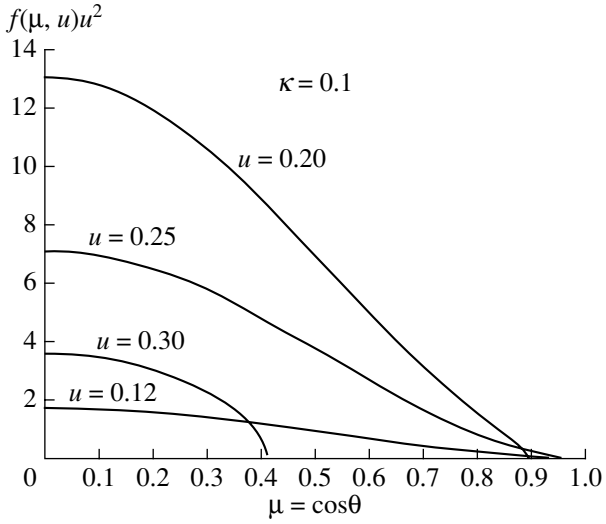

Fig. 2. Plot of the distribution $f(\mu, u)u^2$ for $\kappa = 0.1$.

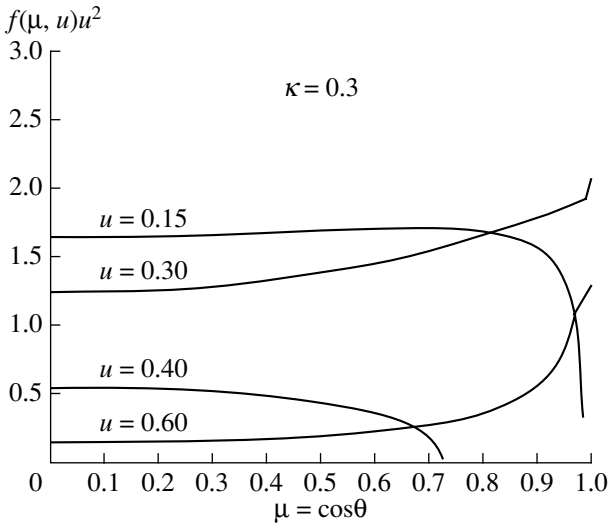

Fig. 3. Plot of the distribution $f(\mu, u)u^2$ for $\kappa = 0.3$.

where $A = |(\mathbf{v}_2 - \mathbf{v}_s) \times \mathbf{i}|$. The solution to this equation is

$$\mathbf{n} = \frac{-\mathbf{j}u_z + \mathbf{k}(\alpha + u_y)}{\sqrt{(\alpha + u_y)^2 + u_z^2}}; \qquad (6)$$

i.e., the cosine of the angle between the vectors $\mathbf{n}$ and $\mathbf{u}$ is

$$\frac{\mathbf{nu}}{u} = \frac{\alpha u_z}{u\sqrt{(\alpha + u_y)^2 + u_z^2}}. \qquad (7)$$

Let us consider only binaries that are not disrupted by the explosion; i.e., those whose total energy in the center-of-mass coordinate frame remains negative after the explosion:

$$-\frac{Gm_2m_3}{r} + \frac{m_{23}}{2}(\mathbf{v}_1 + \mathbf{v}_k - \mathbf{v}_2)^2 < 0, \qquad (8)$$

where $m_{23} = m_2m_3/(m_2 + m_3)$ is the reduced mass. Using (2) and (4), the condition for preserving the binary system (8) can be reduced to the form

$$2\nu^2\frac{1-\alpha}{1-\nu} - \alpha^2 - u^2 - 2\alpha u_y > 0. \qquad (9)$$

(We consider coalescence of the two stars after the explosion to be unlikely.)

Let us construct the distribution $f(\mu, \mathbf{u})$ of the cosines of the angles between the vectors $\mathbf{n}$ and $\mathbf{u}$, $\mu = \mathbf{nu}/u$, and the velocity $\mathbf{u}$. We assume (following [6]) that $\mathbf{u}_k$ is a random quantity with a Maxwellian distribution:

$$\frac{1}{(2\pi\kappa^2)^{3/2}}\exp\left[-\frac{u_{kx}^2 + u_{ky}^2 + u_{kz}^2}{2\kappa^2}\right]. \qquad (10)$$

The dimensionless parameter κ describes the dispersion of the recoil velocities for the neutron star:

$$f(\mu, \mathbf{u}) = \int d\mathbf{u}_k \frac{1}{(2\pi\kappa^2)^{3/2}}\exp\left[-\frac{u_k^2}{2\kappa^2}\right] \qquad (11)$$
$$\times\delta\left[\mu - \frac{\mathbf{nu}}{u}\right]\delta\left[\mathbf{u} - \nu\mathbf{u}_k + (\alpha - \nu)\mathbf{j}\right]$$
$$\times\Theta\left[\frac{2\nu^2(1-\alpha)}{1-\nu} - \alpha^2 - u^2 - 2\alpha u\sin\theta\sin\phi\right].$$

The Heaviside function Θ ensures that we take into account only undisrupted systems.

After integrating $f(\mu, \mathbf{u})$ over the initial orientations of the orbital planes of the binaries before the supernova, this function ceases to depend on the direction of $\mathbf{u}$. To obtain $f(\mu, u)$, we can integrate $f(\mu, \mathbf{u})$ over the directions of the velocity $\mathbf{u}$ for a fixed orientation of the initial binary. Since $f(\mu, u)$ is even with respect to μ, we will use it for $0 \le \mu \le 1$. The integral over the angle θ in the domain $(0, \pi)$ will reduce to twice the integral over the domain $(0, \pi/2)$:

$$f(\mu, u) = 2\int_0^{\pi/2}\sin\theta d\theta\int_0^{2\pi} f(\mu, \mathbf{u})d\phi. \qquad (12)$$

The integral $\int_0^1 d\mu\int_0^\infty f(\mu, u)u^2du$ is equal to the fraction of systems that remain undisrupted after the supernova. When $\kappa \to 0$, this fraction tends to unity.

Taking into account the function $\delta[\mathbf{u} - \nu\mathbf{u}_k(\alpha - \nu)\mathbf{j}]$, we will integrate over $\mathbf{u}_k$ and then over the angle ϕ.

$$\delta\left[\mu - \frac{\mathbf{nu}}{u}\right]$$

$$= \delta\left[\mu - \frac{\alpha\cos\theta}{\sqrt{(\alpha + u\sin\theta\sin\phi)^2 + u^2\cos^2\theta}}\right]$$
$$= \frac{\alpha^2\cos\theta}{\mu^2}\frac{1}{u\sin\theta}\frac{1}{\sqrt{\alpha^2 - u^2\mu^2}}$$
$$\times\left\{\delta(\psi - \psi_0^{(1)}) + \delta(\psi - \psi_0^{(2)})\right\}, \qquad (13)$$
$$\psi \equiv \sin\phi \quad \int d\phi \to \int \frac{d\psi}{\sqrt{1-\psi^2}},$$

$$\psi_0^{(1)} = \frac{1}{u\sin\theta}\left\{\frac{\cos\theta}{\mu}\sqrt{\alpha^2 - u^2\mu^2} - \alpha\right\}, \qquad (14)$$
$$\psi_0^{(2)} = \frac{1}{u\sin\theta}\left\{-\frac{\cos\theta}{\mu}\sqrt{\alpha^2 - u^2\mu^2} - \alpha\right\}.$$

We obtain

$$f(\mu,u) = \frac{1}{(2\pi\nu^2\kappa^2)^{3/2}}\exp\left[-\frac{u^2 + (\alpha-\nu)^2}{2\nu^2\kappa^2}\right]4\frac{\alpha^2}{\mu^2}\frac{1}{u}\frac{1}{\sqrt{\alpha^2 - u^2\mu^2}}\int_0^{\pi/2} d\theta\cos\theta$$
$$\times\left\{\exp\left[-\frac{2(\alpha-\nu)}{2\nu^2\kappa^2}u\sin\theta\psi_0^{(1)}\right]\frac{1}{\sqrt{1-(\psi_0^{(1)})^2}}\Theta\left[2\nu^2\frac{1-\alpha}{1-\nu} - u^2 - \alpha^2 - 2\alpha u\sin\theta\psi_0^{(1)}\right]\right. \qquad (15)$$
$$\left.+\exp\left[-\frac{2(\alpha-\nu)}{2\nu^2\kappa^2}u\sin\theta\psi_0^{(2)}\right]\frac{1}{\sqrt{1-(\psi_0^{(2)})^2}}\Theta\left[2\nu^2\frac{1-\alpha}{1-\nu} - u^2 - \alpha^2 - 2\alpha u\sin\theta\psi_0^{(2)}\right]\right\},$$

$$|\psi_0^{(1)}| < 1, \qquad |\psi_0^{(2)}| < 1.$$

Figures 2 and 3 present the results of numerical integration of (15) for $\kappa = 0.1$ and $\kappa = 0.3$. We can see that, in the case of small recoil velocities ($\kappa = 0.1$), the distribution $f(\mu,u)u^2$ has a maximum at $\mu = 0$ (i.e., the direction of the additional velocity is close to the orbital plane of the binary). For larger recoil velocities ($\kappa = 0.3$), the μ distribution becomes close to isotropic, while for $u > 0.4$, the direction of the additional velocity is close to the normal to the orbital plane. Figure 4 presents the function $f(\mu) = \int_0^\infty f(\mu,u)u^2du$. This relation also indicates that systems that acquire small additional velocities ($\kappa \sim 0.1$) move primarily in their orbital planes, whereas rapidly moving systems ($\kappa \sim 0.5$) move normal to their orbital planes. The areas under the curves are equal to the fraction of undisrupted systems, which decreases as κ increases. The parameters of binaries after an asymmetrical supernova explosion were investigated in [6]; however, the functions $f(\mu,u)$ and $f(\mu)$ were not derived. Using these functions, the orientations of binaries relative to the plane of the Galaxy for various heights above the Galactic plane can be determined. We plan to do this as part of our subsequent work.

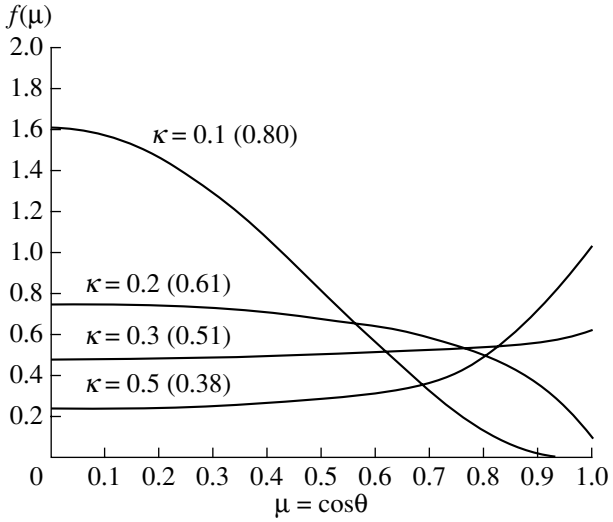

Fig. 4. The function $f(\mu)$ for various κ. For each κ, the fraction of undisrupted systems is indicated in parentheses.

Note that binaries with large orbital periods ($P \sim 120$ days and $v \sim 70$ km/s) cannot be thrown to large heights above the Galactic plane by supernova explosions, since they are either disrupted or have low velocities. The radiative mechanism can accelerate binaries independent of their orbital periods.

It is interesting that the radiative mechanism for acceleration makes it possible for X-ray binaries belonging to a globular cluster to remain inside the cluster. For a globular cluster with mass $10^5 M_\odot$

and radius ~ 3 pc, the radiative force $F_X = 2.6 \times 10^{26}$ dyne does not exceed the gravitational attraction of the binary toward the cluster center.

3. ACKNOWLEDGEMENTS

This work was supported by the Russian Foundation for Basic Research (project no. 98-02-18401), the State Science and Technology Program "Astronomy," and INTAS (Project no. 96-0154).

REFERENCES

1. V. D. Pal'shin and A. I. Tsygan, Pis'ma Astron. Zh. **24**, 163 (1998) [Astron. Lett. **24**, 131 (1998)].
2. J. van Paradijs, in *The Lives of the Neutron Stars,* Ed. by M. A. Alpar, U. Kiziloglu, and J. van Paradijs (Kluwer, Dordrecht, 1993), p. 281.
3. G. S. Bisnovatyi-Kogan and B. V. Komberg, Pis'ma Astron. Zh. **2**, 338 (1976) [Sov. Astron. Lett. **2**, 130 (1976)].
4. G. S. Bisnovatyi-Kogan, in *The Magnetospheric Structure and Emission Mechanisms of Radio Pulsars (IAU Colloquium 128),* Ed. by T. H. Hankins, J. M. Rankin, and J. A. Gil (Pedagogical Univ. Press, 1992), p. 209.
5. E. R. Harrison and E. Tademaru, Astrophys. J. **201**, 447 (1975).
6. V. Kalogera, Astrophys. J. **471**, 352 (1996).

Translated by K. Maslennikov

Astronomy Reports, Vol. 45, No. 12, 2001, pp. 972–983. Translated from Astronomicheskiĭ Zhurnal, Vol. 78, No. 12, 2001, pp. 1104–1115.

Age and Metallicity Estimates for Moderate-Mass Stars in Eclipsing Binaries

D. A. Kovaleva

Institute of Astronomy, Russian Academy of Sciences, Pyatnitskaya ul. 48, Moscow, 109017 Russia

Received February 15, 2001

Abstract—We estimate the ages and metallicities for the components of 43 binary systems using a compilation of accurate observational data on eclipsing binaries for which lines of both components are visible in their spectra, together with two independent modern sets of stellar evolution models computed for a wide range of masses and chemical abundances. The uncertainties of the resulting values are computed, and their stability is demonstrated. The ages and metallicity are compared with those derived in other studies using different methods, as well as with independent estimates from photometric observations and observations of clusters. These comparisons confirm the reliability of our age estimates. The resulting metallicities depend significantly on the choice of theoretical model. Comparison with independent estimates favors the estimates based on the evolutionary tracks of the Geneva group. © *2001 MAIK "Nauka/Interperiodica".*

1. INTRODUCTION

Direct estimation of a star's mass from its observed parameters is possible only in a limited number of cases (when the star is a component of a certain type of binary). The number of such stars is insufficient to solve many astrophysical problems. One widely used technique for mass estimation for large samples of stars, including single stars, is to use relations between comparatively easily determined stellar parameters (for example, magnitude) and a star's mass. Such relations can be derived using the dynamical masses of binary components and independent estimates of observable parameters (empirical relations) or via stellar model computations (theoretical relations). Comparison between empirical and theoretical relations can be an effective means to study models of stellar evolution.

A valuable source of data for empirical relations are eclipsing binaries (EB) in which lines of both components are observed in their spectra (SB2). The light curve and the radial velocity curve provide information on the masses and linear sizes of the components. Estimates of the effective temperatures of the components can be used to derive their bolometric luminosities. Currently, the typical accuracy of mass and radius estimates for such stars is better than 5%. It is difficult to obtain accuracies this good for other types of systems, for which parallax errors make a significant contribution to the uncertainty.

Andersen [1] notes that 5% is the limiting accuracy for mass determinations, so that the scatter of empirical points essentially ceases to decrease after reaching this accuracy. Deviations of individual stars from mean relations are now due not only to observational errors, but also to the dispersions of their chemical abundances and ages. Mass and radius accuracies of 2–3% make it possible to compute these effects and take them into account when comparing empirical and theoretical relations.

In the current study, we estimated the ages and initial chemical abundances (CAs) for the main-sequence components of eclipsing binaries using modern stellar models. This amounts to minimizing a multi-variable parametric function in a limited domain, as was done in [2] to estimate the characteristics of components of unresolved low-mass binaries. This technique makes it possible to distinguish and take into account evolutionary effects for intermediate-mass stars (0.8–7 $m_\odot$), as well as the influence of abundance differences on the scatter of observed parameters. We also analyzed the accuracy and stability of the derived ages and metallicities of the systems. We present comparisons with the estimates published in [3] and with other independent estimates.

In a subsequent paper, the results will be used to study the agreement between the theoretical mass–effective temperature and mass–luminosity relations with observations.

Section 2 formulates the problem and describes the theoretical evolution computations and compilation of observations we used. In Section 3, we discuss the techniques applied. Section 4 analyzes

1063-7729/01/4512-0972$21.00

Table 1. Comparison of general characteristics of the Geneva and Padova models

	Geneva group models	Padova group models
Mass range	0.8–120 $m_\odot$	0.6–120 $m_\odot$
Our mass range	0.8–10 $m_\odot$	0.8–10 $m_\odot$
CAs (Y, Z)	(0.24, 0.001), (0.25, 0.004), (0.26, 0.008), (0.30, 0.02), (0.34, 0.04), (0.48, 0.1)	(0.23, 0.0004), (0.23, 0.001), (0.24, 0.004), (0.25, 0.008), (0.28, 0.02), (0.405, 0.05), (0.42, 0.1)
Our CAs	(0.24, 0.001), (0.25, 0.004), (0.26, 0.008), (0.30, 0.02), (0.34, 0.04)	(0.23, 0.001), (0.24, 0.004), (0.25, 0.008), (0.28, 0.02), (0.405, 0.05), (0.42, 0.1)
Our age range	ZAMS to end of main-sequence evolution	ZAMS to end of main-sequence evolution
Convection parameter	$\alpha = 1.6$	$\alpha = 1.63$
Convective overshooting (CO)	Models with CO + several without CO	Models with CO + several without CO
Opacities	OPAL [16], $z \leq 0.03$; LAOL [17], $z > 0.03$	OPAL [16]
Mass loss $(m/m_\odot)$ yr^{-1}	$(0.6–1.0) \times 10^{-7}$	No mass loss for $m/m_\odot \leq 12$

the accuracy and stability of the results and presents a comparison with independent estimates. Our conclusions are summarized in Section 5.

2. PROBLEM FORMULATION INPUT DATA

There exist several methods to determine the ages and chemical abundances of stars. However, these have limited applicability. Practically none give results that can be considered uniform and are useful for determinations of the characteristics of large and heterogeneous samples of stars.

In our current study, we consider spectroscopic binaries in which lines of both components can be observed in their spectra (SB2-EBs). We estimated their evolutionary status using data on well-determined masses and radii. We decided to use radii (rather than luminosities or temperatures) in our computations, because they can be determined accurately without applying implicit assumptions.

To increase the uniqueness of the solutions and take into account the stars' binarity, we imposed additional conditions flowing from the assumption that a close binary's components have a common origin. We assumed they had equal ages and initial chemical abundances.

For our computations, we selected two modern sets of models computed for a wide range of masses and a variety of abundances covering values characteristic of disk stars: those of the Geneva [4–11] and Padova [12–15] groups. Table 1 compares some characteristics of these tracks.

There exist several representative reviews containing data on the parameters of components of SB2-EB systems [1, 18–20]. The bibliographic "Catalogue of Astrophysical Parameters of Binary Systems" [21] contains all information available at the time of its publication, including data on observed SB2-EB stars. We selected only those systems in which both components are thought to be on the main sequence. The catalog contains the observed masses, radii, effective temperatures, and bolometric luminosities of the binary components (along with their errors). The data from [21] were supplemented and updated in 2000. In this way, we obtained a very complete compilation of modern observational data for a list of SB2-EB stars. We excluded three SB2-EB systems in which the masses of both components were below 0.8 $m_\odot$. Table 2 contains a list of the stars and data used.

Table 2. The sample of SB2-EB systems. Observed component characteristics, ages and metallicities for the Geneva tracks, and values of D^2

Name HD number	Ref.	Sp(A) Sp(B)	m (A)/$m_\odot$ m(B)/$m_\odot$	r(A)/$r_\odot$ r(B)/$r_\odot$	$\log T_{\rm eff}$ (A)(K) $\log T_{\rm eff}$ (B)(K)	$\log L$(A)/$L_\odot$ $\log L$(B)/$L_\odot$	[Fe/H]	$\log t$ (yrs)	D^2
GG Lup		B7V	4.13 ± 0.04	2.38 ± 0.02	4.16 ± 0.03	2.36 ± 0.12	-0.22 ± 0.10	6.93 ± 0.11	0.004
HD 135876		B9V	2.52 ± 0.02	1.73 ± 0.02	4.04 ± 0.05	1.6 ± 0.2			
ζ Phe		B6V	3.93 ± 0.04	2.85 ± 0.02	4.163 ± 0.010	2.51 ± 0.04	-0.41 ± 0.04	7.98 ± 0.02	0.3
HD 6882		B8V	2.55 ± 0.03	1.85 ± 0.02	4.076 ± 0.007	1.79 ± 0.03			
IQ Per	[22]	B8V	3.53 ± 0.06	2.47 ± 0.03	4.100 ± 0.007	2.13 ± 0.03	-0.10 ± 0.08	7.74 ± 0.11	0.05
HD 24909	[22]	A6V	1.72 ± 0.04	1.53 ± 0.02	3.890 ± 0.006	0.88 ± 0.03			
PV Cas	[23]	B9.5V	2.81 ± 0.05	2.30 ± 0.02	4.009 ± 0.010	1.69 ± 0.04	-0.42 ± 0.06	8.32 ± 0.11	0.03
HD 240208	[23]	B9.5V	2.76 ± 0.06	2.26 ± 0.02	4.008 ± 0.010	1.71 ± 0.04			
V451 Oph		B9V	2.78 ± 0.06	2.64 ± 0.03	4.03 ± 0.03	1.93 ± 0.13	-0.23 ± 0.10	8.41 ± 0.05	0.04
HD 170470		A0V	2.36 ± 0.05	2.03 ± 0.03	3.99 ± 0.02	1.53 ± 0.09			
RX Her		B9V	2.75 ± 0.06	2.44 ± 0.10	4.02 ± 0.03	1.79 ± 0.12	-0.3 ± 0.2	8.40 ± 0.05	0.03
HD 170757		A0V	2.33 ± 0.05	1.96 ± 0.10	3.99 ± 0.02	1.48 ± 0.09			
TZ Men		A0V	2.49 ± 0.03	2.02 ± 0.02	4.02 ± 0.02	1.63 ± 0.07	-0.12 ± 0.05	8.15 ± 0.01	0.06
HD 39780		A8V	1.504 ± 0.010	1.43 ± 0.02	3.86 ± 0.02	0.69 ± 0.07			
AR Aur	[24]	B8V	2.48 ± 0.10	1.78 ± 0.04	4.039 ± 0.012	1.61 ± 0.05	-0.3 ± 0.3	7.93 ± 0.04	0.2
HD 34364	[24]	B9V	2.29 ± 0.09	1.82 ± 0.04	4.015 ± 0.013	1.53 ± 0.05			
V1031 Ori		A6V	2.47 ± 0.02	4.32 ± 0.03	3.90 ± 0.03	1.80 ± 0.11	0.22 ± 0.07	8.74 ± 0.11	0.2
HD 38735		A3V	2.29 ± 0.02	2.98 ± 0.06	3.92 ± 0.03	1.60 ± 0.11			
β Aur		A1V	2.36 ± 0.03	2.56 ± 0.05	3.95 ± 0.02	1.59 ± 0.08	-0.34 ± 0.05	8.67 ± 0.03	0.08
HD 40183		A1V	2.27 ± 0.03	2.42 ± 0.05	3.95 ± 0.02	1.54 ± 0.08			
V1647 Sgr		A1V	2.19 ± 0.04	1.83 ± 0.02	3.982 ± 0.014	1.41 ± 0.05	-0.40 ± 0.11	8.5 ± 0.3	0.06
HD 163708		A1V	1.97 ± 0.03	1.67 ± 0.02	3.959 ± 0.014	1.23 ± 0.06			
VV Pyx		A1V	2.10 ± 0.02	2.17 ± 0.02	3.978 ± 0.009	1.54 ± 0.04	-0.26 ± 0.06	8.73 ± 0.06	0.007
HD 71581		A1V	2.10 ± 0.02	2.17 ± 0.02	3.978 ± 0.009	1.54 ± 0.04			
CM Lac		A2V	1.88 ± 0.09	1.59 ± 0.06	3.94 ± 0.02	1.10 ± 0.07	-0.1 ± 0.2	7.5 ± 0.2	0.02
HD 209147		F0V	1.47 ± 0.04	1.42 ± 0.06	3.8 ± 0.2	0.68 ± 0.09			
RS Cha		A8V	1.86 ± 0.02	2.14 ± 0.06	3.906 ± 0.010	1.24 ± 0.05	-0.38 ± 0.06	8.96 ± 0.01	0.9
HD 75747		A8V	1.82 ± 0.02	2.34 ± 0.06	3.886 ± 0.010	1.24 ± 0.05			
V477 Cyg	[25]	A2V	1.79 ± 0.12	1.57 ± 0.05	3.94 ± 0.02	1.08 ± 0.07	-0.1 ± 0.5	7.6 ± 0.3	0.02
HD 190786	[25]	F2V	1.35 ± 0.07	1.27 ± 0.04	3.82 ± 0.02	0.41 ± 0.09			
ZZ Boo		F2V	1.72 ± 0.08	2.22 ± 0.10	3.824 ± 0.007	0.94 ± 0.05	-0.47 ± 0.06	9.04 ± 0.12	0.05
HD 121648		F2V	1.72 ± 0.08	2.22 ± 0.10	3.824 ± 0.007	0.94 ± 0.05			
TX Her		A8V	1.62 ± 0.04	1.58 ± 0.05	3.86 ± 0.01	0.80 ± 0.05	0.1 ± 0.2	8.5 ± 0.2	0.02
HD 156965		F2V	1.45 ± 0.03	1.48 ± 0.05	3.83 ± 0.01	0.60 ± 0.05			
PV Pup		A8V	1.565 ± 0.011	1.54 ± 0.02	3.84 ± 0.02	0.69 ± 0.08	0.22 ± 0.05	7.33 ± 0.04	0.03
HD 62863		A8V	1.554 ± 0.013	1.50 ± 0.02	3.84 ± 0.0	0.67 ± 0.08			
V442 Cyg		F1V	1.56 ± 0.02	2.07 ± 0.03	3.839 ± 0.006	0.94 ± 0.03	-0.43 ± 0.12	9.20 ± 0.08	0.2
HD 334426		F2V	1.41 ± 0.02	1.66 ± 0.03	3.833 ± 0.006	0.72 ± 0.03			
CW Eri		F2V	1.52 ± 0.02	2.11 ± 0.15	3.83 ± 0.01	0.92 ± 0.07	-0.46 ± 0.12	9.24 ± 0.12	0.14
HD 19115		F2V	1.28 ± 0.01	1.48 ± 0.10	3.82 ± 0.01	0.57 ± 0.07			
RZ Cha		F5V	1.52 ± 0.02	2.26 ± 0.02	3.810 ± 0.010	0.90 ± 0.04	0.23 ± 0.10	9.35 ± 0.04	0.15
HD 93486		F5V	1.51 ± 0.03	2.26 ± 0.02	3.810 ± 0.010	0.90 ± 0.04			

Table 2. (Contd.)

Name HD number	Ref.	Sp(A) Sp(B)	m (A)/$m_\odot$ m(B)/$m_\odot$	r(A)/$r_\odot$ r(B)/$r_\odot$	$\log T_{\rm eff}$(A)(K) $\log T_{\rm eff}$(B)(K)	$\log L$(A)/$L_\odot$ $\log L$(B)/$L_\odot$	[Fe/H]	$\log t$ (yrs)	D^2
BW Aqr	[26]	F7V	1.49 ± 0.02	2.06 ± 0.04	3.803 ± 0.007	0.79 ± 0.03	-0.7 ± 0.2	9.3 ± 0.2	0.03
BD -16 6074	[26]	F8V	1.39 ± 0.02	1.79 ± 0.04	3.810 ± 0.007	0.70 ± 0.03			
DM Vir	[27]	F7V	1.454 ± 0.008	1.76 ± 0.02	3.813 ± 0.007	0.70 ± 0.03	-0.34 ± 0.07	9.23 ± 0.08	0.10
HD 123423	[27]	F7V	1.448 ± 0.008	1.76 ± 0.02	3.81 ± 0.02	0.70 ± 0.03			
CD Tau	[28]	F7V	1.44 ± 0.02	1.80 ± 0.02	3.792 ± 0.003	0.63 ± 0.02	0.3 ± 0.2	9.26 ± 0.12	0.3
HD 34335	[28]	F7V	1.37 ± 0.02	1.58 ± 0.02	3.792 ± 0.003	0.52 ± 0.02			
V1143 Cyg		F5V	1.39 ± 0.02	1.35 ± 0.02	3.810 ± 0.007	0.45 ± 0.03	-0.2 ± 0.1	8.5 ± 0.2	0.012
HD 185912		F5V	1.35 ± 0.01	1.32 ± 0.02	3.806 ± 0.007	0.42 ± 0.03			
TV Cet		F2V	1.39 ± 0.05	1.50 ± 0.05	3.820 ± 0.01	0.58 ± 0.05	0.2 ± 0.3	8.8 ± 0.5	0.08
HD 20173		F5V	1.27 ± 0.04	1.26 ± 0.05	3.803 ± 0.007	0.365 ± 0.04			
BS Dra		F5V	1.37 ± 0.03	1.44 ± 0.05	3.808 ± 0.002	0.50 ± 0.03	-0.3 ± 0.1	9.1 ± 0.3	0.04
HD 190020		F5V	1.37 ± 0.03	1.44 ± 0.05	3.808 ± 0.002	0.50 ± 0.03			
HS Hya		F5V	1.34 ± 0.05	1.36 ± 0.14	3.810 ± 0.005	0.46 ± 0.09	0.0 ± 0.3	8.0 ± 0.4	0.03
HD 90242		F5V	1.28 ± 0.05	1.22 ± 0.14	3.803 ± 0.005	0.34 ± 0.10			
BK Peg		F8V	1.27 ± 0.01	1.5 ± 0.2	3.785 ± 0.005	0.43 ± 0.09	-0.4 ± 0.2	9.34 ± 0.11	0.02
BD +25 5003		F8V	1.43 ± 0.02	2.0 ± 0.2	3.780 ± 0.005	0.69 ± 0.09			
UX Men		F8V	1.238 ± 0.006	1.347 ± 0.013	3.792 ± 0.007	0.38 ± 0.03	-0.4 ± 0.3	9.32 ± 0.06	0.006
HD 37513		F8V	1.198 ± 0.007	1.274 ± 0.013	3.789 ± 0.007	0.32 ± 0.03			
VZ Hya		F6V	1.23 ± 0.03	1.35 ± 0.04	3.812 ± 0.007	0.46 ± 0.04	-0.4 ± 0.3	9.3 ± 0.2	0.08
HD 72257		F6V	1.12 ± 0.03	1.12 ± 0.03	3.798 ± 0.007	0.24 ± 0.04			
FL Lyr		F8V	1.22 ± 0.02	1.28 ± 0.03	3.789 ± 0.007	0.32 ± 0.03	-0.6 ± 0.5	9.3 ± 0.2	0.16
HD 179890		G8V	0.960 ± 0.012	0.96 ± 0.03	3.724 ± 0.008	-0.18 ± 0.04			
UV Psc		G5V	1.22 ± 0.08	1.22 ± 0.08	3.755 ± 0.004	0.14 ± 0.02	-0.1 ± 0.4	9.3 ± 0.3	0.6
HD 7700		K2V	0.87 ± 0.03	0.87 ± 0.03	3.700 ± 0.010	-0.33 ± 0.05			
EW Ori		G0V	1.194 ± 0.014	1.141 ± 0.011	3.776 ± 0.007	0.17 ± 0.03	-0.2 ± 0.2	8.21 ± 0.06	0.001
HD 287727		G5V	1.158 ± 0.014	1.090 ± 0.011	3.762 ± 0.007	0.08 ± 0.03			
WZ Oph		F8V	1.12 ± 0.04	1.34 ± 0.03	3.785 ± 0.005	0.35 ± 0.03	-0.3 ± 0.3	9.6 ± 0.4	0.13
HD 154676		F8V	1.12 ± 0.04	1.34 ± 0.03	3.785 ± 0.005	0.35 ± 0.03			
UV Leo	[29]	G2V	1.105 ± 0.012	1.13 ± 0.02	3.768 ± 0.005	0.13 ± 0.02	-0.4 ± 0.2	9.4 ± 0.2	0.05
HD 92109	[29]	G2V	1.105 ± 0.012	1.13 ± 0.02	3.77 ± 0.03	0.13 ± 0.02			
HS Aur		G8V	0.90 ± 0.02	1.00 ± 0.02	3.73 ± 0.03	-0.13 ± 0.03	-0.7 ± 0.4	9.8 ± 0.3	0.05
BD +47 1350		K0V	0.88 ± 0.02	0.87 ± 0.02	3.716 ± 0.006	-0.30 ± 0.03			
V539 Ara	[30]	B3V	6.24 ± 0.07	4.50 ± 0.08	4.260 ± 0.01	3.29 ± 0.05	-0.06 ± 0.04	7.57 ± 0.03	0.09
HD 161783	[30]	B4V	5.31 ± 0.06	3.42 ± 0.08	4.230 ± 0.01	2.95 ± 0.06			
CV Vel		B2.5V	6.10 ± 0.04	4.09 ± 0.04	4.253 ± 0.012	3.19 ± 0.05	-0.09 ± 0.01	7.55 ± 0.02	0.02
HD 77464		B2.5V	6.00 ± 0.04	3.958 ± 0.04	4.250 ± 0.012	3.15 ± 0.05			
AG Per	[30]	B4V	5.4 ± 0.2	3.0 ± 0.2	4.26 ± 0.02	2.95 ± 0.08	-0.02 ± 0.12	6.35 ± 0.05	0.2
HD 25833	[30]	B4V	4.9 ± 0.2	2.6 ± 0.2	4.24 ± 0.02	2.75 ± 0.08			
U Oph	[28]	B5V	4.93 ± 0.05	3.29 ± 0.06	4.23 ± 0.04	2.9 ± 0.2	-0.31 ± 0.08	7.76 ± 0.04	0.04
HD 156247	[28]	B6V	4.56 ± 0.04	3.01 ± 0.05	4.20 ± 0.04	2.7 ± 0.2			
DI Her		B5V	5.19 ± 0.11	2.68 ± 0.05	4.230 ± 0.020	2.73 ± 0.08	-0.2 ± 0.2	6.5 ± 0.4	0.011
HD 175227		B5V	4.53 ± 0.07	2.48 ± 0.05	4.179 ± 0.020	2.46 ± 0.08			
V760 Sco		B5V	4.7 ± 0.2	2.97 ± 0.06	4.228 ± 0.010	2.81 ± 0.02	-0.43 ± 0.04	7.7 ± 0.3	0.5
HD 147683		B5V	4.42 ± 0.14	2.60 ± 0.09	4.213 ± 0.010	2.63 ± 0.02			

* References not given for data from [21].

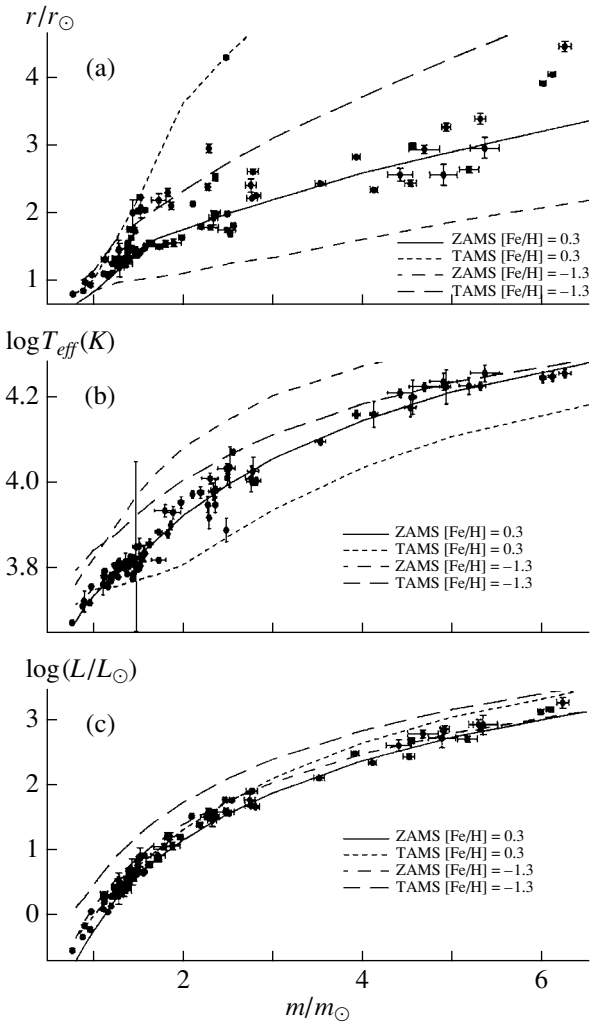

Fig. 1. Distributions of the components of the selected 43 eclipsing binaries in (a) mass–radius, (b) mass–effective temperature, and (c) mass–bolometric luminosity diagrams. For comparison, theoretical relations for the Geneva models are presented for the ZAMS and TAMS for $Z = 0.001$ and $Z = 0.04$, corresponding to the [Fe/H] values indicated in the panels.

Figure 1 displays the observational data from Table 2 in the mass–radius, mass–effective temperature, and mass–luminosity planes. Here and below, we consider the logarithms of the luminosities and effective temperatures. For comparison, we show theoretical relations for the ZAMS (zero age main sequence) and TAMS (terminal age main sequence) for different chemical abundances for the Geneva models: these represent the possible range of physical parameters for stars of the same mass within the main sequences and abundance intervals that are plausible for disk stars. We intentionally presented the mass–radius relation (Fig. 1a) on a linear scale to clearly demonstrate the scatter of the observed data points in comparison with the corresponding errors.

Note that, despite its high accuracy, the compiled stellar data in Tables 2 and 3 are not suitable for statistical studies of the characteristics of binaries or investigations of their mass functions, since they are not statistically complete.

3. COMPUTATION TECHNIQUE

Let $m_1^0 \pm \Delta(m_1^0)$, $r_1^0 \pm \Delta(r_1^0)$, $m_2^0 \pm \Delta(m_2^0)$, and $r_2^0 \pm \Delta(r_2^0)$ be independently determined masses and radii of the binary components, along with their errors. We also assume that we have theoretical stellar models for different chemical abundances.

Theoretical models can be used to compute stellar parameters ($\log L_{bol}/L_\odot$ and $\log T_{eff}$, and hence also r) as functions of the mass m, age $a = \log t$[years], and abundances (X, Y, Z). In the models, $\Delta Y/\Delta Z =$ const; i.e., X, Y, Z were interdependent in the computations (therefore, we can discuss changes of Z, having in mind changes of the overall abundances). For a close binary, it is reasonable to suppose that the components have a common origin and so have the same age and initial chemical abundance.

Thus, we have four initial parameters describing the system: m_1, m_2, a, and Z, where the masses m_1 and m_2 are constrained by the observational errors, the metallicities by the system of evolutionary tracks used, and the system's age by the requirement that both components be main-sequence stars.

We define the function

$$D^2 = \sum_{i=1}^{2}\left(\frac{m_i^0 - m_i}{\Delta(m_i^0)}\right)^2 + \sum_{i=1}^{2}\left(\frac{r_i^0 - r(m_i,a,Z)}{\Delta(r_i^0)}\right)^2, \quad (1)$$

where $r(m_i, a, Z)$ is the radius computed from the theoretical models for a star of the given mass, age, and chemical abundance.

Minimizing D^2, we obtain estimates of a and Z for which (m_1, m_2) and (r_1, r_2) are closest to the observational masses and radii. In this way, we can select an isochrone that is in best agreement with the observed component parameters. The function D^2 is dimensionless, and can used as be an indicator of the goodness of fit between the computed and observed masses and radii for a given system of tracks, given the condition that the components have the same a and Z values. Thus, we must find the minimum of a function of several variables in a limited domain. By approximating the tracks using sets of straight line segments, we can solve this problem analytically using the Nelder–Mead downhill simplex method (the Amoeba procedure, [32]). Instead of the

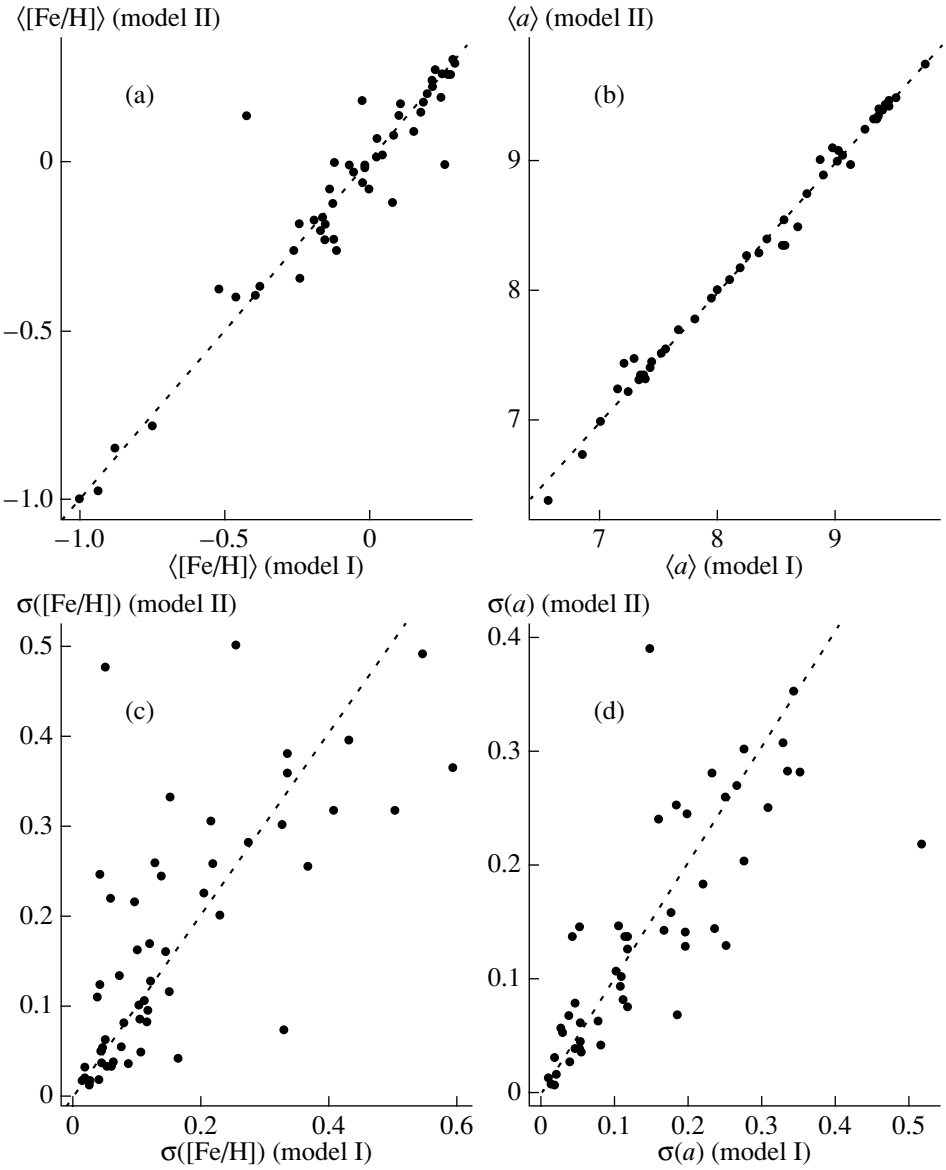

Fig. 2. Comparison of mean (a) metallicity indices, $\langle$[Fe/H]$\rangle$, and (b) ages, $\langle a\rangle = \langle \log t\rangle$, computed using two different models for the component mass and radius errors (model I, uncorrelated errors; model II, correlated errors), together with the standard deviations for the corresponding distributions of the (c) metallicity index, σ([Fe/H]), and (d) age, $\sigma(a)$.

metallicity proper, we will use the metallicity index [Fe/H]$= \log Z/Z_\odot$ unless otherwise stated.

An isochrone as a function of age a and metallicity Z can be obtained by interpolating between tracks in mass and abundance. To ensure trustworthy results, we took into account the shape of the tracks and interpolated only between segments corresponding to equivalent states of evolution. Accurate interpolation consists of two steps. First, tracks are computed for the required mass interpolating in $\log m$ between model tracks for higher and lower masses and model metallicities (provided by the authors of evolutionary computations); we then interpolate in [Fe/H] between these computed tracks. We did not allow extrapolation in our computations.

Note that the minimum of D^2 depends in a complicated way on several parameters (see below), and does not indicate the *accuracy* of the solution. We will call the "optimal" fit for each system the estimate of the age and metallicity providing a minimum of D^2 for the values of m_1^0, m_2^0, r_1^0, and r_2^0 from Table 2.

4. DISCUSSION

After computing the systems' optimal ages and [Fe/H] values, we studied the stability of these results

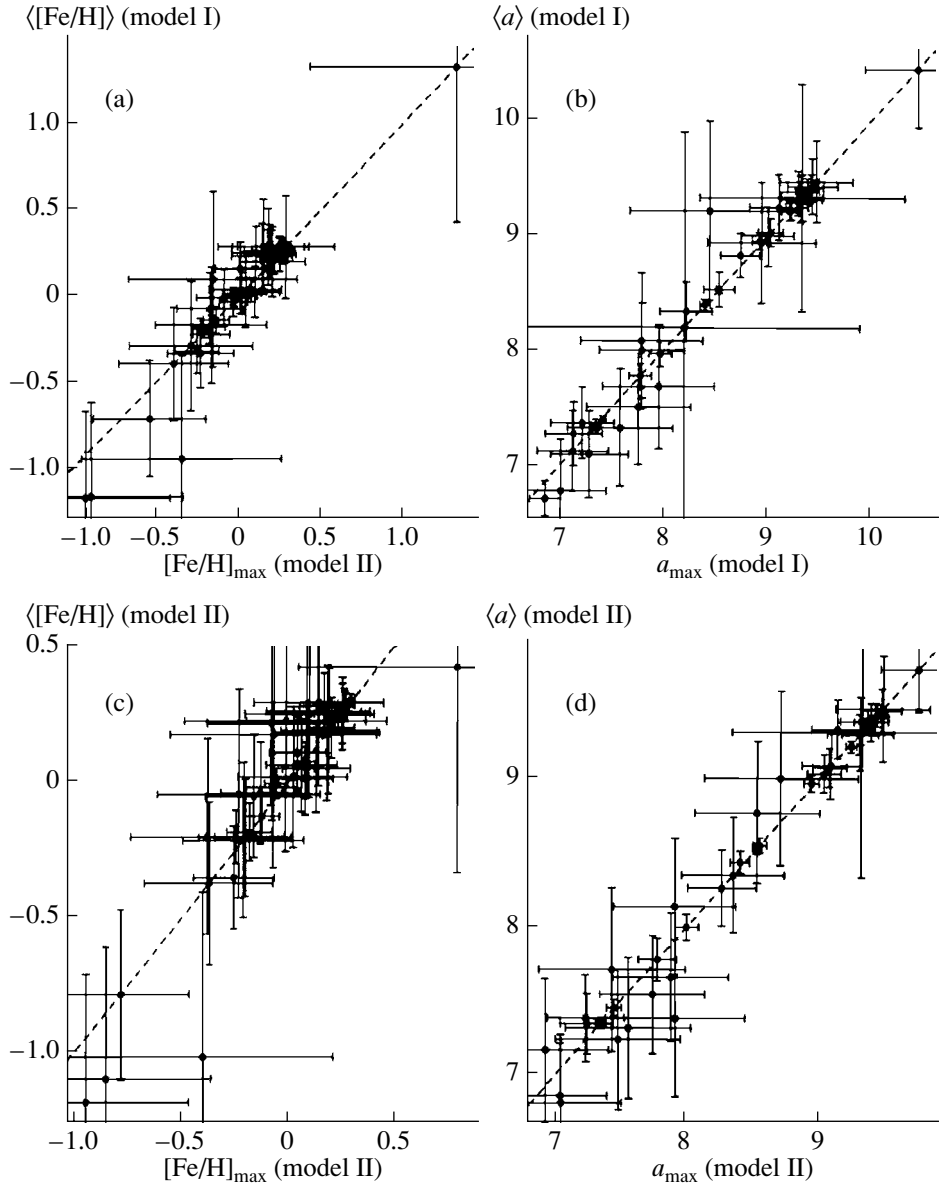

Fig. 3. Comparison of the mean values, $\langle[\mathrm{Fe/H}]\rangle$ and $\langle a\rangle$, and maximum values, $[\mathrm{Fe/H}]_{\max}$ and $a_{\max}$, for the distributions in (a, c) metallicity and (b, d) age derived assuming (a, b) error model I and (c, d) error model II.

to observational errors and estimated their accuracy for given errors.

4.1. Error Estimates for a and [Fe/H]. Stability of the Results

We will treat the mass and radius errors as the standard deviations $\sigma(m_i)$ and $\sigma(r_i)$ of the corresponding normal distributions. The quantities m_1^0, m_2^0, r_1^0, and r_2^0 are not independent, and are interrelated via their errors. Let us consider the distributions of the errors in the component masses $\sigma(m_1^0)$ and $\sigma(m_2^0)$ in more detail.

Let us suppose that observed data points on a radial-velocity curve are normally distributed and independent. We modeled the normal distribution of the observed radial velocity using the observational errors as the standard deviations for each data point. We then constructed orbits from these observations and determine the elements of each of these orbits, the radial velocities of the components, period, and eccentricity, using the ORBIT routine [33]. This enabled us to calculate the component masses to within a factor of $\sin^3 i$. Using the inclinations i from published results on the light curves, we obtained an error distribution for the component masses.

Because it is comparatively resource-intensive,

we carried out such numerical modeling for only six systems randomly selected from the studied sample (Table 2). We found that the error distribution for the component masses could, on average, be considered Gaussian, and the correlation coefficient between the errors $\sigma(m_1)$ and $\sigma(m_2)$ was close to unity for each system. Thus, normal distributions with the mean values m_1^0, m_2^0 and dispersions $\sigma_1^2 = \Delta^2(m_1^0)$, $\sigma_2^2 = \Delta^2(m_2^0)$, and with the correlation coefficient of the dispersions equal to unity can be considered a simple and reasonable model for the component mass errors.

Similar numerical modeling for the component radii, and especially simultaneously for the masses and radii, is a much more complicated task. A priori, it seems reasonable to expect correlation of the errors $\sigma(r_1)$ and $\sigma(r_2)$ of the component radii for a given system, as well as some correlation between the errors in the radii and masses. We preferred not to investigate the particular form of this relation, but instead to study the influence of our choice of model for the errors in the masses and radii on the age and abundance distributions.

We studied the results of age and abundance computations for all 43 binaries based on numerical simulations using two artificial and, in some sense, extreme models for the mass and radius errors for each system. The first model (I) assumes that all four quantities have been determined independently and that their errors are uncorrelated. The second model (II) assumes complete correlation of the errors in the masses and radii. Comparing the resulting a and [Fe/H] values (Fig. 2), we find that the mean values and dispersions of the distributions for each system based on error models I and II are in close agreement and show no systematic displacements from each other. This demonstrates that it is not necessary to try to determine the exact form of the correlation between the errors of the component masses and radii.

The dispersion of the resulting distributions in age and chemical abundance depends on several factors. The most important are the positions of the components relative to the system of tracks considered, the behavior of the tracks in the corresponding region, and the mass and radius errors. The contributions from these factors combine in a complex manner, and it is not possible to derive a simple expression giving a unique relation, for example, between the mass error and the age dispersion.

The resulting distributions in a and [Fe/H] can probably not be considered normal (the hypothesis that they are normal can be rejected at the 5% level according to the χ^2 criterion in more than 90% of cases, for any choice of tracks and error model). Nevertheless, the distributions in age and abundance resemble normal distributions with slight asymmetry in three-quarters of the cases. The mean and maximum of the sample are similar in the vast majority of cases (Fig. 3). However, about a dozen systems show two pronounced maxima in the a–[Fe/H] plane. This is related to two factors:

(1) the limited grid of tracks in metallicity for the linear interpolation (a very sparse grid gave a unique, but systematically biased, solution; an infinitesimal grid increment in [Fe/H] would also lead to a unique result);

(2) the observational errors in the masses and radii (other conditions being the same, higher initial errors lead to non-unique a and [Fe/H]).

The above discussion shows that the standard deviations of the computed distributions, $\sigma(a)$ and σ([Fe/H]), are reasonable indicators of the computational accuracy. For definiteness, we will use the rms deviations of the distributions derived assuming the more realistic model with correlated errors as indicators of the uncertainties.

We find good agreement between the sample mean ages and chemical abundances and the optimal a and [Fe/H] values (Fig. 4). This demonstrates that our results are stable within the limits of the observational errors.

4.2. Comparison of a and [Fe/H] for the Geneva and Padova Tracks

A comparison of the age and abundance estimates derived for the sample of binaries using the two independent track systems shows good agreement for the ages and reasonable agreement for the metallicities, within the estimated uncertainties (Fig. 5). In Fig. 5b, some stars show systematically higher metallicities in the Padova system (where the upper limit of the metallicity range is higher). Table 2 presents the a and [Fe/H] values computed for the Geneva models along with the corresponding values of D^2.

As already mentioned, D^2 does not indicate the errors in a system's parameters, but instead reflects the reliability of the result. Technically, D^2 is the sum of squared distances in the mass–radius plane from the observed positions of the components to the isochrone for some age and metallicity. The minimum of D^2 corresponds to the optimal isochrone parameters a and [Fe/H], whereas the value of D^2 at this minimum indicates how possible it is to find equal ages and abundances for the two components of the system using a given model. This is the quantitative

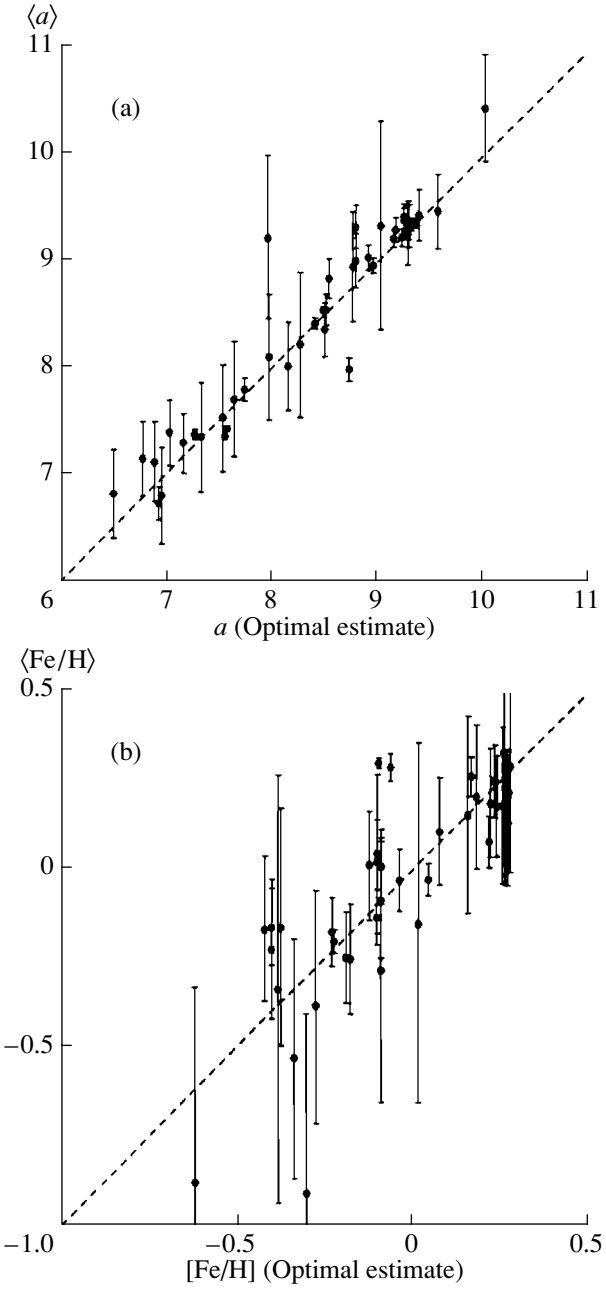

Fig. 4. Comparison of optimal and mean sample values ⟨[Fe/H]⟩ and ⟨a⟩ of the (a) ages and (b) metallicity indices. The rms deviations of the distributions σ([Fe/H]) and $\sigma(a)$ adopted as indicators of the accuracies of the metallicity indices and ages are also shown.

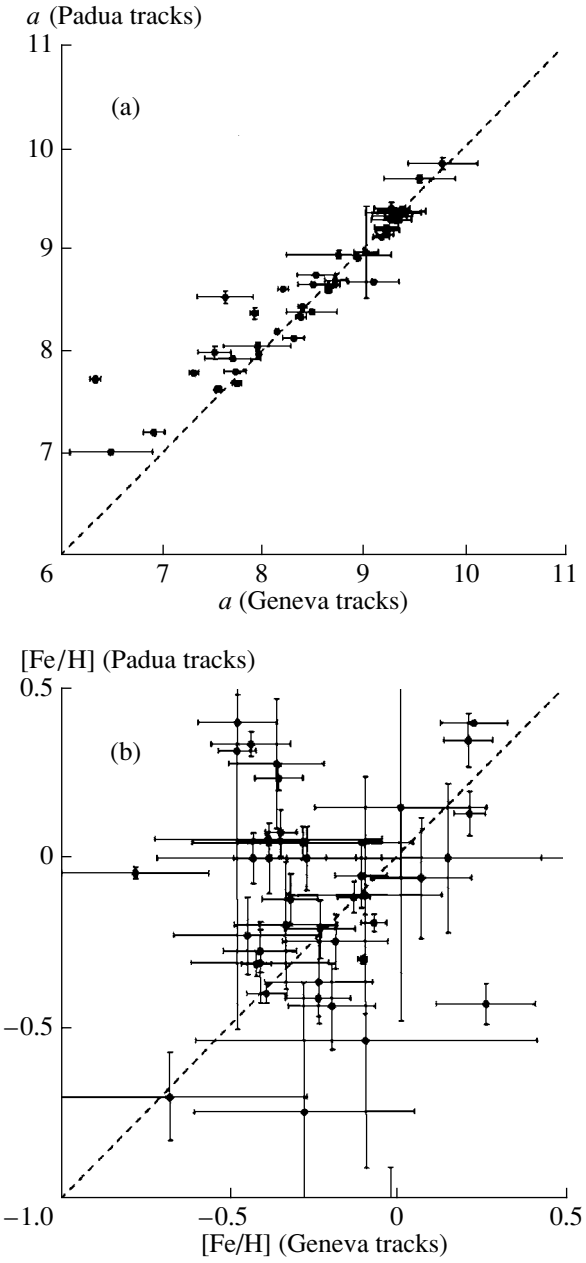

Fig. 5. Comparison of optimal (a) ages and (b) metallicities computed using the Geneva and Padova systems of tracks.

characteristic of the obtained fit that we call the reliability of the result. The accuracy, or uncertainty, indicates how strongly these ages and chemical abundances can change when the component masses and radii are varied within the observational errors.

The minimum of D^2 (Table 2) should be considered only qualitatively: we can say which system has a higher formal reliability for the solution. There is no absolute quantitative criterion to reject any particular results. Arbitrarily, we can call less reliable the 30% of solutions with the highest D^2 values. In this case, the boundary will be approximately at $D^2 = 0.1$.

4.3. Comparison with Results from other Studies

We compared our estimates with the computational results of Pols *et al.* [3] (hereafter PTSEM), derived by comparing their evolutionary tracks with observations for 49 SB2-EB systems. As expected,

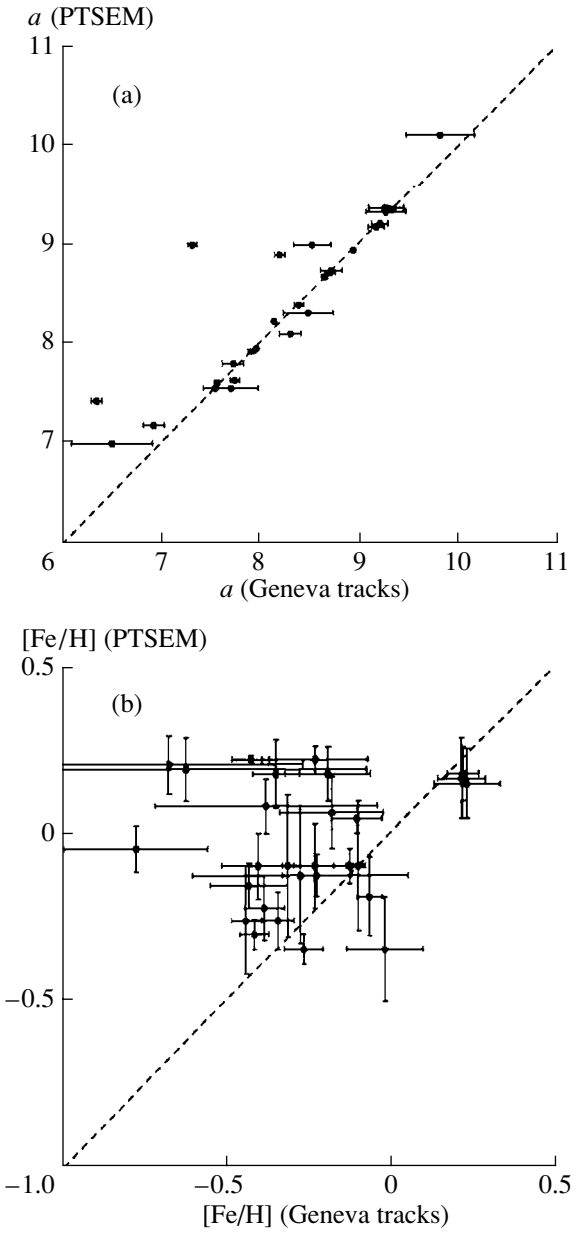

Fig. 6. Comparison of our computed (a) ages and (b) metallicities with independent values from [3].

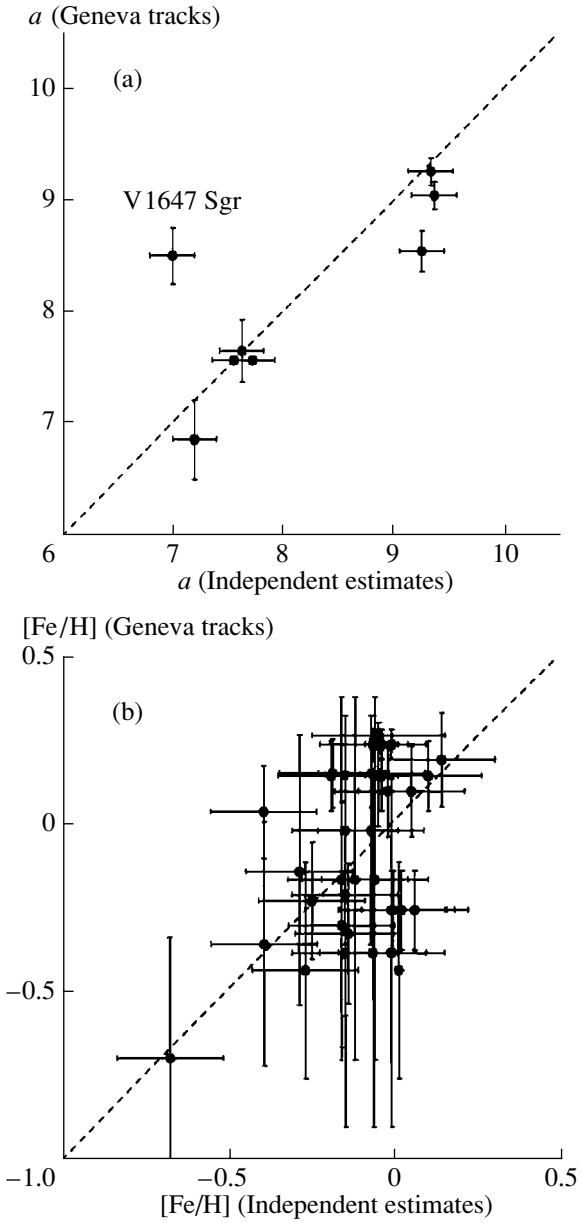

Fig. 7. Comparison of our computed (a) ages and (b) metallicities with independent estimates from photometry and based on membership in stellar aggregates. The system V1647 Sgr is marked in the upper panel; it was associated by us, probably erroneously, with a cluster with an age of 10^7 yr.

the sample of systems in PTSEM overlaps with our sample (although the two samples do not completely coincide due to the different aims of the studies and, consequently, different requirements for the data used). Like us, PTSEM applied the natural hypothesis that the components of a system have equal a and [Fe/H] values. The techniques used differ in that PTSEM used six observed parameters, considering as well the temperatures of the two components.

Comparison of our results with the estimates of PTSEM shows good agreement of the ages and reasonable agreement of the metallicities (Fig. 6). The lower edge of the metallicity range in PTSEM ($Z = 0.01$) is higher than for the models we use, so that [Fe/H](PTSEM) is systematically higher for several systems. The difference in the uncertainties is due to the different techniques used to estimate them. To some extent, the computational reliabilities and unreliabilities are in agreement, since observations for certain systems do not agree with any model if the components are constrained to have equal ages

and chemical abundances. Figures 5 and 6 show that ages below 100 million years computed using the Geneva tracks are systematically lower than both the ages from the Padova tracks and the PTSEM ages.

4.4. Comparison with Independent Estimates of a and [Fe/H]

There are few independent age and chemical-abundance determinations for the systems in our sample. A good source of such information are estimates based on the possible membership of some of the systems in clusters or associations with known parameters. Only four of the systems are usually considered to be related to stellar aggregates [30, 34]. V477 Cyg and V1647 Sgr have been assigned as cluster members based on their coordinates and distance moduli (Fig. 7a). Several ages and metallicities were taken from [35, 36]. Spectroscopic determinations of Z are available for two stars (β Aur and UX Men). For a considerable fraction of the systems with F and G components, $uvby\beta$ intermediate-band photometry is available, making is possible to estimate [Fe/H]. We used the photometric data from [37] and relations from [38], as well as other data of these authors (note, however, that metallicities for binaries determined from integrated photometry are fully correct only if the components are identical, as is not always so in our case).

Figure 7 compares the results of our computations with independent estimates. Our computed a and [Fe/H] values are in reasonable agreement with the independent estimates, given the computed uncertainties. In both panels of Fig. 7, each point corresponds to a single metallicity index or age determination.

These comparisons show that, in contrast to the age estimates, the [Fe/H] estimates depend fairly strongly on the choice of theoretical models used. The best agreement with independent metallicity estimates is found for the Geneva models, whereas the agreement for the Padova models is less satisfactory. The PTSEM tracks occupy an intermediate position.

5. CONCLUSIONS

In this study, we have determined the ages and chemical abundances for components in eclipsing binary systems with reliably known masses and radii using modern stellar models. We selected a compilation of published modern high-accuracy data on the physical characteristics of the components of 43 SB2-EB systems with masses from 0.87 to 6.3 $m_\odot$ and spectral types from K to B (inclusive). In addition, we selected two sets of models published in the last decade, computed for a wide range of masses and chemical abundances covering the values characteristic of disk stars (the computations of the Geneva and Padova groups).

Using these sets of evolutionary tracks and the observed masses and radii for the components, we estimated the component ages and metallicities in a uniform way. We made the natural assumption that the two components in a close binary system have a common origin. To find the a and [Fe/H] values providing a good fit between the modeled and observed characteristics, we determined the minimum of a function of several variables within a limited domain. We consider the resulting age and metallicity-index estimates to be optimal. We demonstrated the stability of these optimal estimates. The standard deviations of a and [Fe/H] were shown to be good estimates of their uncertainties.

When comparing the results for the two systems of evolutionary tracks, the optimal ages agree well and optimal metallicities agree reasonably well. Our results are also in satisfactory agreement with those of Pols *et al.* [3], who used a different computational technique and different set of tracks. The ages of young stars are systematically lower for the Geneva tracks compared to those for the Padova tracks or the results of [3].

Our comparison with independent age and abundance estimates for the program binaries shows agreement between the computed uncertainties and the actual dispersions of the estimates for the same stars. The computed metallicities show a fairly strong dependence on the choice of theoretical model used. The comparison with independent estimates leads us to favor the abundance estimates for the Geneva tracks.

ACKNOWLEDGMENTS

The author expresses sincere thanks to A.E. Piskunov for his continuing help, to O.Yu. Malkov for valuable discussions, to V.I. Myakutin for his assistance during the work with the evolutionary tracks, and to A.A. Pamyatnykh for useful advice. I am grateful to Dr. A. Bressan, who courteously provided evolutionary tracks. I thank the anonymous referee for valuable criticism. This study was supported by grants from the program "Support to Young Scientists" of the Russian Academy of Sciences, the President of the Russian Federation (project no. 99-15-96022), and the Russian Foundation for Basic Research (project no. 00-15-96722).

REFERENCES

1. J. Andersen, Astron. Astrophys. Rev. **3**, 91 (1991).
2. D. A. Kovaleva and O. Yu. Malkov, Astron. Zh. **76**, 100 (1999) [Astron. Rep. **43**, 80 (1999)].
3. O. R. Pols, C. A. Tout, K. P. Shröder, *et al.,* Mon. Not. R. Astron. Soc. **289**, 869 (1997).
4. G. Schaller, D. Schaerer, G. Meynet, and A. Maeder, Astron. Astrophys., Suppl. Ser. **96**, 269 (1992).
5. G. Shaerer, G. Meynet, A. Maeder, and D. Shaller, Astron. Astrophys., Suppl. Ser. **98**, 523 (1993).
6. C. Charbonnel, G. Meynet, A. Maeder, *et al.,* Astron. Astrophys., Suppl. Ser. **101**, 415 (1993).
7. G. Shaerer, C. Charbonnel, G. Meynet, *et al.,* Astron. Astrophys., Suppl. Ser. **102**, 339 (1993).
8. G. Meynet, A. Maeder, D. Shaller, *et al.,* Astron. Astrophys., Suppl. Ser. **103**, 97 (1994).
9. C. Charbonnel, G. Meynet, A. Maeder, and G. Shaerer, Astron. Astrophys., Suppl. Ser. **115**, 339 (1996).
10. N. Mowlavi *et al.,* Astron. Astrophys., Suppl. Ser. **128**, 471 (1998).
11. C. Charbonnel *et al.,* Astron. Astrophys., Suppl. Ser. **135**, 405 (1999).
12. A. Bressan, F. Fagotto, G. Bertelli, and C. Chiosi, Astron. Astrophys., Suppl. Ser. **100**, 647 (1993).
13. F. Fagotto, A. Bressan, G. Bertelli, and C. Chiosi, Astron. Astrophys., Suppl. Ser. **104**, 365 (1994).
14. F. Fagotto, A. Bressan, G. Bertelli, and C. Chiosi, Astron. Astrophys., Suppl. Ser. **105**, 29 (1994).
15. F. Fagotto, A. Bressan, G. Bertelli, and C. Chiosi, Astron. Astrophys., Suppl. Ser. **105**, 39 (1994).
16. C. A. Iglesias, F. J. Rogers, and B. G. Wilson, Astrophys. J. **397**, 717 (1992).
17. W. F. Huebner, A. L. Merts, N. H. Magee, and M. F. Argo, LA-6760-M (1997).
18. D. M. Popper, Ann. Rev. Astron. Astrophys. **18**, 115 (1980).
19. D. M. Popper, Astrophys. J. Lett. **404**, L67 (1993).
20. J. Andersen, in *Fundamental Stellar Properties: The Interaction between Observation and Theory (IAU Symposium 189),* Ed. by T. R. Bedding, A. J. Booth, and J. Davis (Kluwer, Dordrecht, 1997), p. 99.
21. O. Yu. Malkov, Bull. Inf. Cent. Données Stellaires **42**, 27 (1993).
22. O. L. Degirmengi, Astrophys. Space Sci. **253**, 237 (1997).
23. M. J. Barembaum and P. B. Etzel, Astron. J. **109**, 2680 (1995).
24. B. Nordstrom and K. T. Johansen, Astron. Astrophys. **282**, 787 (1994).
25. A. Gimenez and J. M. Quintana, Astron. Astrophys. **260**, 227 (1992).
26. J. V. Clausen, Astron. Astrophys. **246**, 397 (1991).
27. D. W. Latham *et al.,* Astron. Astrophys. **314**, 864 (1996).
28. D. E. Holmgren, G. Hill, and W. Fisher, Astron. Astrophys. **248**, 129 (1991).
29. D. M. Popper, Astron. J. **114**, 1195 (1997).
30. A. Gimenez and J. V. Clausen, Astron. Astrophys. **291**, 795 (1994).
31. I. Ribas, C. Jordi, and J. Torra, Mon. Not. R. Astron. Soc. **309**, 199 (1999).
32. W. H. Press *et al., Numerical Recipes: The Art of Scientific Computing* (Cambridge Univ. Press, Cambridge, 1986).
33. A. Tokovinin, in *Complementary Approaches to Double and Multiple Stars Research (IAU Colloquium 135),* Astron. Soc. Pac. Conf. Ser. **32**, 573 (1992).
34. *General Catalogue of Variable Stars,* Ed. by N. N. Samus' [in Russian] (Nauka, Moscow, 1990).
35. V. A. Marsakov and Yu. G. Shevelev, Bull. Inf. Cent. Données Stellaires **47**, 13 (1995).
36. A. V. Loktin and N. V. Matkin, Astron. Astrophys. Trans. **4**, 153 (1994).
37. B. Hauck and M. Mermilliod, Astron. Astrophys., Suppl. Ser. **129**, 431 (1998).
38. W. J. Schuster and P. E. Nissen, Astron. Astrophys. **221**, 65 (1989).

Translated by N. Samus'

Astronomy Reports, Vol. 45, No. 12, 2001, pp. 984–994. Translated from Astronomicheskiĭ Zhurnal, Vol. 78, No. 12, 2001, pp. 1116–1126.

Algorithms for Data Analysis in Gravitational-Wave Experiments

V. N. Rudenko

Sternberg Astronomical Institute, Universitetskiĭ pr. 13, Moscow, 119899 Russia

Received March 14, 2001

Abstract—The detection of gravitational radiation from relativistic objects in the Universe is discussed. Modern programs designed to search for such signals based on current astrophysical concepts about the nature of the sources are considered. A comparative analysis indicates that available gravitational-wave detectors, whose sensitivity to metric perturbations is on the order of 10^{-21}, are unlikely to be able to detect cosmic gravitational waves. However, the detector sensitivity can be increased using a multichannel method to search for astro–gravitational correlations, in which the noise background of the gravitational-wave detectors is analyzed in parallel with data from neutrino and gamma-ray detectors.

1. INTRODUCTION

It is evident that the detection of gravitational waves is one of the most difficult problems of modern astrophysics, which has remained unsolved after 30 years of gravitational-wave experiments. The existence of gravitational radiation, theoretically predicted by Einstein in 1916 [1], has been confirmed only indirectly by observations of the decrease in the orbital period of the binary pulsar PSR 1913+16 [2]. After the first direct, apparently successful, experiments conducted by Weber at the end of the 1960s [3], all subsequent attempts to detect gravitational waves using better equipment failed. Current optimistic hopes are provided by the development of a new generation of gravitational-wave detectors: supercryogenic, resonant, solid-body antennas cooled to several mK and long-baseline interferometers with free mirrors serving as test masses. We can expect the detection of metric perturbations of the order of 10^{-21}, even in early versions of these facilities.

It was realized from the very beginning of gravitational-wave experiments that only certain superdense stars (or other objects) could produce short bursts of gravitational radiation with sufficient power to be detected. For example, the work of Braginskiĭ *et al.* [4], stimulated by Zel'dovich over 30 years ago immediately after the first works by Weber, listed all typical pulsed sources of astrophysical catastrophes—coalescences of relativistic binaries, supernova explosions, asymmetric collapses—and presented the first rough estimates of the gravitational-wave energy from the center of the Galaxy expected at the Earth. The optimistic estimate for the burst amplitude in units of the metric perturbations obtained in that paper was $h \sim 10^{-18}$. Unfortunately, subsequent studies of the stochastic nature of gravitational-wave signals arriving at the Earth from space led to the more accurate value $h \leq 10^{-21}$ for the expected rate of several events per year. It is important to emphasize that the most recent estimates of the event rate are based on the observed distribution of galaxies within 30–50 Mpc of the Earth derived from [5]. The most reliable astrophysical predictions lead us to expect a reasonable number of events—several bursts per month—only at levels of 10^{-22} in metric perturbation units. This is six orders of magnitude below the accuracy of the first Weber detectors. The present article analyzes the scientific programs to be carried out by the new generation of gravitational-wave antennas.

2. THE WORLDWIDE NETWORK OF GRAVITATIONAL ANTENNAS

The modern generation of resonant antennas includes cryogenic ($T = 4$–2 K) and supercryogenic ($T = 0.1$–0.01 K) facilities. In both cases, a cooled bar is suspended by a wire loop in the zone of its central circle. The standard parameters are mass $m \approx 2 \times 10^3$ kg, length $L \approx 3 \times 10^2$ cm, and mechanical (acoustic) quality factor $Q \sim 10^7$ s, with the central frequency $f \sim 890 - 930$ Hz. The potential sensitivity is determined by the thermal Brownian noise of the mode, whose intensity depends on the combination of key parameters T/mQ (for more details, see [6]); the corresponding thermal standard (mean-square amplitude) is on the order of 10^{-16}. The sensitivity to a continuous quasi-monochromatic signal with a spectral bandwidth 10^{-5} Hz is $h \sim 10^{-21}$ for such cryogenic facilities as EXPLORER (Geneva, CERN) [7], ALLEGRO (Baton Rouge,

1063-7729/01/4512-0984$21.00

LSU) [8], and NIOBE (Perth, AWU) [9]. The pulse sensitivity, which determines the possibility of detecting short signals with durations 10^{-2}–10^{-3} s, will be $h_{bst} \sim 10^{-18}$ for these same antennas.

Super-cryogenic facilities—NAUTILUS (Frascati, INFN) [10] and AURIGA (Legnaro, INFN) [11]—possess sensitivities $h \sim 10^{-22}$ for a quasi-monochromatic signal and $h_{bst} \sim 10^{-19}$ for pulses. The noise spectrum of the deformations (metric perturbations) of a resonant antenna has the typical shape for the form factor for two coupled oscillators (a bar–reading diaphragm pair); the region of maximum sensitivity, which is limited by the detection noise, is located approximately between two eigenfrequencies with bandwidth $\sim$ 20–30 Hz. In principle, suppression of the detection noise (improvement of the quality of the electromechanical transformation) can increase this band without limit.

The second type of gravitational-wave detector—free-mass interferometers—should have substantially wider bands. Their development was strongly stimulated by the linear increase in the response to gravitational waves with the increase in the distance between the test masses. At kilohertz frequencies, this behavior acts up to lengths of $\lambda_g/2 \sim 150$ km, which are extremely large (λ_g is the gravitational-wave length). In practice, interferometers have moderate sizes (3–4 km) with multiple reflections (repeated passages of the optical beam), which is equivalent to increasing the arm length by a factor of 50–100. Modern interferometers have a Michelson configuration with optical Fabry–Perot resonators at each arm (for more details, see [12]).

The spectral intensity of the interferometer noise has a U shape. Quantum photon noise dominates in the central relatively flat part with operating bandwidth $\sim$ 100–1000 Hz. The noise in the left low-frequency wing increases due to thermal and seismic perturbations of the suspended test mass–mirrors, and the sensitivity in the right wing decreases due to the decrease in the interferometer response (i.e., transfer function) to high-frequency gravitational weaves (or, in other words, due to inertial damping of fast perturbations). Exact numerical characteristics of such curves have not yet been completely determined, since all well-known interferometers are still under construction, in particular, the TAMA-300 (Tokyo) [13] and GEO-600 (Hannover) [14] medium-size interferometers and the VIRGO (3 km) (Pisa) [15] and LIGO (4 km) (Hanford and Livingston) [16] large interferometers. In the first stage, the projected characteristics of these facilities should enable the detection of gravitational-wave signals with amplitudes 10^{-21} in a band of $\sim 10^2$ Hz for the medium-size interferometers and in a band of $\sim 10^3$ Hz for the large ones. Later, it is planned to improve the sensitivities of these facilities to 10^{-22} and 10^{-23}. Unfortunately, the required technology is currently incompletely developed. The best experimental result has been demonstrated by the TAMA-300 interferometer: 2×10^{-20} in the frequency band 800–1000 Hz [17].

The picture of the worldwide network of gravitational antennas described above suggests that observational data from both types of detectors at sensitivity levels of about 10^{-21} will be accumulated within the next two or three years. The corresponding spectral density of the deformations will be $h \approx 2 \times 10^{-22}$ Hz$^{-1/2}$ for the solid-body antennas and 3×10^{-23} Hz$^{-1/2}$ for the interferometers. Further improvement is very difficult, and requires the solution of both technical and fundamental problems associated with techniques for performing measurements at the level of quantum sensitivity limits [18–20].

3. COINCIDENCE SEARCHES

Several runs of observations by cryogenic antennas [22–24] have already been carried out in a classical coincidence-search regime [21]; i.e., searching for simultaneous excitation above a specified detection level at multiple detectors. Unfortunately, without using additional (*a priori*) information to identify the bursts, this method is efficient only at large signal-to-noise ratios. For example, the average number of chance excesses over the 3σ threshold for a purely Gaussian process is $\sim$ 2900 events per day. As a result, the average number of expected coincidences between two detectors in a 1 Hz window should be $\sim$190 per day. This background of chance coincidences is too high to enable reliable detection of signals with rates as low as ten events per year, demonstrating the need to implement higher detection thresholds. The coincidence method becomes more efficient if *a priori* information is used to introduce some selection rules for preliminary filtration of signal-like events from arbitrary background bursts [25].

The following observational coincidence results have been reported by the cryogenic groups (IGEC collaboration, see **http://igec.lnl.infn.it/igec** for more details) up to the present time. The probability of a chance event is 10^{-4} for an observation interval of $\sim 10^6$ s in the case of triple coincidences (AL–EX–NA) with a threshold of 3×10^{-18}; the probability of chance coincidences decreases to $\sim 10^{-6}$ if four detectors are used (namely, those listed above plus AU), but the corresponding observation interval is not representative, since it covers only several hours. In other words, the cryogenic antennas see

no gravitational-wave signals from objects close to our Galaxy, but the probability of missing signals in such observations is not small, due to the appreciable spatial selectivity of the joint beam of the compound antenna, the unknown shapes of the expected bursts, non-optimal filtration procedures, etc. On the other hand, isotropic gravitational-wave antennas with deep cooling (so-called ball detectors) will be able to considerably decrease the probability of missing events if these projects will be funded (see, for example, Grail project [26]). As regards algorithms for the preliminary selection of observed bursts for subsequent coincidence searches, a number of quasi-optimal procedures for cleaning a sample by applying minimal assumptions about the structure of the gravitational signal have already been developed [25, 27, 28].

The serious problem of estimating the reliability of coincidence detections and gravitational-signal identifications is associated with the fact that the noise in gravitational detectors is in reality non-Gaussian [31, 32]. Unfortunately, most available methods for gravitational-wave searches were developed precisely for the case of Gaussian background detector noise.

4. COALESCENCE OF RELATIVISTIC BINARY STARS

The detection of gravitational-wave radiation from neutron star–neutron star and black hole–black hole systems, as well as from mixed binaries, at the end of their lives during their coalescence is usually considered to be among the most promising program for interferometric antennas, which are wide-band receivers. Such programs are also appropriate for bar detectors, although the probability of missing signals increases slightly.

The gravitational-wave signal produced by the coalescence of a relativistic binary in the stage of its evolution when the stars spiral together can be accurately calculated. This signal forms a pulse with a rapidly varying carrier frequency, usually referred to as a chirp signal. Theoretically, the well-known binary pulsar PSR 1913–16, which has neutron-star components, should emit weak, monochromatic gravitational waves at a frequency of $\sim 10^{-4}$ Hz over $\sim 10^8$ yr. Further, passing through the frequency interval 10–10^3 Hz over a time of ~ 3 s, it should produce a wave packet composed of 16 000 complete oscillatory cycles. The amplitude of the corresponding gravitational-wave radiation should increase proportional to $(t_0 - t)^{-1/4}$ as the coalescence time t_0 is approached.

Estimates of the average number of events depend on the probability of such events in a single galaxy. There are two very different approaches to estimating coalescence rates. The first, which is empirical and is based on the limited statistics for observed binary pulsars occupying a known restricted region of the Galaxy (three objects), results in the pessimistic value of 10^{-6} per galaxy [33]. The second estimation technique, based on Monte Carlo computer simulations of galaxy evolution, yields the more optimistic value of 10^{-4} per galaxy [34]. The corresponding total numbers of events for neutron-star binaries are $r_e \sim 3$ yr^{-1} for a threshold of $h \sim 10^{-22}$ ($R \sim$ 100–200 M) for the pessimistic estimate and $h \sim 10^{-21}$ ($R \sim 30\ M$) for the optimistic estimate. Taking black-hole binaries into account increases the expected event rate by a factor of three to five, since they increase the total mass of the binary and, as a result, the maximum distance to the source [35].

Therefore, the detection of gravitational radiation from the spiraling-in phase in coalescences of relativistic binaries (searches for chirp signals) is essentially a problem of identifying stochastic bursts with predefined structure at small signal-to-noise ratios (SNR), with *a priori* estimates of the average event rate. Analysis of possible solutions to this problem leads to a joint, multichannel data-processing algorithm, which can be briefly described as follows.

In linear filtration theory, the optimal variable I formed by a resolving device is proportional to the correlation integral

$$I \approx \int_0^t O_D(t,\mu,\lambda)U(t,\mu,\lambda)dt, \qquad (1)$$

where O_D is the receiver output and $U(t)$ is the characteristic shape, or template, of the signal. The signal-to-noise ratio ρ at the correlator output in the case of colored background noise $n(t)$ in a given frequency range can be calculated via the corresponding Fourier transforms:

$$\rho = \frac{S}{N} =\sim Re \int_0^\infty \frac{\tilde{O_D}(f,\mu,\lambda)\tilde{U}(f,\mu,\lambda)}{\tilde{N}(f)}df. \quad (2)$$

The detection criterion is given by the standard condition $\rho > \rho_\alpha$, where α is the probability of false detection and the threshold ρ_α corresponds to the $1 - \alpha$ confidence level. The template of the chirp signal for the spiraling-in stage (i.e., just before coalescence) can be derived from approximate solutions of the complete relativistic problem of binary coalescence with increasing accuracy: a Newtonian approximation, first post-Newtonian approximation, second post-Newtonian approximation, etc. A common feature of all these solutions is their dependence on unknown parameters—both external μ and internal λ—as was already taken into account in (1) and

(2). The shape of the chirp signal in a given frequency region can be written (for more details, see [36, 37])

$$\tilde{U}(f,\mu,\lambda) \sim f^{-7/6}\exp i[-(2\pi f_0+\phi_0)+\Psi(f,\lambda)], \quad (3)$$

where the arrival time t_{st} and initial phase ϕ_0 of the signal are treated as external parameters, and λ represents a set of internal parameters characterizing the binary. In the simplest case of a first post-Newtonian approximation, the only internal parameters are the total mass (m_1+m_2) and the mass ratio $m_1m_2/(m_1+m_2)^2$ [36]. Formula (3) represents a rapidly oscillating function. Note that the integral (1)–(2) is more sensitive to the phase correction $\Psi(f,\lambda)$ than to the amplitude coefficient. For this reason, most efforts have been concentrated on improving calculation of $\Psi(f,\lambda)$ [38].

In the absence of *a priori* information about the chirp parameters, the only possibility is multichannel detection—when an operator uses all possible templates and distinguishes those yielding a maximum signal-to-noise ratio [see (1)]. It is clear that such a procedure requires the use of some kind of optimal steps in the parameter space (or some effective distance between two successive templates). The optimization is based on the following compromise between the detection characteristics: (i) the loss in signal-to-noise ratio ρ if less-accurate (more sparse) templates are used, which corresponds to a decrease in the average number of expected events r_e, and (ii) the increase in the required computational power P_r if the number of processed channels increases.

If the burst amplitude is $h \sim R^{-1}$, then the average number of expected events should be $r_e \sim R^3 \sim \rho^{-3}$. Therefore, the relative loss in r_e is

$$\delta r_e = (\rho_\Delta/\rho_0)^3, \quad (4)$$

where ρ_0 is the maximum SNR, corresponding to the best coincidence between the template and signal, and ρ_Δ is the decrease in the SNR due to some deviation of the parameters $\Delta\lambda_j$ (we consider here only internal parameters, since the external parameters can be estimated via a simple computer variation). The maximum admissible discrepancy ρ_Δ is calculated in accordance with (2), where the receiver output function is specified as a shifted template at $\lambda_j+\Delta\lambda_j$ and a shift step corresponds to the median point between neighboring templates on the parameter grid, $|\Delta\lambda_j| = l/2$. From a geometrical point of view, the maximum discrepancy in an n-dimensional parameter space corresponds to a decrease in the SNR of $\rho_\Delta = 1-n(l/2)^2$. Further, expanding ρ_Δ in the neighborhood of the point $\Delta\lambda_j = 0$, we can introduce the metric g_{ij} in the parameter space:

$$\rho_\Delta \approx 1 - \frac{1}{2}\frac{\partial^2\rho_\Delta}{\partial\lambda_i\partial\lambda_j|_{\Delta\lambda=0}}\Delta\lambda_i\Delta\lambda_j \quad (5)$$

$$= 1 + g_{ij}\Delta\lambda_i\Delta\lambda_j.$$

The metric g_{ij} is a function of the grid scale l and can be found from the condition of maximum discrepancy:

$$g_{ij}\Delta\lambda^i\Delta\lambda^j = n(l/2)^2. \quad (6)$$

Therefore, the procedure for determining the optimum template grid in the parameter space reduces to (i) calculating ρ_Δ in accordance with an admissible decrease in the average number of expected events r_e [see (4)], (ii) determining the size of an elementary cell l [see (5) and (7)], and (iii) calculating the total number of required templates:

$$N = \frac{\int d^n\lambda\sqrt{det||g_{ij}||}}{(2\sqrt{(1-\rho_\Delta)/n})^n}. \quad (7)$$

When an optimum array of templates is found, we can estimate the computational power required for immediate (real-time) processing of the data transmitted from the detector. It is obvious that this estimate will also depend on the chosen range of parameter values. For example, for the first (initial) version of LIGO-I, formulas from [36, 37] give the following estimates for the required total number of templates N and the computational power P (number of floating-point operations per second):

$$N \sim 2\times10^5(0.1/r_e)(0.2M_\odot/m_{\min})^{2.7}, \quad (8)$$
$$P \sim 3\times10^{10}(0.1/r_e)(0.2M_\odot/m_{\min})^{2.7}.$$

If $r_e = 0.1$ and $m_{\min} = 0.2M_\odot$, then the required computational power turns out to be quite high: $P \sim 10^{11}$ flops (floating-point operations per second). Moreover, it will become even greater, of the order of 1 Tflops, for LIGO-II and VIRGO. Such computational requirements are not acceptable. In this situation, it is reasonable to develop some step-by-step hierarchical procedures that can economize computational resources. For example, a two-stage procedure is discussed in [37, 39]: the data are initially filtered on a sparse template grid with a low detection threshold, after which the data sets for which the threshold was exceeded are processed on a more accurate (dense) grid with a higher threshold. It is important to emphasize that, in any case, a 0.95 confidence detection level is achieved for amplitudes h that exceed the potential sensitivities of available antennas (or those under construction) $h_{\min}$ by factors of five to seven.

The algorithms described above refer to attempts to detect the coalescence of a relativistic binary in the first (spiraling-in) stage. We do not know the corresponding signal template for the stage of direct coalescence (contact between the components), necessitating numerical solutions of the relativistic problem of a collision between black holes. Nevertheless, a cruder procedure based on *a priori* estimates for a frequency band Δf and a duration T

for the expected burst can be applied here. Such estimates are derived, for example, from conservation laws, assuming that a Kerr black hole is formed as the final product of the coalescence [29]. In this case, the band-pass filtration is based on the Kotel'nikov theorem, which states that it is possible to obtain a discrete representation of a function with a bounded spectrum $\Delta f \sim f_{\max}$. In addition, if the signal duration is limited, the set of required discrete readouts with step $1/f_{\max}$ becomes finite and forms the so-called signal basis $N = 2f_{\max}T$. The optimum variable [similar to (1)] formed by the fast Fourier transform of the output data from the gravitational antenna is the sum of the squares of the corresponding independent frequency components, proportional to the power of the total signal-plus-noise oscillation (with noise bleaching; i.e., normalizing to its spectral intensity). In the case of a Gaussian background, the statistics of this variable obey a χ^2 distribution, so that the corresponding thresholds and detection errors can be calculated explicitly [28]. As was shown in [30], this method gives results similar to those for matched filtering with a specified template (0.6–0.7 relative to the signal-to-noise ratio) for moderate values of the signal base $N \sim 1$–100, typical of the direct coalescence stage and the final stage of ringing—damped oscillations of the resulting Kerr object. On the other hand, it is evident that there remains a need for comprehensive searches for admissible values of T and Δf as functions of the parameters of a black-hole binary (multichannel reception) as a typical strategy for blind searching. Since the time of signal arrival t_{st} is unknown, the increasing computation volume and the requirements for computational power lead to the same type of step-by-step, hierarchical processing procedure as in the case of chirp signals [30].

5. PERIODIC SOURCES

The aim of this program is to search for gravitational-wave radiation from pulsars. Astrophysical analyses of galaxy evolution estimate the fraction of neutron stars in the total population of a galaxy to be 0.01–0.001%, or 10^9–10^8 neutron stars per galaxy [40]. Unfortunately, the number of neutron stars that can be pulsars is quite uncertain. About 1000 pulsars have been observed in our own Galaxy, but only $\sim$ 30 of these possess frequencies in the range 100–1000 Hz.

A pulsar can be a source of continuous and almost monochromatic gravitational-wave radiation at the double frequency of its proper rotation f_0 if there is some non-axial rotational asymmetry in the mass distribution $\varepsilon = (I_{xx} - I_{yy})/I_{zz}$ (where I_{kk} is the moment of inertia about the principal axis). The amplitude of the emitted gravitational waves at a distance r will be

$$h_0 \sim \frac{G}{c^4}\frac{If_0^2}{r}\varepsilon. \quad (9)$$

Substituting the typical values $m = 1.4M_\odot$, $I \sim 10^{45}$ g cm^2, $f_0 = 1$ GHz and the optimistic estimate of the asymmetry $\varepsilon = 10^{-5}$, we obtain $h_0 \sim 10^{-25}$ for a source at the Galactic center. A simple direct estimate shows that coherent accumulation of such a signal over three months (10^7 s) will enable detection against the background noise of $\sim 10^{-22}$ Hz$^{-1/2}$. This concept represents the basis of a program in which blind searches are carried out over the entire sky to keep the probability of success (i.e., encountering a pulsar with sufficiently strong gravitational-wave emission) at a maximum level [39]. One characteristic of the corresponding data processing is the need to demodulate the output signal from the receiver before it is accumulated. The reason is that gravitational-wave radiation from a single pulsar observed on the Earth is actually a quasi-monochromatic process modulated at the frequency $f(t)$, determined by the relative velocity between the source and receiver, as well as by the deceleration of the pulsar by itself. Moreover, there is an amplitude modulation $a(t)$, due to the motion of the antenna beam. Therefore, the signal at the receiver output takes the form

$$h(t) \sim Aa(t)\cos(2\pi f_0 t + \phi(t)) \quad (10)$$
$$\sim A\cos(2\pi \int f_{GW}(\tau)d\tau) = A\cos(\Phi(t,\lambda)),$$

where the effective variable frequency f_{GW} depends on the set of parameters $\bar{\lambda}$, which describe the Doppler shift ($\bar{v}$), direction toward the source ($\bar{n}$), deceleration spin coefficients (ν_k), etc. [41]; i.e.,

$$f_{GW} = f_0(1 + \frac{\bar{v}}{c}\bar{n})(1 + \sum_k \nu_k(t + \frac{\bar{x}}{c}\bar{n})^k). \quad (11)$$

Such modulation redistributes the emission power over all sidelobe combination frequencies, and the coherent signal accumulation becomes inefficient or even impossible. The demodulation can be carried out numerically if we conduct a time reduction of the output data, i.e., recalculate them using a new, so-called canonical, time scale:

$$t_s = \frac{\Phi(t,\lambda)}{2\pi f_0}. \quad (12)$$

Then the reduced output signal will again be monochromatic but will be a function of the new time t_s. This type of operation is known in radio astronomy as data stretching. Of course, the above canonical time will depend on all parameters of the signal [see (11) and (12)]. The quality of the demodulation (degree of monochromaticity of the reduced signal) on the time

scale $t_s(\bar{\lambda})$ depends on the mismatch between the parameters $\Delta\lambda$ and the values λ_i used to recalculate (stretch) the time, as well as the true parameters of the source. Via a fast Fourier transform with respect to t_s, the stretched data can be transformed into the spectral density of the stretched signal:

$$\tilde{O}(f,\bar{\lambda}) = \frac{1}{\sqrt{T_s}}\int_0^{T_s} O(t_s)\exp(i2\pi f t_s)dt_s. \quad (13)$$

Next, a usual identification procedure is applied to this spectral power to determine if the detection threshold was exceeded. A suitable duration of the observation interval T_s (calibrated to t_s) is determined by the degree to which monochromaticity is restored in the course of the numerical demodulation. A quantitative measure can be described by a special variable (the mismatch parameter) m, similar to the scheme for searching for chirp signals. If $\tilde{h}(f,\lambda)$ represents the Fourier transform of the output signal on the scale t_s, then the variable

$$m(\lambda,\Delta\lambda) = 1 - \frac{|\tilde{h}(f,\lambda+\Delta\lambda)|^2}{|\tilde{h}(f_0,\lambda)|^2} \quad (14)$$

defines the relative decrease in the signal power due to the procedure of stretching the data on a time scale with shifted (not true) parameters and digitizing them at a false frequency.

In the same way as in the case of chirp signals, an optimization must be performed between the basic characteristics of the problem—the duration of the observation interval (accumulation time) T_s, minimum mismatch parameter m, and required computational power—such that the reliability of the detection and the sensitivity (signal amplitude) remain at acceptable levels. This can be achieved by introducing a metric and grid in the parameter space; details and results can be found, for example, in [41, 42]. The computational volume depends strongly on the key external characteristics: the frequency region specified *a priori* $f_{\min} < f_0 < f_{\max}$, and the minimum deceleration period $\tau_{\min} = 1/\nu_{\max}$.

This program can be separated into two parts: (1) searches for young rapid pulsars with $f_{\max} =$ 1 Hz and $\tau_{\min} = 40$ s (born in supernova explosions), and (2) searches for old slow pulsars with $f_{\max} =$ 200 Hz and $\tau_{\min} = 10^3$ s. We present the numerical results from [41] for illustration. Searches for old slow pulsars using LIGO-I covering the entire sky will require ~ 1 Tflops of computational power for an observation time of 18 days; however the allowed observation time for young rapid pulsars will be only 0.8 days. On the other hand, a directed search for pulsars with known angular positions should make it possible to increase the observation time to 200 days. It is clear from these examples that such a program also requires a hierarchical approach, similar to that considered above for seeking chirp signals. Then even computational facilities with moderate power will be sufficient to conduct step-by-step optimized searches. Unfortunately, we must bear in mind the fact that the above estimates are based on optimistic predictions and probably overestimate the gravitational asymmetry (non-axial mass distribution) in the source $\varepsilon = 10^{-5}$. Theoretical predictions correspond to a wide range of values for this parameter, 10^{-5}–10^{-9} [43, 44], making it difficult to be sure of success with such a program, even if a very large volume of observational data is processed.

Nevertheless, the first practical effort of this type was an attempt to search for gravitational-wave radiation from pulsars in the Galactic center using the NAUTILUS cryogenic detector and an observation time of 10^7 s. Due to the particular coordinate directivity of this search and its narrow frequency band (0.2 Hz, $f_0 \approx 900$ Hz), the demodulation could be carried out by computers with moderate powers (10–100 Mflops). The data processing was done recently by the INFN group (Rome, Frascati) [45], who believe that the required sensitivity of 10^{-24} was achieved. No signals were detected at the 0.95 confidence level.

6. THE STOCHASTIC RADIATION BACKGROUND

This program of gravitational-wave experiments can be separated into two parts. The first concerns the detection of background noise from the stellar population of the Galaxy. The second, more ambitious, part is associated with the detection of relict gravitational radiation, which is a consequence of the cosmological Big Bang. These two problems are very different from a heuristic point of view. Of course it would be of interest to obtain experimental confirmation of old predictions of the Galactic gravitational-wave spectrum, which should have a peak at two to four h produced by the coalescence of binaries, whose amplitude may be as large as $h \sim 10^{-19}$ Hz$^{1/2}$ [46]. However, the heuristic importance of the experimental detection of the relict gravitational-wave background is incomparably greater, since it carries information about a very early stage of the Universe's evolution. Unfortunately, it will be difficult to attack either of these problems using the available cryogenic antennas and first-generation interferometers.

Nevertheless, detection of the gravitational-wave noise background is included in the plans of each antenna group and interferometer team. The observational data obtained are processed using special algorithms to estimate the experimental upper limits to the relict gravitational-wave background. Such upper limits are usually expressed in the dimensionless

units $\Omega_{gw} = \rho_c^{-1}(d\rho_{gw}/d\log f)$; i.e., the density of gravitational-wave energy in a logarithmic frequency interval normalized to the critical cosmological density ρ_c. Another combination that is more widely used is $h_0\Omega_{gw}$ (where $h_0 = H_0/100$ km s^{-1} Mpc^{-1} is the normalized Hubble constant). On the other hand, to describe interaction with a receiver, it is more convenient to use the metric spectral density (or the gravitational-wave density) $S_h(f)$, which is related to Ω_{gw} by the simple formula (for more details, see [47, 48]):

$$\Omega_{gw}(f) = \frac{4\pi^2}{3H_0^2} f^3 S_h(f). \qquad (15)$$

Theoretical predictions of the values of Ω_{gw} or $S_h(f)$ can be derived from the theory of evolution of the Universe, based on the Big Bang model, taking into account gravitational radiation. Such analyses usually assume the validity of general relativity and relativistic quantum-field theory. (This is precisely the area where gravitational-wave experiments require quantum calculations, whereas the previously-mentioned research programs were based on classical estimates.) Roughly speaking, the mechanism for the generation of the gravitational-wave background is the same as that responsible for the cosmic microwave background; however, the gravitational-wave generation begins at an earlier stage and involves a parametric amplification of zero-mode quantum oscillations of the gravitational radiation in the strongly varying gravitational field of the Universe at this early stage in its evolution; for more details, see papers by Grishchuk [49–51], and also [47, 48]. The calculations presented in these papers suggest that the expected gravitational-wave relict background in the frequency range 50–150 Hz should be

$$h_{gw} \sim 10^{-8}\sqrt{S_h(f)\Delta f} \sim 10^{-24}, \qquad (16)$$

where we have used the frequency band $\Delta f = 3 \times 10^{-8}$ Hz (which corresponds to accumulation of data for one year).

In general, detection of the gravitational-wave relict background represents a substantially more difficult task than detecting the cosmic microwave background. In particular, the input of a gravitational-wave antenna cannot be shielded to measure the level of its own intrinsic noise. In addition, it is not possible to change (modulate) a signal by changing the orientation of the antenna beam. Generally speaking, the well-known problem of detecting noise against a background of other noise can be solved more-or-less efficiently only if their distributions differ. Unfortunately, in the case under consideration, the relict gravitational-wave background is assumed to be Gaussian, like the receiver noise. The only remedy in such a situation is to measure the cross-correlation function of two (or more) identical receivers located quite close to each other in space ([52]).

Having an additive mixture of a stochastic signal and the individual intrinsic noise in each detector and measuring the cross-correlation in the observation interval τ, $K = \langle S_1 S_2\rangle_\tau$ (where $\langle ...\rangle$ denotes time averaging), we can get a signal-to-noise ratio that increases as $\sqrt{\tau}$; i.e., SNR $\sim (S_h/N)\sqrt{\Delta f \tau}$, where N is the spectral density of the receiver noise and Δf is the width of receiving band. This is a consequence of the fact that the background signals are the same but the intrinsic noises for the pair of detectors are independent. Formally, the sensitivity of ultracryogenic antennas and first-generation interferometers $h \sim 10^{-21}$ is quite sufficient to reach a limit 10^{-24} for an integration time of $\tau = 1$ year. Unfortunately, there are no two identical gravitational-wave receivers located near each other. For receivers with arbitrary angular orientations separated in space, the correlation of the signals S_i due to the stochastic background decreases by the mismatch factor $\Theta(x, f, \phi) \ll 1$, which depends on the distance between the receivers x, the frequency f, and the relative angle ϕ. The corresponding reduction functions have been calculated for all known pairs of interferometers [47] and bar antennas [53]. For example, $\Theta \sim 0.2$ for the EX–NA pair and $\Theta \sim 0.1$ for the AU–NA pair at a frequency of ~ 920 Hz. Consequently, it is difficult for the available network of cryogenic antennas and the first-generation interferometers to detect a gravitational-wave background at a level of $h_{\min} = 10^{-24}$.

In connection with establishing experimental upper limits, theoretical estimates of the minimum detected values of the background parameter $h_0\Omega_{gw}$ were done for all possible combinations of available receivers. These proved to be $\sim 5 \times 10^{-6}$ for interferometers [47] and $\sim 10^{-4}$ for bar antennas [53]; the corresponding values of $S_h(f)$ can be calculated using (16). We emphasize that the factor f^3 in (16) motivates observations at lower frequencies: a much better estimate of Ω_{gw} can be obtained for the same sensitivity to $[S_h(f)]_{\min}$. From this point of view, the LISA project—a space-based gravitational-wave interferometer with operational frequency range below 10^{-3} Hz—seems to be very promising [54]. On the other hand, we can hardly hope at this time that two such systems will simultaneously be deployed in space to search for the relict gravitational-wave background using their mutual correlation.

Apart from predicting the gravitational-wave background in the framework of standard cosmological models, there are many other predictions based on alternative theories, such as inflation, string cosmology, phase transitions in the early Universe, etc. The corresponding estimates sometimes yield a stronger

background amplitude, and important constraints on these models can be obtained from observations using the currently available network of gravitational-wave receivers. A more complete discussion of this topic and additional references can be found in [47, 48].

7. SEARCHING FOR ASTRO–GRAVITATIONAL CORRELATIONS

A new joint approach to analyzing data from gravitational-wave experiments has been discussed in recent years. The basic idea is to search for weak perturbations in the background noise of a gravitational detector that are correlated with some astrophysical event (such as a neutrino or gamma-ray burst) simultaneously detected by another apparatus [55–58]. The main argument in favor of such an approach is that the last stages of stellar evolution (supernova explosions, coalescence of binaries, gravitational collapse, etc.), which are usually considered as sources of gravitational-wave bursts, should often also be accompanied by neutrino and/or gamma-ray emission. Essentially, this means that detected neutrino and gamma-ray bursts represent times when the probability of detecting gravitational perturbations is increased. The clear advantages of this type of joint approach are a considerable decrease in the observation time (and, accordingly, the size of the data array to be processed) and the potential of accumulating weak signals. Unfortunately, there are relatively few published models (scenarios) describing objects that simultaneously generate gravitational, neutrino, and gamma-ray emission. Some examples can be found in [59–62], which are concerned with multistage scenarios for gravitational collapse accompanied by the formation of neutron stars, their fragmentation, the subsequent coalescence of the superdense remnants, etc. In such models, packets of neutrino pulses separated by time intervals of several seconds to several days can be generated, which are accompanied by bursts of gravitational waves and can carry away as much as several percent of the rest mass of their progenitors. A multistage scenario is also characteristic of the collapse of a supermassive star with large initial angular momentum [59]. In this type of scenario, the radial compression of matter can be interrupted by its partial reflection, fragmentation, coalescence and ejection of the fragments, etc. In principle, gravitational, electromagnetic, and neutrino bursts can be generated at each of these stages, although it remains to develop the corresponding models in detail.

Another problem to be solved is the development of an optimal data-processing system for searches for astro–gravitational correlations. A simple comparison of records obtained by different detectors is inefficient for identification of coincidences, since the time delays between different types of bursts are unknown and (more importantly) the sensitivities of gravitational-wave and neutrino detectors are insufficient. It seems likely that this provides at least part of the reason why searches for correlations between neutrino and gamma-ray data [63] and gamma-ray and gravitational-wave data [64] have been unsuccessful thus far. The first attempt to perform an optimal solution of the sort described above was undertaken by the RTM collaboration, which announced a neutrino–gravitational-wave correlation for supernova 1987A found using two gravitational-wave bar detectors operating at room temperature in Rome and Maryland, together with a neutrino scintillator under Mont Blanc [65]. The following Z variable was used as a sufficient statistic in their treatment of the joint data:

$$Z = (1/n)\sum_{k=1}^{n}(1/2)(R^2(t_k-\tau)/\sigma^2). \qquad (17)$$

This variable represents the sum of the squares of the envelope of the antenna output $R(t)/\sigma$ (proportional to the energy variations in the gravitational-wave detector) taken at the times of astrophysical events—i.e., at times t_k at which the neutrino anomaly was recorded—with some small shift τ. This sum is accumulated over the observation interval, which includes n events. After normalizing to the total number of events $(1/n)$, the meaning of this variable is evident: this is a selective sample average of the variations in receiver energy at the times corresponding to the astrophysical events.

It was shown in [66] that formal use of the maximum likelihood method in this case leads to a corrected [compared to (18)] sufficient statistic; namely, to the absolute-maximum variable Z_m in terms of variations in the shift τ:

$$Z_{\max} = \max_\tau Z(\tau), \tau \in [\tau_{\min}, \tau_{\max}]. \qquad (18)$$

The value τ_{opt} that corresponds to the maximum of $Z(\tau)$ can be taken as an estimate of the true time shift between the astrophysical event and the gravitational-wave signal. It is evident that both Z_m and τ_{opt} depend substantially on the range of variations in the shift τ, which therefore becomes a key parameter of the problem. There are no restrictions on the size of the shift interval $(\tau_{\min};\tau_{\max})$ in this statistical method. This interval should be chosen on the basis of *a priori* information, astrophysical scenarios, or some additional physical arguments. As was shown in [66], taking into account such constraints, the available experimental data obtained by the RTM collaboration are insufficient to definitively confirm the neutrino–gravitational-wave correlation from supernova 1987A.

The formulation of an optimal algorithm for the case of gamma-ray bursts turns out to be more difficult, due to the non-trivial time structure of such bursts, their probable cosmological origin, etc. Some possible approaches are described, for example, in [67, 68]. The algorithm based on (18) and (19) cannot be used directly here, since the concept of a time mark is not applicable in the case of gamma-ray events, due to the considerable variety in the shapes of detected gamma-ray bursts. Let us use the definition introduced in [69], where the effective duration of the burst is specified by the fraction of emitted energy, starting from the most intense bin in the pulse (a bin is the number of photons with a specified energy during the counting interval). As a result, the pulse can be represented by the time structure $G_i(t)$ exceeding an energy threshold G_0, in accordance with a chosen energy fraction (50%, 80%, etc). Then, the following phenomenological procedure, generalizing (18), can be used to construct a sufficient statistic Z for the case of gamma-ray bursts having several peaks.

Let $\tau_{i,k}$ be the time of a local maximum k in gamma-ray burst i whose amplitude exceeds the threshold, $G_{i,k} > G_0$. Then we have a set of random times, any of which can, in principle, be taken as the arrival time of the gamma-ray burst: $\tau_i \to (\tau_{i,1}, \tau_{i,2}, \tau_{i,3}, ...)$, where $k = 1, 2, 3, ..., m_i$ is the total number of local maxima of the function $G_i(t)$. We now introduce $W_i(\tau_j)$, which is the probability density for the arrival times; i.e., the probability that the time τ_j should be taken as the effective arrival time for burst i. In the adopted model for gamma-ray bursts, it is reasonable to represent $W_i(\tau_j)$ using a discrete series of coefficients $p_{i,k}$, which are proportional to the relative amplitudes of the maxima:

$$W_i(\tau_k) = \sum_{k=1}^{m_i} p_{ik}\delta(\tau_i - \tau_{ik}), \qquad (19)$$

where $p_{ik} = (G_{ik}/\sum_k^{m_i} G_{ik}) < 1$. As a result, the statistic of the average selective variation in the energy of the gravitational-wave detector E will be given by the following formula generalizing (18):

$$Z = (1/n)\sum_{i=1}^{n}\sum_{k=1}^{m_i} p_{ik}E(\tau_{ik} - \tau). \qquad (20)$$

Next, we can make a transformation to the variable $Z_{\max}$ in exactly the same way as in the case of neutrino events. We emphasize that introducing a universal shift τ is reasonable only for relatively nearby events with $z < 1$. In models where the sources are at cosmological distances, we must introduce differential shifts proportional to the factor $(1 + z)^{-1}$, as in [67].

8. CONCLUSION

Analysis of the current state of the gravitational-wave experiments shows that there is not much hope to obtain successful detections using receivers with sensitivities of about $h_{\min} = 10^{-21}$ in a 10^2–10^3 Hz frequency band or $h_{\min} = 10^{-22}$ in a narrow 10^{-5} Hz band. Such detections will be possible only for favorable events: those that are very close and, therefore, very rare.

It is important to emphasize that the strategy of item-by-item examination of templates, which is equivalent to multichannel reception of the signals and is characteristic of the programs discussed above, will shift the detection threshold (against the Gaussian background) in accordance with the law $h_{th} \sim 1.96h_{\min}\sqrt{\ln(N)}$ (the statistical loss due to the absence of *a priori* information), where N is the total number of templates (or channels) used. For example, when $N \approx 10^5$–10^6, the corresponding threshold will be shifted to $h \sim 10^{-20}$, which is clearly very far from the stated program goals. Further improvement of the sensitivity (if possible in principle) will require much time and the solution of several technical and methodological problems in the physics of measurements [18–20].

In this situation, the idea of searching for astro-gravitational correlations via the joint adaptive recording of signals incorporating the acquisition and use of additional information in parallel channels seems to be very promising, since it enables us to continue well-planned work on already-available receivers. From a theoretical point of view, this idea stimulates further research in two directions: (i) the development of more detailed joint scenarios for sources of neutrino–gamma–gravitational fluxes, and (ii) the construction of reliable robust data-processing procedures, which must be as free as possible of subjective elements in estimations of the statistical errors.

ACKNOWLEDGEMENTS

I am grateful to A.V. Gusev and K.A. Postnov for fruitful discussions, as well as to A.Yu. Kochetkova for technical assistance. This work was supported by the Russian Foundation for Basic Research (project no. 00-02-17884) and the Special State Science and Technology Program "High-Energy Physics."

REFERENCES

1. A. Einstein, *Sitzungsberichte* (Berlin, 1916), p. 688; *Sitzungsberichte* (Berlin, 1918), p. 154.
2. J. H. Taylor, Rev. Mod. Phys. **66**, 711 (1994).
3. J. Weber, Phys. Rev. Lett. **22**, 1320 (1969); **24**, 276 (1970).

4. V. B. Braginskiĭ, Ya. B. Zel'dovich, and V. N. Rudenko, Pis'ma Zh. Éksp. Teor. Fiz. **10**, 256 (1969) [JETP Lett. **10**, 163 (1969)].
5. V. M. Lipunov, S. N. Nazin, I. E. Panchenko, *et al.*, Astron. Astrophys. **298**, 677 (1995).
6. I. Bichak and V. N. Rudenko, *Gravitational Waves in General Relativity and the Problem of Detecting Them* [in Russian] (Mosk. Gos. Univ., Moscow, 1987).
7. P. Astone, M. Bassan, P. Bonifazi, *et al.*, Phys. Rev. D **47**, 362 (1993).
8. E. Mauceli, M. P. Mc Hugh, B. Hamilton, *et al.*, Phys. Rev. D **54**, 1264 (1996).
9. D. Blair, E. N. Ivanov, M. E. Tobar, *et al.*, Phys. Rev. Lett. **74**, 1908 (1995).
10. P. Astone, M. Bassan, P. Bonifazi, *et al.*, Astropart. Phys. **7**, 231 (1997).
11. G. Prodi, L. Conti, R. Mezzena, *et al.*, in *Gravitational Wavese,* Ed. by E. Coccia *et al.* (World Scientific, Singapore, 1998), p. 158.
12. P. R. Saulson, *Fundamentals of Interferometric Gravitational Wave Detectors* (World Scientific, Singapore, 1994).
13. M. K. Fujimoto, in *Gravitational Wave Detection II,* Ed. by S. Kawamura and N. Mio (Univ. Ac. Press, Tokyo, 2000), p. 41
14. B. Willke, P. Aufmuth, R. Balasumbaramanian, *et al.*, in *Gravitational Wave Detection II,* Ed. by S. Kawamura and N. Mio (Univ. Ac. Press, Tokyo, 2000), p. 15.
15. C. Bradaschia, G. Del Fabbro, A. Di Virgilio, *et al.*, Nucl. Instrum. Methods Phys. Res. A **289**, 518 (1990).
16. A. Abramovici, W. E. Althouse, R. W. P. Drever, *et al.*, Science **256**, 325 (1992).
17. M. Ando, in *Gravitational Wave Detection II,* Ed. by S. Kawamura and N. Mio (Univ. Ac. Press, Tokyo, 2000), p. 101.
18. H. J. Kimble, Yu. Levin, A. B. Matsko, *et al.*, gr-qc/0008026 (2000).
19. V. B. Braginsky, Phys. Scr. **76**, 122 (1998).
20. V. B. Braginskiĭ, Usp. Fiz. Nauk **170**, 743 (2000).
21. J. Weber, Phys. Rev. **117**, 306 (1960).
22. E. Amati, P. Astone, M. Bassan, *et al.*, Astron. Astrophys. **216**, 325 (1989).
23. P. Astone, M. Bassan, P. Bonifazi, *et al.*, Astropart. Phys. **10**, 83 (1999).
24. P. Astone, M. Bassan, P. Bonifazi, *et al.*, Phys. Rev. D **59**, 122 001 (1999).
25. P. Astone, S. D'Antonio, and G. Pizzella, gr-qc/0001030 (2000); Phys. Rev. D **62**, 042001 (2000).
26. G. Frosatti, J. Low Temp. Phys. **101**, 81 (1995).
27. N. Arnaud, F. Cavalier, M. Davier, and P. Hello, Phys. Rev. D **59**, 082 002 (1999).
28. W. Andersen, P. Brady, J. Creighton, and E. Flanagan, gr-qc/0001044 (2000).
29. E. E. Flanagan and S. A. Huges, Phys. Rev. D **57** (8), 4535 (1998); **57** (8), 4566 (1998).
30. W. G. Andersen, P. R. Brady, J. D. E. Creghton, and E. E. Flanagan, gr-qc/0008066 (2000).
31. J. Creighton, Phys. Rev. D **60**, 021 101 (1999).
32. V. N. Rudenko and A. V. Gusev, Int. J. Mod. Phys. D **9**, 353 (2000).
33. E. S. Phinney, Astrophys. J. Lett. **380**, L17 (1991).
34. V. M. Lipunov, K. A. Postnov, and M. E. Prokhorov, Mon. Not. R. Astron. Soc. **288**, 245 (1997).
35. V. M. Lipunov, K. A. Postnov, and M. E. Prokhorov, New Astron. **2**, 43 (1997).
36. B. J. Owen, Phys. Rev. D **53**, 6749 (1996).
37. B. J. Owen and B. S. Sathyaprakash, Phys. Rev. D **60**, 022 002 (1999).
38. C. Cutler, T. A. Apostolatos, L. Bildsten, *et al.*, Phys. Rev. Lett. **70**, 2984 (1993).
39. B. F. Schutz and M. A. Papa, gr-qc/9905018 (1999).
40. V. M. Lipunov, *Astrophysics of Neutron Stars* (Springer-Verlag, Berlin, 1992).
41. P. R. Brady, T. Creighton, C. Cutler, and B. F. Schutz, Phys. Rev. D **57**, 2101 (1998).
42. P. R. Brady and T. Creighton, Phys. Rev. D **61**, 082 001 (2000).
43. S. Bonazzola and E. Gourgoulhon, Astron. Astrophys. **312**, 675 (1996).
44. K. S. Thorne, in *Three Hundred Years of Gravitation,* Ed. by S. W. Hawking and W. Israel (Cambridge Univ. Press, Cambridge, 1987), p. 330.
45. P. Astone, M. Bassan, P. Bonifazi, *et al.*, gr-qc/0011072 (2000).
46. V. N. Mironovskiĭ, Astron. Zh. **42** (5), 977 (1965) [Sov. Astron. **9**, 752 (1965)].
47. B. Allen, in *Proceedings of the Les Houches School on Astrophysical Sources of Gravitational Waves,* Ed. by J. A. Marck and J. P. Lasota (Cambridge Univ. Press, Cambridge, 1996); gr-qc/9604033 (1996).
48. M. Maggiore, Phys. Rep. **331**, 283 (2000).
49. L. P. Grishchuk, Zh. Éksp. Teor. Fiz. **67**, 825 (1974) [Sov. Phys. JETP **40**, 409 (1975)].
50. L. P. Grishchuk, gr-qc/0002035 (2000).
51. L. P. Grishchuk, V. M. Lipunov, K. A. Postnov, *et al.*, Usp. Fiz. Nauk **171** (1), 3 (2001).
52. P. Michelson, Mon. Not. R. Astron. Soc. **227**, 933 (1987).
53. S. Vitale, M. Cerdonio, E. Coccia, *et al.*, Phys. Rev. D **55**, 1741 (1997).
54. J. Hough, in *Gravitational Wave Experiments,* Ed. by E. Coccia, G. Pizzella, and F. Ronga (World Scientific, Singapore, 1995), p. 50.
55. C. Bemporad, in *Gravitational Wave Experiments,* Ed. by E. Coccia, G. Pizzella, and F. Ronga (World Scientific, Singapore, 1995), p. 18.
56. P. Michelson, in *Gravitational Wave Experiments,* Ed. by E. Coccia, G. Pizzella, and F. Ronga (World Scientific, Singapore, 1995), p. 37.
57. A. V. Gusev, V. K. Milyukov, V. N. Rudenko, *et al.*, in *Gravitational Wave Experiments,* Ed. by E. Coccia, G. Pizzella, and F. Ronga (World Scientific, Singapore, 1995), p. 512.
58. G. Modestino and G. Pizzella, Nota Interna LNF 97/038 IR.1997.

59. K. S. Thorne, in *Particles and Nuclear Astrophysics and Cosmology in the Next Millenium* (World Scientific, Singapore, 1995), p. 160.
60. M. V. Sazhin, S. D. Ustyugov, and V. M. Chechetkin, Pis'ma Zh. Éksp. Teor. Fiz. **64** (12), 25 (1996) [JETP Lett. **64**, 871 (1996)].
61. V. S. Imshennik, Pis'ma Astron. Zh. **18**, 489 (1992) [Sov. Astron. Lett. **18**, 194 (1992)].
62. A. F. Zakharov, Astron. Zh. **73**, 605 (1996) [Astron. Rep. **40**, 552 (1996)].
63. M. Aglietta, A. Castellina, W. Fulgione, *et al.*, in *Proceedings of the 24th International Cosmic Ray Conference, Rome, 1995,* Vol. 2, p. 73.
64. P. Astone, A. Barbiellini, M. Bassan, *et al.*, Astron. Astrophys. **352**, 612 (1999).
65. M. Aglietta, G. Badino, G. Bologna, *et al.*, Nuovo Cimento C **12**, 75 (1989).
66. V. N. Rudenko, A. V. Gusev, V. K. Kravchuk, and M. P. Vinogradov, Zh. Éksp. Teor. Fiz. **118**, 979 (2000) [JETP **91**, 845 (2000)].
67. M. T. Murphy, J. K. Webb, and I. S. Heng, gr-qc/9911071 (1999).
68. J. C. Finn, S. D. Mohanty, and J. D. Romano, gr-qc/9903101 (1999).
69. I. G. Mitrofanov, D. S. Anfimov, and M. L. Litvak, *et al.*, Astrophys. J. **522**, 1069 (1999).

Translated by Yu. Dumin

Astronomy Reports, Vol. 45, No. 12, 2001, pp. 995–1001. Translated from Astronomicheskiĭ Zhurnal, Vol. 78, No. 12, 2001, pp. 1127–1134.

The Construction of Self-Consistent Models for Outflowing Stellar Envelopes

G. S. Bisnovatyi-Kogan and A. V. Dorodnitsyn

Space Research Institute, ul. Profsoyuznaya 84/32, Moscow, Russia

Received March 3, 2001

Abstract—The article presents self-consistent computations of the spherically symmetric envelope of a massive ($M = 20M_\odot$) star whose envelope is flowing outward under the action of continuum radiation pressure. A system of equations describing the outflow for arbitrary optical depth, degree of ionization, and opacity κ are obtained. A numerical solution is obtained for the case of constant κ and degree of ionization via approaching integrations from the singularities and smooth joining in the intermediate region. Asymptotic solutions are found in the vicinity of the sonic point and the singularity at infinity.

1. INTRODUCTION

Mass loss due to outflow is one factor introducing uncertainty into our understanding of the evolution of massive stars. There is the need for a theory that would make it possible to take into account mass loss in the process of evolutionary computations in a self-consistent way. It is currently clear that the role of outflow is extremely important for stellar evolution, but quantitative conclusions about mass-loss rates remain uncertain.

The evolution of stars with masses $M \geq 15M_\odot$ is accompanied by mass loss at rates reaching 10^{-4}–$10^{-6}M_\odot$/yr. This strongly influences the evolution of such stars in the supergiant stage.

The origin of the outflow is most likely the action of radiation pressure. The mechanisms responsible for the acceleration of matter by radiation flux are appreciably different for different types of massive stars.

Blue supergiants located near the main sequence lose mass via outflows that form in envelope regions having low optical depths. The transfer of momentum from radiation to matter occurs as a result of strong line absorption. The acceleration is strengthened by the velocity gradient in the medium (the Sobolev effect). This mechanism leads to the formation of very fast (~ 2000 km/s) winds from O stars. Wind acceleration by line radiation pressure probably also plays an important role in Wolf-Rayet (WR) stars, although, in this case, there can also be appreciable acceleration of matter at high optical depths by the continuum radiation flux [1].

The theory of outflows from early-type stars has been developed by Castor *et al.* [2] and is in good agreement with observational data. However, this theory only describes outflows in blue supergiants, and the expected mass-loss rates in later stages of evolution may be much higher.

In contrast to the situation with blue supergiants, outflows from evolved massive stars are formed by radiation pressure at high optical depths. At the onset of core helium burning, when the envelope expands and its temperature drops, hydrogen begins to recombine, leading to a sharp decrease in the opacity [3, 4].

As a result, the luminosity exceeds the local critical luminosity in an appreciable layer, and the envelope ceases to be static: an outflow begins. In this mechanism, matter is primarily accelerated in regions of high optical depth. The resulting intense outflow could lead to the complete ejection of the star's hydrogen envelope and, consequently, to the formation of a single helium Wolf-Rayet-type star. In [3], a search for extended gaseous envelopes around WR stars with masses on the order of the mass of the helium star itself was conducted as a test of this idea. Observations of a ring-like nebula around a single WR helium star are described in [5]. More detail about numerous observational and theoretical aspects of Wolf-Rayet winds can be found in [6]. The winds from WR stars are appreciably faster than those formed by continuum radiation pressure. The interaction of the fast WR wind with the slower wind of the precursor star can lead to the formation of the ring nebulae observed around WR stars [6].

Determining the mass-loss rates of evolved massive stars is accompanied by considerable difficulties from an observational point of view. This is associated with the fact that the intense mass loss from the star leads to large uncertainties in its position in the Hertzsprung–Russell diagram. The effective

1063-7729/01/4512-0995$21.00

temperature and luminosity of a star with an extended outflowing envelope depend on the physical characteristics of the envelope and can be determined only via self-consistent computations of the evolution of stars taking into account mass loss.

The star can occupy any position between the infrared and yellow regions of the HR diagram. In spite of the large number of papers published on this subject, self-consistent theories have essentially remained little developed. The first attempts to compute outflow under the action of continuum radiation pressure were made in [3, 7]. The equation of state was taken to be that for an equilibrium mixture of radiation and matter, which was a consequence of their neglect of regions with optical depths $\tau < 1$. As a result, the resulting mass-loss rates were overestimated.

Further studies in this direction were carried out by Zytkow [8, 9]. In spite of the considerable progress achieved in these papers, the crude treatment of optically thin layers led to appreciable uncertainties. For evolved supergiants with extended rarefied envelopes, it is important to correctly take into account layers with low optical depths. A detailed analysis of the consequences of neglecting optically thin regions in an outflowing atmosphere, together with a discussion of the appropriate outer boundary conditions, are given by Bisnovatyi-Kogan and Dorodnitsyn [10]. This paper lays out an approximate system of radiative hydrodynamics equations, which yield a correct description for the limiting cases of high and low optical depth in a gray-atmosphere approximation, as well as reasonable interpretations for intermediate cases. The approximate solution for an outflowing envelope obtained in [10] was not completely self-consistent, since the relation between the flow of energy associated with the outflowing matter and the flow of radiative energy was externally specified.

In the current paper, we construct a fully self-consistent model of the type proposed in [10]. We analyze in detail the asymptotic solution for large distances and join this solution to a global solution obtained numerically. In addition, we derive equations in the framework of this model taking into account the variable opacity and degree of ionization.

2. EQUATIONS OF RADIATIVE HYDRODYNAMICS VALID FOR ARBITRARY OPTICAL DEPTH IN THE SPHERICALLY SYMMETRICAL CASE

In layers of the star where the optical depth is high ($\tau \gg 1$), the matter can be described as an equilibrium mixture of an ideal gas and radiation:

$$p(\rho, T) = \frac{aT^4}{3} + \rho\mathcal{R}T, \qquad (1)$$

where P is the pressure, ρ the density, T the temperature, a the constant energy density of the radiation, and $\mathcal{R}$ the gas constant (which is a function of the variable chemical composition). In this case, radiative transport in outflowing matter with high optical depth can be described in a diffusion approximation.

In the case of low optical depth, we can no longer consider the matter to be in equilibrium with the radiation. Here, we see a bimodality in the interaction of the radiation and the outflowing matter in a spherically symmetrical envelope. The physical origin of this bimodality is that, at low τ, the radiation field at a given point is appreciably non-local: it is made up in large part by photons arriving from various other locations in a large volume. At the same time, some fraction of the radiation is in local thermodynamic equilibrium (LTE) with the matter.

LTE, which is characterized by a Boltzmann distribution for excited levels and equilibrium ionization, can also break down at low densities, when interactions with non-equilibrium photons become comparable to non-equilibrium processes. Note, however, that an LTE approximation is often adopted even if there is some disruption of LTE, which usually correctly yields the mean characteristics of the solution.

Two approaches are possible if we wish to describe the behavior of the outflowing matter and the radiation that is in partial equilibrium with this matter. We can consider the entire complex physics of the radiative transport against the background of the outflowing matter. This requires the solution of an extremely cumbersome problem in radiative transport jointly with appropriate gas-dynamical equations. However, instead of computing the intensity of the radiation field, we can use the first two (angular) moments of the transport equation (an Eddington approximation). In this case, we derive a variable Eddington factor, which relates the pressure and the radiative energy density and, thereby, closes the system of equations for the moments of the transport equation. There are various methods for angular averaging of the intensity; i.e., there is some freedom in our choice of the relation for the Eddington factor. In the general case, the variable Eddington factor enables a continuous description of both regions with $\tau \gg 1$ and those where $\tau < 1$.

When $\tau < 1$, in accordance with our approximate treatment [10], the isotropic component of the pressure can be decomposed into two components. The first is the gas pressure, and the second the pressure of that part of the radiation that is in equilibrium with the matter:

$$P^{\rm isotr}_{\tau\to 0} = \frac{aT^4}{3}\tau + \rho\mathcal{R}T. \qquad (2)$$

At infinity, $\tau \to 0$, and the contribution of the isotropic component to the total radiation pressure tends to zero.

An equation of motion describing a spherically symmetrical stationary outflow under the action of radiation pressure can be written

$$u\frac{du}{dr} = -\frac{1}{\rho}\frac{dP_g}{dr} - \frac{GM(1-\tilde{L}_{th})}{r^2}, \qquad (3)$$

$$\tilde{L}_{th} = \frac{L_{th}(r)}{L_{ed}}, \quad L_{ed} = \frac{4\pi cGM}{\kappa}, \qquad (4)$$

where u is the outflow velocity, κ the variable opacity, L_{th} the radiation flux, P_g the gas pressure, M the mass contained inside the radius r, G the gravitational constant, and c the speed of light. Equation (3) is exact, and does not depend on our adopted approximate description of the behavior of matter and radiation for arbitrary τ. The energy integral can be written

$$L = 4\pi\rho u r^2\left(E + \frac{p}{\rho} - \frac{GM}{r} + \frac{u^2}{2}\right) + L_{th}(r). \qquad (5)$$

Here, L is the constant total energy flux, which is made up of the fluxes of radiative energy and of the energy of the outflowing matter.

The radiation flux L_{th} can be found from the transport equation written in moment form:

$$L_{th} = -\frac{4\pi r^2 c}{\kappa\rho}\left(\frac{dP_r}{dr} - \frac{E_r\rho - 3p_r}{r}\right), \qquad (6)$$

where P_r is the radiation pressure and E_r is the radiation energy density.

The continuity equation, expressions for the pressure and energy density, and the optical depth can be written in the form [10]:

$$\frac{\dot{M}}{4\pi} = \rho u r^2, \qquad (7)$$

$$p = p_r + p_g, \qquad (8)$$

$$E = E_r + E_g + \epsilon_i, \qquad (9)$$

$$p_r = \frac{aT^4}{3}\left(1 - e^{-\tau}\right) + \frac{L_{th}^{\infty}}{4\pi r^2 c}, \qquad (10)$$

$$E_r\rho = aT^4\left(1 - e^{-\tau}\right) + \frac{L_{th}^{\infty}}{4\pi r^2 c}, \qquad (11)$$

$$p_g = \rho\mathcal{R}T, \quad E_g = \frac{3}{2}\mathcal{R}T, \qquad (12)$$

$$\tau = \int_r^{\infty}\kappa\rho dr. \qquad (13)$$

The quantity ϵ_i in (9) is the specific ionization energy. These equations are valid for variable κ and $\mathcal{R}$; however, these quantities were assumed to be constant in [10]. Taking into account the relation $\mathcal{R} = k/\mu m_p$, (where k is the Boltzmann constant and μ is the mean molecular mass) and introducing the notation

$$\frac{\partial p_g}{\partial\rho} = \mathcal{R}T\gamma_\rho, \qquad \frac{\partial p_g}{\partial T} = \mathcal{R}\rho\gamma_T, \qquad (14)$$

where

$$\gamma_\rho = 1 - \left(\frac{\partial\ln\mu}{\partial\ln\rho}\right)_T, \quad \gamma_T = 1 - \left(\frac{\partial\ln\mu}{\partial\ln T}\right)_\rho, \qquad (15)$$

we can transform the equation of motion (3) into the form

$$\left(\mathcal{R}T\gamma_\rho - \frac{\dot{M}^2}{16\pi^2\rho^2 r^4}\right)\frac{1}{\rho}\frac{d\rho}{dr} = \left(\frac{\dot{M}}{4\pi}\right)^2\frac{2}{\rho^2 r^5} - \frac{GM}{r^2}(1-\tilde{L}_{th}) - \mathcal{R}\gamma_T\frac{dT}{dr}. \qquad (16)$$

Here, we have used relations (7), (12), and (14).

We now substitute (10)–(11) into (6). Using (13) when differentiating, we substitute the resulting expression for L_{th} into (5):

$$4\pi r^2 c\lambda(1-e^{-\tau})\frac{dT}{dr} = \dot{M}\left\{\frac{4aT^4}{3\rho}(1-e^{-\tau}) + \frac{5}{2}\mathcal{R}T + \frac{2L_{th}^{\infty}}{4\pi r^2 c\rho} - \frac{GM}{r} + \frac{u^2}{2} + \epsilon_i\right\} + 4\pi r^2 c\frac{e^{-\tau}acT^4}{3} - L. \qquad (17)$$

Here, λ denotes the coefficient of radiative heat conduction:

$$\lambda = \frac{4acT^3}{3\kappa\rho}. \qquad (18)$$

We have from (13)

$$\frac{d\tau}{dr} = -\kappa\rho. \qquad (19)$$

Together with (19), equations (16) and (17) form the desired system of differential equations.

After manipulation, (6) takes the form

$$L_{th} = -4\pi r^2\left(\lambda(1-e^{-\tau})\frac{dT}{dr} - \frac{1}{3}acT^4e^{-\tau}\right). \qquad (20)$$

If the anisotropic radiation-pressure force is much less than the equilibrium isotropic component of the radiation pressure, i.e.,

$$\frac{L_{th}}{4\pi r^2} \ll acT^4, \qquad (21)$$

then we obtain in the limiting case $\tau\to\infty$ the system of equations for equilibrium radiative gas dynamics analyzed in [11].

Equation (16) has a singularity where its left-hand side vanishes:

$$(\mathcal{R}T\gamma_\rho)_{cr} = \frac{\dot{M}^2}{16\pi^2\rho_{cr}^2 r_{cr}^4}, \qquad \dot{M} = 4\pi\rho_{cr}u_{cr}r_{cr}^2, \tag{22}$$

$$u_{cr}^2 = (\mathcal{R}T\gamma_\rho)_{cr} \equiv \left(\frac{\partial p}{\partial\rho}\right)_{T,cr} = u_{s,cr}, \tag{23}$$

where u_s is the isothermal sound speed. After substituting the expression for dT/dr into (16), we obtain an equation of motion that can be solved for the derivative. For a transonic wind, the derivative $d\rho/dr$ should remain finite, so that the right-hand side of this equation must simultaneously vanish. There exist solutions that are subsonic in the entire region—so-called breezes. For these solutions, the derivative is equal to zero when $r = r_{cr}$, and the wind is accelerated in the region $r < r_{cr}$ and decelerated in the region $r > r_{cr}$. However, the limiting velocities that are obtained for such solutions are too small to be in good agreement with the observations. Another branch of solutions corresponding to motion first with deceleration ($r < r_{cr}$) and then with acceleration ($r > r_{cr}$) do not satisfy the condition that the velocity vanish deep in the star. The system of equations (16), (17), and (19) have a saddle singularity where the velocity is equal to the isothermal sound speed u_s.

The desired solution of the system (16), (17), and (19) should pass through the critical point and satisfy the outer boundary conditions. The temperature and density should vanish at infinity. More precisely, the density should become very small. Thus, we have for the outer boundary conditions:

$$T = 0, \qquad \rho \sim \frac{1}{r^2} \to 0 \qquad u \to \text{const} = u_\infty. \tag{24}$$

In the limiting case $\kappa \to \infty$, $\lambda \to 0$, both singularities of the system degenerate into a single singular point where the velocity is equal to the adiabatic sound speed [11].

Here, we wish to elucidate the suitability of the proposed method for studies of outflows under the action of radiation pressure for arbitrary τ. Therefore, in our numerical computations we should simplify the task at hand as much as possible without losing important aspects of the problem. The physical picture will not be fundamentally changed if we assume $\kappa = \text{const}$ and also take the matter to be fully ionized.

3. NUMERICAL SOLUTION FOR $\kappa = \text{const}$ AND FULL IONIZATION ($\mu = \text{const}$)

Let us write the system (16), (17), and (19) in dimensionless form, making the following change of variables:

$$\tilde{T}(r) = \frac{T(r)}{T_{cr}}, \quad \tilde{\rho}(r) = \frac{\rho(r)}{\rho_{cr}}, \quad \tilde{L}_{th} = \frac{L_{th}}{L_{ed}}, \quad \tilde{x} = \frac{r_{cr}}{r}. \tag{25}$$

We obtain after manipulation (here and below, we omit tildas for simplicity of presentation):

$$\frac{d\rho}{dx} = \left(\frac{x^4}{\rho^3} - \frac{T}{\rho}\right)^{-1}\left\{\frac{dT}{dx}\left(1 + A_1(1-e^{-\tau})\frac{T^3}{\rho}\right) - A_3 + \frac{1}{4}\frac{A_1 e^{-\tau}}{A_5}\frac{T^4}{x^2} + 2\frac{x^3}{\rho^2}\right\}, \tag{26}$$

$$\frac{dT}{dx} = -\left(\frac{5}{2}T - A_3 x + \frac{1}{2}\frac{x^4}{\rho^2} + (1-e^{-\tau})A_1\frac{T^4}{\rho} + \frac{e^{-\tau}}{4A_2A_5}\frac{T^4}{x^2} + 2L_{th}^\infty A_3 A_5\frac{x^2}{\rho} - \frac{A_4}{A_2}\right)\frac{A_2\rho}{T^3(1-e^{-\tau})}, \tag{27}$$

$$\frac{d\tau}{dx} = \frac{\rho}{A_5 x^2}, \tag{28}$$

where

$$A_1 = \frac{4aT_{cr}^3}{3\rho_{cr}\mathcal{R}}, \quad A_2 = \frac{3\kappa}{4ac}\frac{\rho_{cr}\mathcal{R}}{r_{cr}T_{cr}^3}\frac{\dot{M}}{4\pi}, \tag{29}$$

$$A_3 = \frac{GM}{r_{cr}\mathcal{R}T_{cr}}, \quad A_4 = \frac{3\kappa L}{16ac\pi}\frac{\rho_{cr}}{r_{cr}T_{cr}^4}. \tag{30}$$

The physical meanings of the dimensionless parameters are as follows (see also [11]): $A_1/4$ is the ratio of the isotropic part of the radiation pressure to the gas pressure at the critical point, $(2A_3)^{1/2}$ is the ratio of the parabolic sound speed to the isothermal sound speed at the critical point, and A_1A_4/A_3 is the ratio of the total energy flux to the Eddington luminosity at the critical point.

The parameter

$$A_5 = \frac{1}{r_{cr}\kappa\rho_{cr}}, \tag{31}$$

is a quantity of the order of the inverse of the optical depth at the critical point.

Taking into account that the dimensionless L_{th}^∞ and τ_{cr} are also parameters of the problem, the number of dimensionless parameters (seven) exceeds the number of equations in the system (26)–(28) (three) by four. More detail about the question of the number of dimensionless parameters can be found in [10].

We obtain in the dimensionless variables for L_{th} from (6)

$$L_{th} = \frac{A_1}{A_3}\left(\frac{T^3}{\rho}(1-e^{-\tau})\frac{dT}{dx} + \frac{e^{-\tau}}{4A_5}\frac{T^4}{x^2}\right). \quad (32)$$

The solution of (26)–(28) must pass through the critical point. This condition makes it possible to decrease the number of dimensionless parameters by one. Equating the expression in braces in (26) to zero, we obtain the following relation between the parameters:

$$\begin{aligned} A_4 = \big(&4A_3A_5(1-e^{-\tau_{cr}}) + 8A_5(-1+e^{-\tau_{cr}}) \\ &+ 4A_1^2A_2A_5\big(1-2e^{-\tau_{cr}}+(e^{-\tau_{cr}})^2\big) \\ &+ A_2\big(12A_5 + A_3(-4A_5 + 8A_5^2L_{th}^{\infty}\big) \\ &+ A_1A_2\big(16A_5(1-e^{-\tau_{cr}}) \\ &+ A_3(4A_5(-1+e^{-\tau_{cr}}) + A_5^2(8L_{th}^{\infty} \\ &- 8e^{-\tau_{cr}}L_{th}^{\infty}))\big) + e^{-\tau_{cr}}\big)/4\big(A_5 + A_1A_5(1-e^{-\tau_{cr}})\big). \end{aligned} \quad (33)$$

Another dimensionless parameter, A_5, can be expressed explicitly as a combination of physical constants and other dimensionless parameters:

$$A_5 = \left(\frac{3}{4}\right)^{1/5} \frac{A_3^{1/5}\mathcal{R}^{4/5}}{A_1^{3/5}A_2^{4/5}\kappa^{1/5}a^{1/5}c^{4/5}(GM)^{1/5}}. \quad (34)$$

To obtain a numerical solution, we must integrate the system (26)–(28) from the sonic point outward, satisfying the outer boundary conditions, and inward, smoothly joining the solution with the static solution for the core. The desired solution for the outer region is obtained after integrating from the sonic point outward and from the singularity at infinity inward and smoothly joining the solutions in the intermediate region. Since we wish to obtain solutions for an outflowing envelope, we will seek only solutions for this outer region. The remaining two free parameters will be unambiguously determined after joining with the solution for the core.

The physical quantities are computed from the dimensionless parameters using the formulas

$$r = \left(\frac{4a\kappa}{3c}\right)^{2/5} \frac{(GM)^{7/5}}{\mathcal{R}^{8/5}} \frac{1}{(A_1^2A_2A_3)^{2/5}A_3x}, \quad (35)$$

$$\rho = \left(\frac{3\mathcal{R}}{4a}\right)^{1/5} \left(\frac{c\mathcal{R}^{1/2}}{\kappa GM}\right)^{6/5} (A_1^2A_2A_3)^{6/5}\frac{\tilde{\rho}}{A_1}. \quad (36)$$

$$T = \left(\frac{3c\mathcal{R}^{3/2}}{4a\kappa GM}\right)^{2/5} (A_1^2A_2A_3)^{2/5}\tilde{T}. \quad (37)$$

Near the critical point $x = 1$, the solution can be presented as a series in powers of $(1-x)$:

$$T = 1 + a(1-x), \quad (38)$$

$$\rho = 1 + b(1-x). \quad (39)$$

We can write the exponential in the form

$$e^{-\tau} \simeq e^{-\tau cr}\left(1 + \frac{y}{A_5}\right),$$

where $y = 1-x$. The coefficients a and b are found after substituting (38) and (39) into the original system and equating coefficients of corresponding powers of y:

$$b = \frac{4A_5\left(A_4 - A_2\left(3 - A_1(e^{-\tau_{cr}}-1) - A_3(1-2A_5L_{th}^{\infty})\right)\right) - e^{-\tau_{cr}}}{4A_5(e^{-\tau_{cr}}-1)}, \quad (40)$$

$$a = -\left(c_1 + (c_1^2 - 4c_2c_0)^{\frac{1}{2}}\right)/(2c_2). \quad (41)$$

An expression for c_i is presented in [10].

The solution at the singularity at infinity must also be written as a series expansion. The form of the series T is determined by the requirement that $L_{th} \to$ const as $x \to 0$:

$$T = a_{\infty}\sqrt{x}. \quad (42)$$

In the series ρ, we must take into account two terms of the expansion:

$$\rho = b_1x^2 + b_2x^{5/2}. \quad (43)$$

The expansion for the velocity at infinity has the form

$$u \simeq u_{\infty} - \frac{b_2}{b_1^2}\sqrt{x}, \quad u_{\infty} = \frac{1}{b1}. \quad (44)$$

Note that, in Fig. 4 of [10], the extrapolation of the solution for u/u_{cr} to the region of small x (at infinity) is inaccurate.

At the singularity $x = 0$, we can write the exponential in the form

$$e^{-\tau} \simeq 1 - \frac{\rho}{A_5x} + \frac{1}{2}\left(\frac{\rho}{A_5x}\right)^2. \quad (45)$$

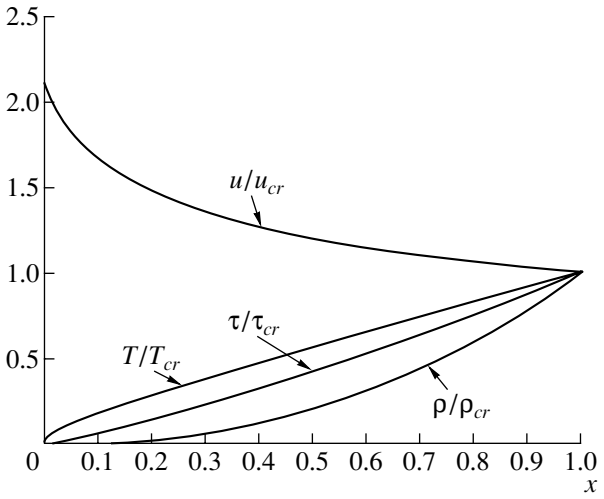

Distributions of the temperature T, density ρ, and velocity u in a self-consistent outflowing envelope. The solution of the system (26)–(28) was obtained by numerically integrating from the singularity at infinity ($x = 0$) inward and from the sonic point ($x = 1$) outward and then smoothly joining the solutions in the intermediate region. The exit from the singularities was achieved using the expansions (38), (39) and (42), (43). This solution is characterized by the dimensionless parameter values $A_1 = 4.73$, $A_2 = 2.82 \times 10^{-5}$ (chosen arbitrarily), $A_3 = 6.70$, $A_4 = 0.82$, $A_5 = 0.05$, $\tau_{cr} = 14.3$, $L_{th}^{\infty} = 0.570$, and $L = 0.579$ (obtained from the self-consistent solution). The joining point was specified for $r_{cr}/r = 0.5$.

The value of L_{th}^{∞} is unambiguously determined after substituting (42) and (45) into (32):

$$L_{th}^{\infty} = \frac{3}{4}\frac{a_{\infty}^4 A_1}{A_3 A_5}. \tag{46}$$

After substituting the asymptotic series (42) and (43) into the system (26)–(28) and using (46) and (33) also, we obtain the following system that can be used to determine a_{∞}, b_1, and b_2:

$$\begin{aligned}
0 = {} & 6A_2A_5^2 + 6A_1A_2A_5^2 + 18a_{\infty}^4A_1A_2A_5^2b_1 \\
& + 18a_{\infty}^4A_1^2A_2A_5^2b_1 + 9a_{\infty}^4A_5b_1^2 + 9a_{\infty}^4A_1A_5b_1^2 \\
& + 24A_5^2b_1^2 - 36A_2A_5^2b_1^2 - 48A_1A_2A_5^2b_1^2 \\
& - 18a_{\infty}^4A_1A_2A_5^2b_1^2 - 12A_1^2A_2A_5^2b_1^2 \\
& - 18a_{\infty}^4A_1^2A_2A_5^2b_1^2 - 12A_3A_5^2b_1^2 \\
& + 12A_2A_3A_5^2b_1^2 + 12A_1A_2A_3A_5^2b_1^2 \\
& - 6A_1A_2A_5^2e^{-\tau_{cr}} - 18a_{\infty}^4A_1^2A_2A_5^2b_1e^{-\tau_{cr}} \\
& - 3A_5b_1^2e^{-\tau_{cr}} - 9a_{\infty}^4A_1A_5b_1^2e^{-\tau_{cr}} \\
& - 24A_5^2b_1^2e^{-\tau_{cr}} + 48A_1A_2A_5^2b_1^2e^{-\tau_{cr}} \\
& + 24A_1^2A_2A_5^2b_1^2e^{-\tau_{cr}} + 18a_{\infty}^4A_1^2A_2A_5^2b_1^2e^{-\tau_{cr}} \\
& + 12A_3A_5^2b_1^2e^{-\tau_{cr}} - 12A_1A_2A_3A_5^2b_1^2e^{-\tau_{cr}} \\
& - 12A_1^2A_2A_5^2b_1^2(e^{-\tau_{cr}})^2,
\end{aligned} \tag{47}$$

$$\begin{aligned}
0 = {} & -18A_2A_5^2b_1^2 - 18A_1A_2A_5^2b_1^2 - 54a_{\infty}^4A_1A_2A_5^2b_1^3 \\
& - 54a_{\infty}^4A_1^2A_2A_5^2b_1^3 + 63a_{\infty}^4A_5b_1^4 + 63a_{\infty}^4A_1A_5b_1^4 \\
& - 72A_5^2b_1^4 + 108A_2A_5^2b_1^4 + 144A_1A_2A_5^2b_1^4 \\
& + 54a_{\infty}^4A_1A_2A_5^2b_1^4 + 36A_1^2A_2A_5^2b_1^4 \\
& + 54a_{\infty}^4A_1^2A_2A_5^2b_1^4 36A_3A_5^2b_1^4 - 36A_2A_3A_5^2b_1^4 \\
& - 36A_1A_2A_3A_5^2b_1^4 - 18a_{\infty}^3A_5b_1b_2 \\
& - 18a_{\infty}^3A_1A_5b_1b_2 + 18A_1A_2A_5^2b_1^2e^{-\tau_{cr}} \\
& + 54a_{\infty}^4A_1^2A_2A_5^2b_1^3e^{-\tau_{cr}} + 9A_5b_1^4e^{-\tau_{cr}} \\
& - 63a_{\infty}^4A_1A_5b_1^4e^{-\tau_{cr}} + 72A_5^2b_1^4e^{-\tau_{cr}} \\
& - 144A_1A_2A_5^2b_1^4e^{-\tau_{cr}} - 72A_1^2A_2A_5^2b_1^4e^{-\tau_{cr}} \\
& - 54a_{\infty}^4A_1^2A_2A_5^2b_1^4e^{-\tau_{cr}} - 36A_3A_5^2b_1^4e^{-\tau_{cr}} \\
& + 36A_1A_2A_3A_5^2b_1^4e^{-\tau_{cr}} + 18a_{\infty}^3A_1A_5b_1b_2e^{-\tau_{cr}} \\
& + 36A_1^2A2A_5^2b_1^4(e^{-\tau_{cr}})^2.
\end{aligned} \tag{48}$$

Equations (47) and (48) can be obtained to zeroth order in x from (26) and (27), respectively. Multiplying (47) by $3b_1^2$ and adding it to (48), we obtain

$$-18a_{\infty}^3A_5b_1(5a_{\infty}b_1^3 - b_2)(-1 + A_1(-1 + e^{-\tau_{cr}})) = 0, \tag{49}$$

whence

$$a_{\infty} = \frac{b_2}{5b_1^3}. \tag{50}$$

It follows from (42) that $a_{\infty} > 0$. The positivity of b_1 and b_2 follow from this condition, as well as from (50).

After substituting (50) into (47), we obtain an equation whose positive root is b_1:

$$\begin{aligned}
0 = {} & 1250A_2A_5b_1^{11} + 1250A_1A_2A_5b_1^{11} + 5000A_5b_1^{13} \\
& - 7500A_2A_5b_1^{13} - 10000A_1A_2A_5b_1^{13}
\end{aligned}$$

$$
\begin{aligned}
&- 2500A_1^2A_2A_5b_1^{13} - 500A_3A_5b_1^{13} \\
&+ 2500A_2A_3A_5b_1^{13} + 2500A_1A_2A_3A_5b_1^{13} \\
&+ 6A_1A_2A_5b_2^4 + 6A_1^2A_2A_5b_2^4 + 3b_1b_2^4 \\
&+ 3A_1b_1b_2^4 - 6A_1A_2A_5b_1b_2^4 - 6A_1^2A_2A_5b_1b_2^4 \\
&- 1250A_1A_2A_5b_1^{11}e^{-\tau_{cr}} - 625b_1^{13}e^{-\tau_{cr}} \\
&- 5000A_5b_1^{13}e^{-\tau_{cr}} + 10000A_1A_2A_5b_1^{13}e^{-\tau_{cr}} \\
&+ 5000A_1^2A_2A_5b_1^{1}3e^{-\tau_{cr}} + 2500A_3A_5b_1^{13}e^{-\tau_{cr}} \\
&- 2500A_1A_2A_3A_5b_1^{13}e^{-\tau_{cr}} - 6A_1^2A_2A_5b_2^4e^{-\tau_{cr}} \\
&- 3A_1b_1b_2^4e^{-\tau_{cr}} + 6A_1^2A_2A_5b_1b_2^4e^{-\tau_{cr}} \\
&- 2500A_1^2A_2A_5b_1^{13}(e^{-\tau_{cr}})^2. \qquad (51)
\end{aligned}
$$

To obtain b_1, we must numerically solve (51). In this way, after performing approaching integrations from the singularities and smoothly joining the curves in the intermediate region, we obtained a solution passing through the sonic point and satisfying the boundary conditions at infinity. The curves presented in the figure correspond to the following values of the dimensionless parameters: $A_1 = 4.73$, $A_2 = 2.82 \times 10^{-5}$, $A_3 = 6.70$, $A_4 = 0.82$, $A_5 = 0.05$, $\tau_{cr} = 14.3$, $L_{th}^{\infty} = 0.570$, $L = 0.519$, $b_1 = 0.46$, $b_2 = 0.24$, and $a_T = 0.49$. We took the mass of the star to be $M = 20M_{\odot}$. Using (35)–(37), we obtain for the physical quantities at the critical point $T_{cr} = 6.04 \times 10^2$K, $r_{cr} = 7.88 \times 10^{15}$ cm, $\rho_{cr} = 5.65 \times 10^{-15}$ g/cm^3, and $\tau_{ph} \simeq 2$. The flow velocity at the critical point is $v_{cr} \approx 2.75$ km/s. The corresponding mass-loss rate is $\dot{M} \approx 1.5 \times 10^{-2}$ M$_{\odot}$ /yr.

We should note that these values of the physical parameters resulted from the fact that the computations were carried out for a constant κ and constant degree of ionization. The resulting high mass-loss rate can qualitatively be explained by the fact that the sonic point lies at large r and $\dot{M} = 4\pi r_{cr}^2 \rho_{cr} u_{cr}$. If we allow for realistic values of κ, the singularity is located near the location of an opacity jump, i.e., at low R_{cr} and, accordingly, T_{cr}. Thus, with realistic values for κ, the mass-loss rate will be lower, the wind speed somewhat higher, and the outflowing envelope hotter. The position of the photosphere in the moving atmosphere differs from the static case and can be determined from the results of the numerical computations by the condition that $L_{th}(r) = 4\pi r^2 \sigma T^4$. See [10] for a detailed analysis of the problem of finding the location of the photosphere and a comparison with previous results.

4. CONCLUSION

We have used the method developed in [10] to obtain a system of equations describing a spherically symmetrical outflow under the action of continuum radiation pressure with variable opacity and degree of ionization. The method enables a description of the outflow for arbitrary τ. The outflow forms primarily in the region $\tau \gg 1$, smoothly making a transition to the region $\tau < 1$. In the resulting solution, $L_{th}^{\infty} = 0.570$ and $L = 0.579$; i.e., the convective flux of energy comprises a modest fraction (about 2%) of the total energy flux L. This is apparently associated with the fact that the total energy flux, which is equal to the thermal flux in the region $\tau \gg 1$, was only $0.58\,L$. We expect an increase in the fraction of convective energy flux as the total luminosity approaches the critical Eddington limit. In the limiting case of infinite optical depth, a fully ionized gas, and $\kappa = \text{const}$, the system of equations agrees with that obtained in [11].

In our numerical solution, we considered the special case of constant $\mathcal{R}$ and κ. We found a self-consistent solution for the outflowing envelope passing through the sonic point and satisfying the boundary conditions at infinity. This solution was obtained by performing approaching integrations from the singularities and smoothly joining the curves in the intermediate region. This enabled a self-consistent determination of all the parameters of the problem. Parameters remaining free can be determined after joining the solution for the outflowing envelope with that for the static core. Proceeding from the numerical solutions, we can determine the position of the photosphere in a stationary outflowing envelope. With the use of realistic $\kappa(\rho, T)$ and $\mathcal{R}(\rho, T)$, the resulting system of equations can be applied directly to computations of the stationary outflowing envelopes of massive stars.

REFERENCES

1. M. Kato and I. Iben, Astrophys. J. **394**, 305 (1992).
2. J. Castor, D. Abbot, and R. Klein, Astrophys. J. **195**, 157 (1975).
3. G. S. Bisnovatyi-Kogan and D. K. Nadyozhin, Astrophys. Space Sci. **15**, 353 (1972).
4. R. Stothers and C.-W. Chin, Astrophys. J. **233**, 267 (1979).
5. L. Smith, in *Proceedings of Symposium on Wolf-Rayet Stars, Boulder, 1968.*
6. T. A. Lozinskaya, *Supernovae and Stellar Wind in the Interstellar Medium* (Nauka, Moscow, 1986; American Inst. of Physics, New York, 1992).
7. G. S. Bisnovatyi-Kogan and D. K. Nadyozhin, Nauchn. Inf. Astron. Sovet Akad. Nauk SSSR **11**, 157 (1969).
8. A. Zytkow, Acta Astron. **22**, 103 (1972).
9. A. Zytkow, Acta Astron. **23**, 121 (1973).
10. G. S. Bisnovatyi-Kogan and A. V. Dorodnitsyn, Astron. Astrophys. **344**, 647 (1999).
11. G. S. Bisnovatyi-Kogan, Prikl. Mat. Mekh. **31**, 762 (1967).

Translated by D. Gabuzda